

Barium Ions for Quantum Computation

Matthew Dietrich

A dissertation submitted in partial fulfillment
of the requirements for the degree of

Doctor of Philosophy

University of Washington

2009

Program Authorized to Offer Degree: Department of Physics

University of Washington
Graduate School

This is to certify that I have examined this copy of a doctoral dissertation by

Matthew Dietrich

and have found that it is complete and satisfactory in all respects,
and that any and all revisions required by the final
examining committee have been made.

Chair of the Supervisory Committee:

Boris Blinov

Reading Committee:

Boris Blinov

Subhadeep Gupta

David Bacon

Date: _____

In presenting this dissertation in partial fulfillment of the requirements for the doctoral degree at the University of Washington, I agree that the Library shall make its copies freely available for inspection. I further agree that extensive copying of this dissertation is allowable only for scholarly purposes, consistent with "fair use" as prescribed in the U.S. Copyright Law. Requests for copying or reproduction of this dissertation may be referred to Proquest Information and Learning, 300 North Zeeb Road, Ann Arbor, MI 48106-1346, 1-800-521-0600, to whom the author has granted "the right to reproduce and sell (a) copies of the manuscript in microform and/or (b) printed copies of the manuscript made from microform."

Signature_____

Date_____

University of Washington

Abstract

Barium Ions for Quantum Computation

Matthew Dietrich

Chair of the Supervisory Committee:

Assistant Professor Boris Blinov

Department of Physics

Barium ion is investigated as a hyperfine qubit. $^{137}\text{Ba}^+$ is trapped in a linear Paul trap and laser cooled. Isotope selective photoionization is employed to improve trapping from an isotopically impure source. Optical pumping into the magnetically insensitive $^2\text{S}_{1/2}(\text{F}=2)$ $m_{\text{F}} = 0$ state is shown, and readout by electron shelving into the $^2\text{D}_{5/2}$ is demonstrated both directly and by adiabatic passage. Rabi flops between the $^2\text{S}_{1/2}$ $\text{F}=1$ and $\text{F}=2$ states is accomplished by exposure to 8.037 GHz microwave radiation.

Several methods of locking the cooling lasers have been attempted and are discussed. Stabilization of the infrared laser used to drive the $\text{D}_{5/2} \leftarrow \text{S}_{1/2}$ transition is of particular interest, and several novel technologies are tested in this purpose.

TABLE OF CONTENTS

	Page
List of Figures	iii
List of Tables	v
Part I: Theoretical Preliminaries	1
Chapter 1: Quantum Computing	2
1.1 Bloch Spheres and Phase Coherence	5
Chapter 2: Ion Trapping	8
2.1 Paul Traps	8
2.2 Optical Molasses	16
Chapter 3: Atomic Physics	21
3.1 Atomic Excitation	21
3.2 Quadrupole Transitions	28
Part II: Trapping Barium Ions	34
Chapter 4: Atomic Structure of Barium Ion	35
Chapter 5: Apparatus	40
Chapter 6: Loading and Ionization	46
6.1 Ionization	46
6.2 Isotope Selectivity	47
Chapter 7: Laser Cooling	52
7.1 Cooling Scheme	52
7.2 Laser Stabilization	54
Part III: Realization of Qubit Operations	62

Chapter 8:	Optical Pumping	63
Chapter 9:	Qubit Rotation	68
9.1	Hyperfine Qubits	68
9.2	Optical Qubits	70
Chapter 10:	Readout	72
10.1	Basics	72
10.2	Selective Excitation	76
10.3	Deshelving	77
Chapter 11:	Stabilization of Fiber Laser	80
11.1	Motivation	80
11.2	Setup	82
11.3	Results	95
11.4	Conclusions and Outlook	99
Bibliography	101

LIST OF FIGURES

Figure Number	Page
1.1 The Bloch sphere	5
2.1 Cartoon of an ion confined in a Paul trap	9
2.2 Simulation of secular frequency sidebands on a trapped ion	11
2.3 Ion trajectories in the pseudopotential limit, with and without excess micro- motion	13
2.4 The effect of micromotion on an atomic resonance	15
2.5 The effect of excess micromotion on Doppler cooling	19
3.1 Rabi oscillations and detuning	22
3.2 Avoided crossing, adiabatic and diabatic curves	23
3.3 Simulation of adiabatic passage and effectiveness of the Landau-Zener model	25
3.4 Adiabatic passage as imaged on the Bloch sphere	27
3.5 The far field radiation patterns for a quadrupole radiation source	30
3.6 The polarization of radiation for a quadrupole radiation source	31
4.1 Generic diagram of ion energy levels, with and without D states	37
4.2 The level diagram of $^{137}\text{Ba}^+$	39
5.1 A 3D model of our trap design, not to scale.	41
5.2 Cross sectional schematic of linear Paul trap	42
5.3 Ray diagram of the optical setup	43
5.4 A block diagram of the laser setup.	44
6.1 Level Diagram of Neutral Barium	48
6.2 Isotope selective photoionization rates	49
6.3 Doppler broadening of a neutral barium atomic beam as a function of angle and temperature.	50
7.1 Theoretical strengths and frequencies of various 650 nm repump transitions in $^{137}\text{Ba}^+$	53
7.2 Doppler free saturated absorption setup	54
7.3 Schematic of wavelengthmeter based lock concept	58

7.4	Wavelengthmeter frequency drift versus atmospheric pressure	59
7.5	Attempt to use secular axial sidebands to measure the absolute ion temperature	60
8.1	Relative Transition Strengths of π transition in the D1 line	64
8.2	Optical pumping effectiveness as function of correction coil current	65
8.3	Magnetic coil configuration	66
8.4	Demonstration of optical pumping using the 1762 nm laser	67
9.1	RF Rabi flops	69
9.2	Optical Rabi flop	71
10.1	Confidence interval of readout versus time in absence of noise	73
10.2	Histogram of events from an experimental run	74
10.3	Detection infidelity versus time in presence of noise	75
10.4	Adiabatic passage efficiency as a function of sweep time	77
10.5	Circuit diagram of analog ramp generator.	78
10.6	Optical setup of the adiabatic passage system	79
11.1	Temperature stabilization of Zerodur cavity versus room temperature	81
11.2	Circuit diagram of temperature controller	83
11.3	Longitudinal study of cavity stability	85
11.4	High resolution demonstration of frequency stability	85
11.5	Abstract block diagram of a generic PDH system	86
11.6	The I/Q Plane	87
11.7	Circuit diagram of PDH system	89
11.8	Circuit diagram of the microcontroller based servo mechanism.	90
11.9	Fiber laser response function and piezo resonances	92
11.10	Group delay in microcontroller based laser lock	93
11.11	Fiber laser noise spectrum	96
11.12	Power broadening of 1762 nm transition	98

LIST OF TABLES

Table Number	Page
4.1 A summary of various qubit candidates	36
7.1 A correlated list of Te_2 Doppler free and Ba^+ resonances	56

ABBREVIATIONS

ADC Analog to Digital Converter. Accepts an analog voltage and converts it into a digital sequence whose value is proportional to the input voltage.

AM Amplitude Modulation. A periodic signal whose amplitude is varied periodically over time.

AOM Acousto-Optic Modulator. Creates a diffracted laser beam from an input beam and RF signal whose frequency and phase is the sum or difference of the two inputs. Turning off the RF will cause the diffraction to cease, which allows an AOM to act as a shutter. The angle of diffraction also depends on RF frequency.

CCD Charge Coupled Device. Refers to a method of iteratively shifting the charge stored on one semiconductor diode to its neighbor. Usually used colloquially to refer to a camera made from an array of such photosensitive diodes.

DAC Digital to Analog Converter. Accepts a digital signal and outputs an analog voltage proportional to the digital value provided.

DAQ Data Acquisition Board. A type of computer expansion card that is specialized to the collection of scientific data.

DDS Direct Digital Synthesizer. A type of radio frequency synthesizer which operates from a DAC that reads its output value from a lookup table.

DPAOM Double Passed AOM. An AOM in a configuration where the laser is first sent through the AOM once, and then one diffracted beam is selected and retroreflected to pass through the same AOM again. This causes the net deflection to be independent of frequency, so that the AOM can be used to shift and tune the laser's frequency but not angle.

DSP Digital Signal Processor. A kind of microprocessor which is focused on the rapid processing of digital data converted to or from an analog signal. Can also refer to digital signal processing, which is the field of processing said digital data.

ECDL External Cavity Diode Laser. Ordinarily, the cleaved surface of a laser diode provides sufficient back reflection to generate a poorly coherent light source. By introducing a second, stronger back reflection outside of the laser diode, a much narrower laser can be achieved. This external cavity is usually formed with a diffraction grating to provide frequency control.

EOM Electro-Optic Modulator. A device containing a transparent crystal whose index of refraction depends on the strength of the local electric field. By feeding an EOM an RF electric field, an effective frequency modulation can be applied to a transiting laser beam.

FM Frequency Modulation. A periodic signal whose frequency is changed over time. For a sinusoidal signal and modulation, is equivalent to phase modulation. Modulation depth is the amount by which the carrier frequency is changed, while modulation frequency is the frequency of that change.

FPGA Field Programmable Gate Array. An integrated circuit containing a large number of basic digital logic circuits which can be programmed with a computer to be interconnected in almost arbitrarily flexible ways.

FSR Free Spectral Range. The distance, measured in Hz, between longitudinal modes of an optical cavity. The mode structure of a cavity repeats every FSR.

FWHM Full Width Half Maximum. The width of a peak measured from the point on one side where the value is equal to half of the the peak's maximum value to the corresponding point on the other side.

GPIB General Purpose Interface Bus. A complicated parallel bus protocol specified by IEEE-488 commonly used for scientific instrumentation. Originally known as HPIB, Hewlett Packard Interface Bus.

LED Light Emitting Diode. A diode whose bandgap and optical properties have been adjusted to emit light when current is passed through it. Usually meant to imply an incoherent light source, as opposed to a laser diode, which functions similarly, but emits coherent light.

NA Numerical Aperture. One measure of the light collection ability of a lens, equal to $n \sin \theta$, where n is the index of refraction of one side of the lens and θ is the opening angle from an object at the focus to the entrance pupil of the optical system.

PDH Pound-Drever-Hall. A method of obtaining an error signal from a cavity resonance interferometrically by measuring the amplitude of the reflected light. Requires modulation of the incident laser.

PMT Photo-Multiplier Tube. A series of electrically charged plates that relies on the photoelectric effect to convert a photon into an electron, and then by means of a cascade effect, amplifies that electron into an easily measured amount of charge.

RF Radio Frequency. A wide range of electromagnetic frequencies accessible to conventional electronics, ranging from 3 kHz to 3 THz. Frequencies above 300 MHz are usually referred to as microwaves rather than RF.

SNR Signal to Noise Ratio. The ratio of relevant signal strength to the net total of all underlying noise sources. Properly specified within some bandwidth, and usually measured in dB.

UHV Ultra-high vacuum. A level of vacuum that can only be achieved by baking the entire system at high temperature for an extended period of time. Usually understood to be

better than 10^{-9} Torr.

UV Ultraviolet. The nominally invisible part of the electromagnetic spectrum just higher in frequency than the bluest visible light. Extends in wavelength from about 400 to 10 nm.

VCO Voltage Controlled Oscillator. A device that outputs a signal whose frequency is proportional to an analog input voltage.

ACKNOWLEDGMENTS

I would like foremost to thank my parents, who have worked tirelessly and made inestimable sacrifices to provide me with the many opportunities that have paved my life. What has been done here is as much their accomplishment as my own. I regret that my father could not be here to enjoy our hour of triumph, as he passed away just a few months ago, and is sorely missed. This one's for you, Dad.

Of course none of this would be possible without my teacher, advisor and friend Boris Blinov. Besides from being a generally swell guy, Boris brings energy and new life into everything he does; his creativity and vigor never cease to amaze. He has been my companion for these past 4 years, he *willingly* shared with me many of the hardships of graduate school life; long nights and weekends, uncertainty and frustration. Throughout he maintained enduring confidence and a steady vision. He has also been amazingly supportive far above and beyond any call of duty, and I am profoundly grateful.

Of special import are my comrades-in-arms Nathan Kurz, Gang "Rick" Shu and Adam Kleczewski. I am in constant consultation with all three of them, and it is nearly impossible for me to select any project which is untouched by one of their ideas, sweat, or actual blood. I would like to give special thanks to Li Wang, with whom I was nearly inseparable in the early parts of this project. Also it was nice of Jeff Sherman to let us (repeatedly) hijack his trap back in the days when ours didn't work.

In the following pages I shamelessly reproduce the efforts of a veritable army of undergraduates and graduate students I've had the privilege of working with over the years. People such as Joanna Salacka, Aaron Avril, Kalista Smith, Gary Howell, Ryan Bowler, Joseph Pirtle, Viki Mirgon, Tom Noel, Eric Magnuson, Sanghoon "Hoony" Chong, Edan Shahar, Peter Greene, Chris Dostert, Frank Garcia, Jennifer Porter, Anya Davis, and Corey Adams greatly enriched my life and taught me much about physics and teaching. I hope I

was able to return the favor in kind.

Last but not least, I also appreciate the efforts of my reading committee, Boris, Subhadeep Gupta, and Dave Bacon for being crazy enough to read this thing, and generous in offering comments. Thanks!

Part I

THEORETICAL PRELIMINARIES

Chapter 1

QUANTUM COMPUTING

Quantum computing is a paradigm of computing in which certain features of quantum mechanics are leveraged to make possible new algorithms that cannot be simulated efficiently on a classical Turing machine. That is, the scaling law of quantum algorithms that solve certain problems is better than any known modern algorithm that solves the same problem. Although this does not appear to reduce the complexity of NP complete problems, there are several other important problems that are known to have significant improvements in a quantum regime over the classical one. A few famous examples are Shor's factoring algorithm [61] and Grover's database search algorithm [25].

One part of the quantum computer's advantage is superposition. The fundamental unit of information in a quantum computer is a *qubit*, which is physically implemented by any two level quantum system. A qubit is allowed to take on any superposition of the form $\alpha|0\rangle + \beta|1\rangle$. This is in contrast to a classical bit, which must at all times be exactly 0 or 1. So while a bit can take on but 2 values, a qubit can be any one of an infinite number of values. Now, this very concept is already problematic, since the proposal is very much like an analog computer, where the fundamental unit of information is an analog voltage. Analog computers lack the basic error correction protocols which are integral to the great strength of digital logic. Fortunately, there exists the field of *quantum error correction*, wherein the redundant storage of quantum information is used to protect against specific forms of noise, or decoherence [49]. Quantum error correction makes the dream of quantum computing plausible.

If this were the only advantage of a quantum computer, then it would be a form of probabilistic automata [54] and provide little advantage over modern computing systems. However, quantum computers have an additional advantage which is unavailable to any classical machine - entanglement. Consider the state $(|11\rangle + |00\rangle)/\sqrt{2}$. This is a probabilistic

statement together with an absolute conditional on the relationship between two qubits that requires no active calculation on the part of the CPU to enforce. Specifically, either qubit can be found in either state with equal probability, but they will always be found in the same state. It is this absolute conditional combined with the probabilistic one that cannot be simulated efficiently on a classical computer. That fact is enshrined in Bell's inequality [3], which teaches us that the correlation between two entangled objects is greater than any possible classical correlation in the absence of communication. Since on a computer this communication requires actual intervention on the part of the CPU, the resolution of a complex network of conditionals can always be done more efficiently on a quantum computer than a classical one. It is unclear that this mechanism can really provide the exponential speedup that appears to be possible with a quantum computer, although it is clear that entanglement is an important resource in quantum computing.

Any qubit candidate must exhibit a full set of *universal quantum gates* [13]. This is any set of basic gates, which together can perform any algorithm possible on a quantum computer. Formally because of the infinite number of available quantum states one of these sets is usually infinite, but can usually be reduced to a small number of classes. Ordinarily, the universal gate set can be further subdivided into gates that operate on a single qubit and those that operate on two or more qubits. The former class is used for the generation of superpositions, while the latter class is necessary for the generation of entanglement. The single qubit gates are usually $\sigma_x(\theta)$ and $\sigma_z(\theta)$, rotations about the x and z axes of the Bloch sphere discussed below. Because θ can take on any value, this class of gates is technically infinite, although it is usually considered sufficient to demonstrate a small number of such rotations. The rotation $\sigma_x(\theta)$ corresponds to a rotation between qubit levels, e.g. $|0\rangle \rightarrow \cos(\theta)|0\rangle + \sin(\theta)|1\rangle$. Then $\sigma_z(\theta)$ rotations corresponds to a phase shift, e.g. $(|0\rangle + |1\rangle)/\sqrt{2} \rightarrow (|0\rangle + \exp(i\theta)|1\rangle)/\sqrt{2}$. There are a fair number of known multiple qubit gates that constitute full sets, but the most popular is a controlled not, or CNOT, gate. In a CNOT gate, the second qubit has a NOT operation, or $\sigma_x(\pi)$, performed on it if the first qubit is 1, and nothing is done if the first is 0. A CNOT gate together with the two aforementioned single qubit rotations constitute a universal quantum computer.

There are many plausible candidates for a physical representation of qubits, such as

quantum dots, superconducting qubits, and nitrogen vacancies in diamond to name a few. In this work we study $^{137}\text{Ba}^+$ as a trapped ionic qubit, specifically a hyperfine qubit, although a brief detour into the world of an optical qubit is entertained. In a hyperfine qubit, the qubit information is stored in the form of two hyperfine levels in an ion. Qubit rotations can be performed using resonant microwaves or laser Raman transitions. The proposals for multiqubit operations are manifold, but a few popular ones include the Cirac-Zoller phonon coupling scheme [9], the NIST geometric phase gate [37], the Sørensen and Mølmer high temperature gate [65], and the García-Ripoll ultrafast gate [19]. In this work, we demonstrate single $^{137}\text{Ba}^+$ qubit initialization, rotations and readout. Future plans include implementation of the García-Ripoll style gate for two qubit interactions, as well as ion-photon [6] and remote ion-ion [42] entanglement, for applications such as loophole free Bell’s inequality tests [64].

The most naive way to perform single qubit rotations on ionic qubits is to simply drive the microwave hyperfine transition directly. This is a convenient and effective method. However, since the centimeter scale diffraction limit of such radiation is enormous compared to the spacing of ions in a Paul trap, it cannot easily be used to drive transitions on a single qubit while leaving its neighbor unchanged. A more appropriate method is to drive the transition using two lasers detuned by an amount equal to the hyperfine splitting, and both far detuned from any electronic transition. This is known as a Raman transition [18, 35]. Since this system uses laser light instead of microwaves, the beams can be focused tightly, allowing the researcher to drive only one ion at a time. Furthermore, because the beam is being focused, the radiation intensity is higher and so the required rotation time is generally less for Raman transitions than with microwaves. The technique is frequently limited by the AC Stark effect, where, because of the high intensities involved, the frequency of the hyperfine splitting is altered slightly by an amount related to the laser intensity. In this way laser intensity noise couples into the qubit and causes decoherence. It is much more difficult to stabilize the intensity of a laser than its frequency. This effect can be mitigated by using lasers at the “magic wavelength” where the Stark effect due to two nearby transitions approximately cancel.

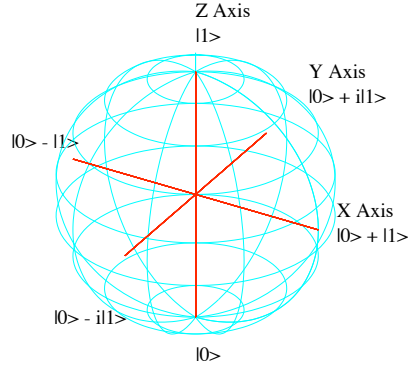


Figure 1.1: The Bloch sphere. The z axis represents the population inversion, -1 to 1, while the xy plane contains phase information. The entire globe should be imagined rotating around its axis at a rate equal to the qubit's energy splitting.

1.1 Bloch Spheres and Phase Coherence

There is a graphical way to represent a two level quantum state known as the *Bloch sphere*, which is almost exactly analogous to the venerable Poincaré sphere representation of the polarization of light [7]. Consider the most general pure state of a two level system with eigenstates separated by energy E ,

$$|\psi\rangle = \sin(\theta/2)|0\rangle + \cos(\theta/2)e^{i\phi_0}e^{-iEt/\hbar}|1\rangle \quad (1.1)$$

$$\equiv c_0|0\rangle + c_1e^{-iEt/\hbar}e^{i\phi_0}|1\rangle \quad (1.2)$$

The ability to write this in terms of θ and ϕ_0 motivates our desire to represent this state on a sphere of radius unity, and they are the spherical coordinates of a state vector on the Bloch sphere. But there is a problem, the presence of an energy splitting causes the phase ϕ effectively to increase with time. In terms of the Bloch sphere, this corresponds to an azimuthal rotation with frequency E/\hbar . Although the states $|0\rangle$ or $|1\rangle$ are unaffected

by this rotation, the state vector $(|0\rangle + |1\rangle)/\sqrt{2}$ will rotate rapidly around the sphere, and eventually knowledge of its phase will be completely lost to the observer.

If we introduce an interaction $H_I = \Omega \cos(\omega t + \phi_{\text{ext}})$, with Ω being the Rabi frequency, ω the field's oscillation frequency, and ϕ_{ext} an arbitrary phase, then after applying the rotating wave approximation the equations of motion are given by

$$i\dot{c}_0 = \frac{\Omega}{2} e^{i(\omega - E/\hbar)t} e^{i(-\phi_0 + \phi_{\text{ext}})} c_1 \quad (1.3)$$

$$= \frac{\Omega}{2} e^{i(-\phi_0 + \phi_{\text{ext}})} c_1 \quad (1.4)$$

$$i\dot{c}_1 = \frac{\Omega}{2} e^{-i(\omega - E/\hbar)t} e^{i(\phi_0 - \phi_{\text{ext}})} c_0 \quad (1.5)$$

$$= \frac{\Omega}{2} e^{i(\phi_0 - \phi_{\text{ext}})} c_0 \quad (1.6)$$

where we choose $\omega = E/\hbar$. We see that ϕ_0 and ϕ_{ext} always appear together, and in fact only their difference is physically meaningful. This suggests a useful picture of how the Bloch sphere operates - as the qubit phase advances, its state vector rotates azimuthally around the Bloch sphere at a rate equal to the state splitting. But as the driving field phase advances, so does the coordinate system on which the state vector lies also rotate, so that as long as the two proceed at the same frequency, the state vector is seen as stationary on the Bloch sphere. So from a practical standpoint, the Bloch sphere only has useful meaning in context of the stability of an available resonant clock that can keep track of the ever slipping phase. Notice that the clock doesn't actually need to be exposed on the qubit to be doing its job, since during the exposure the clock's instantaneous phase contributes to the interaction energy, i.e.,

$$|\psi\rangle = \sin(\theta/2)|0\rangle + \cos(\theta/2)e^{i\phi_0} e^{-i(Et/\hbar + \phi_{\text{ext}}(t))}|1\rangle \quad (1.7)$$

$$= \sin(\theta/2)|0\rangle + \cos(\theta/2)e^{i(\phi_0 - \phi_{\text{ext}})}|1\rangle \quad (1.8)$$

for a resonant clock. Thus, all that is required is for the clock's phase to be stable with respect to the qubit's own phase while "offline". When later exposed onto the qubit to drive a rotation, the qubit will behave as if its phase had never changed at all. In some sense,

the function of the clock is to remember the qubit's phase during the quantum calculation. Phase incoherence of the clock results directly in dephasing of the qubit. One can imagine that the x axis of the Bloch sphere rotates along with the clock's phase while the qubit state vector rotates along with the qubit, as long as these relative phases do not slip, then the Bloch sphere remains unchanged.

Thinking about the reference clock in this way makes clear the correct way to perform σ_z rotations. In this picture, a σ_z rotation is just a change to the total phase $\phi = \phi_0 - \phi_{\text{ext}}$, which includes the clock's phase. Thus, a $\sigma_z(\Phi)$ rotation is accomplished by simply decreasing the clock's phase by an amount Φ . It might seem strange that the qubit's properties can be changed by affecting the external clock, but keep in mind that any interference experiment on the qubit's superposition will require the clock to drive transitions. To build a qubit, we see that it is necessary to have excellent control over a clock's phase, which must be independently stable to avoid dephasing. A qubit is only as good as its clock. Of course, the clock isn't the only place where phase slipping can occur. If any undesired interaction causes an energy shift between the two qubit levels unbeknownst to the experimenter, then the qubit's own clock can be unstable, and the its phase will slip with respect to the external clock. There is something of a catch 22 involved here, a good qubit interacts strongly with the things the experimenter wants it to interact with, and not at all with anything else.

Chapter 2

ION TRAPPING

2.1 *Paul Traps*

It is, to the great disappointment of fusion advocates, impossible to suspend a charged particle in free space using electrostatic forces alone. This is the content of Earnshaw's theorem, which simply makes the observation that an electrostatic field with this ability would look like a harmonic well in all 3 directions. But, since any electrostatic potential field must obey Laplace's equation

$$\begin{aligned}\nabla^2\phi &= \nabla^2\left(\alpha x^2/2 + \beta y^2/2 + \gamma z^2/2\right) \\ &= \alpha + \beta + \gamma \\ &= 0\end{aligned}$$

has no solution where all three spring constants α , β , and γ are positive. Thus, at least one direction must be a potential maximum rather than a minimum. The best we can manage is a saddlepoint.

An ion at the saddlepoint of a rapidly rotating electric quadrupole potential behaves, to lowest approximation, as if it were in an electrostatic harmonic potential. To understand this, one might imagine what happens to a particle at the saddlepoint of a static quadrupole field - naturally, it falls down the slope. But what if, before the particle has an opportunity to move very far, the sign of the quadrupole field is flipped, so what was once a valley is now a hill. Now the particle can no longer escape by its previous route, and must change directions. But then repeat the process over and over, and the ion can never move very far before it is "saved" by the oscillating quadrupole field. In this way, an oscillating quadrupole field is able to trap a charged particle in free space, see figure 2.1. A trap that suspends a charged particle by application of this principle is called a Paul trap. The

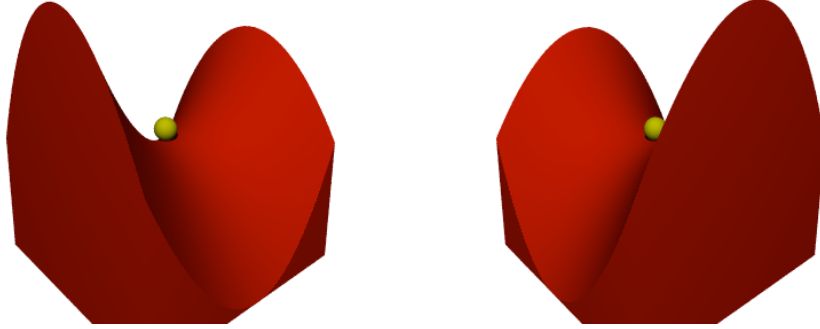


Figure 2.1: Cartoon of an ion confined in a Paul trap. In the first image, the ion will begin to fall to the right, but before it is able to move very far, the quadrupole changes to the second image, and begins to fall to the left.

oscillating quadrupole field is obtained in practice through the application of high voltage RF to electrodes in ultrahigh vacuum.

There are several features of the particle's motion we can expect immediately from the above description. First, it will have some free oscillation of its own, which will most closely resemble harmonic motion, since the time averaged force it feels is at a minimum at the saddlepoint, where the ion can come to a rest. The frequency, known as the secular frequency, of that harmonic well should be some function of the quadrupole slope and the oscillation frequency. As the slope increases, so should the harmonic frequency, but it should decrease as the oscillation frequency increases. One can understand this from considering the limit of an extremely fast oscillating field, where the field changes so rapidly that the ion can only experience a time averaged effect, which is everywhere zero. Second, there will be motion caused by the quadrupole as its rotation pushes the ion around. This motion is driven by the rotating field itself and will occur at the frequency of quadrupole oscillation. This is known as micromotion.

In order to account for the possibility of a fixed DC field, the most general potential field of interest can be written as [36]

$$\Phi = \frac{U}{2} (\alpha x^2 + \beta y^2 + \gamma z^2) + \cos(\omega_{\text{rf}} t) \frac{U'}{2} (\alpha' x^2 + \beta' y^2 + \gamma' z^2), \quad (2.1)$$

Where U and U' are electrostatic potentials, ω_{rf} is the oscillation frequency of the Paul trap, and the various Greek constants describe the shape of the trapping potential. We will consider that this potential acts on a particle of charge Ze and mass m . Also, for simplicity, we will separate the problem and consider only the x axis. In this case, it is possible to write the resulting equation of motion in the standard form of Mathieu's equation

$$\frac{d^2x}{d\zeta^2} + [a_x - 2q_x \cos(2\zeta)]x = 0, \quad (2.2)$$

with the definitions

$$\zeta \equiv \frac{\omega_{\text{rf}}t}{2} \quad a_x \equiv \frac{4ZeU\alpha}{m\omega_{\text{rf}}^2} \quad q_x \equiv \frac{2ZeU'\alpha'}{m\omega_{\text{rf}}^2}. \quad (2.3)$$

The analytic solution to Mathieu's equation can be found using the Floquet theorem, and in its most general form is not especially useful. The gist is that the solution can be described by the infinite set of constants C_{2n} and another constant β_x . The easiest way to see the connection with our earlier qualitative argument is to make an extremely common approximation, where $a_x \ll 1$ and $q_x^2 \ll 1$, which is equivalent to assuming that only C_0 and C_2 are significant. This is the lowest order approximation, and can be thought of as the pseudopotential approximation, since it is in this regime that imagining that the ion lives in a DC harmonic well makes sense. In this case the solution is

$$x(t) = 2AC_0 \cos\left(\beta_x \frac{\omega_{\text{rf}}}{2} t\right) \left[1 - \frac{q_x}{2} \cos(\omega_{\text{rf}}t)\right] \quad (2.4)$$

$$\beta_x = \sqrt{a_x + q_x^2/2}, \quad (2.5)$$

where A is an initial conditions that sets the size of secular oscillation. In these equations we see a direct connection to physical intuition. There is one part, $\cos(\beta_x \omega_{\text{rf}}t/2)$, which dominates the behavior, that looks like normal harmonic motion having frequency $\omega_s = \beta_x \omega_{\text{rf}}/2$. At first glance, this appears to contradict our previous assertion that ω_s ought to decrease with the oscillation frequency. However, there are two relevant regimes for β_x . In one, a_x dominates, and from equations 2.3, we see that overall $\beta_x \omega_{\text{rf}}$ is independent of RF frequency. But from the definition of a_x , we see that this actually means that the trap

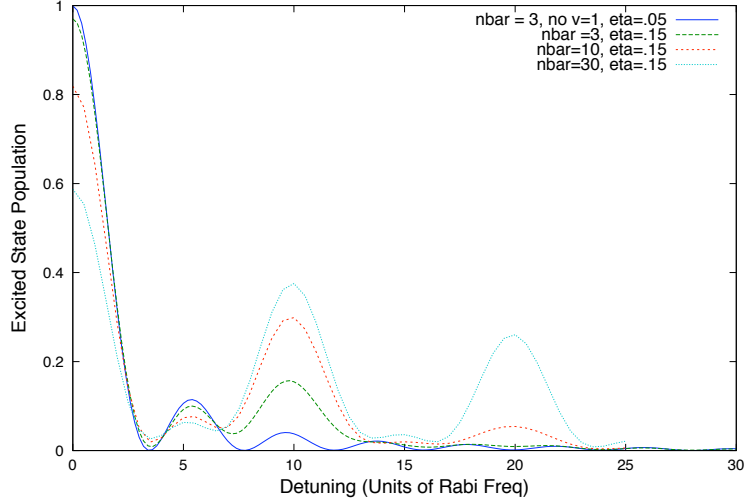


Figure 2.2: A full simulation of the effect of Doppler shifts on a coherently driven atomic resonance. On this scale, the Rabi frequency is unity, and the secular frequency is 10. Note that when the ion is at rest, it is easy to see fringes from the laser’s coherence, and then as η becomes larger, the modulation peaks become more prominent. “nbar” is the thermal average occupation number, as defined in equation 2.17.

is dominated by a DC quadratic potential, in which case the RF frequency ought to be irrelevant. In fact, equation 2.4 reduces to the usual form of quadratic potential, since q_x is small, with

$$\omega_s = \sqrt{\frac{ZeU\alpha}{m}}. \quad (2.6)$$

In the other case, q_x dominates, and $\beta_x \omega_{\text{rf}} \propto 1/\omega_{\text{rf}}$. So in the pseudopotential approximation, $\omega_s \propto \omega_{\text{rf}}^{-\kappa}$ with $\kappa \in [0, 1]$. Now, the remaining term does not contain anything but ω_{rf} as its frequency, and so is the promised micromotion, proportional in amplitude to the q_x parameter. It should be stressed that this discussion is only really accurate in the lowest order approximation. In general, the exact solution will still have an identifiable secular frequency ω_s , but outside of the region where $C_4 \approx 0$, the dependence of ω_s on ω_{rf} will be stronger than ω_{rf}^{-1} .

We would like to consider the effect of Doppler shifts caused by the trapped ion’s motion on a nearly resonant laser. Ordinarily, a thermal particle exposed to resonant laser light

will have its resonance broadened by its time averaged random distribution of velocities. However, a lone ion in a Paul trap does not have a random distribution of velocities, it is restricted to oscillate at the secular trap frequency ω_s or ω_{rf} . Thus, the resonance itself is not Doppler broadened at all, but instead exhibits additional peaks spaced at intervals of ω_s and ω_{rf} from the central, carrier resonance. The strength of this effect is parameterized by the spatial extent of ion excursions multiplied by the laser's wavenumber, or $\eta = kx_0 \approx 2kAC_0$, known as the *Lamb-Dicke parameter*. A simulation of this effect can be seen in figure 2.2, where the ion's classical motion is fully simulated by integrating the Mathieu equation, and the ion-laser interaction is obtained by integrating the master equation for the semi-classical interaction Hamiltonian.

A very simple analysis can be performed to quickly quantify and understand this effect. Consider for a moment only the ion's secular motion in one dimension, which by the previous definitions has an amplitude of η/k . The Doppler shifted laser field is then described in the rest frame of the ion by

$$E(t) = \text{Re} \left\{ E_0 \exp \left[i \left(\int_0^t k u dt - \omega t + \phi_{\text{laser}} \right) \right] \right\}, \quad (2.7)$$

where E_0 is the field strength of the laser and u is the ion's velocity. But we have

$$u(t) = \dot{x}(t) = \frac{\eta}{k} \omega_s \cos(\omega_s t + \phi), \quad (2.8)$$

and so, with a Bessel function expansion,

$$E(t) = \text{Re} \{ E_0 \exp [i(\eta \sin(\omega_s t + \phi) - \omega t + \phi_{\text{laser}})] \} \quad (2.9)$$

$$= \text{Re} \left\{ E_0 \exp [\omega t + \phi_{\text{laser}}] \sum_{n=-\infty}^{\infty} J_n(\eta) \exp [in(\omega_s t + \delta + \pi/2)] \right\}. \quad (2.10)$$

We see then that η is best thought of as a frequency modulation index, and that the frequency sidebands occur at regularly spaced intervals of ω_s with amplitudes given by the Bessel functions $J_n(\eta)$.

The existence of these alternate resonances is interesting. Suppose we repeatedly excite an ion on one of these resonances and allow it to spontaneously decay sometime later.

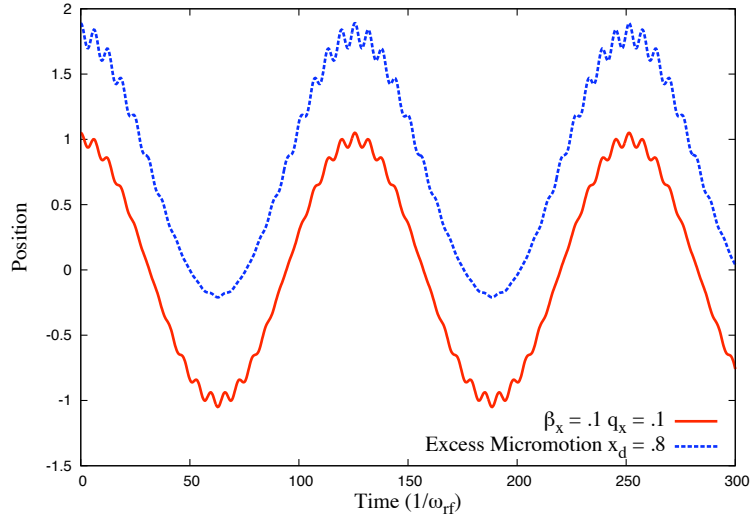


Figure 2.3: Two ion trajectories in one dimension with and without excess micromotion, displaying the slow secular motion and fast micromotion “wiggles”. Notice that the excess micromotion case has its secular motion shifted spatially and is otherwise identical to the case without excess micromotion. The micromotion wiggles are by contrast greater in magnitude and asymmetric.

Although nothing strange has happened in the frame of the ion, in the lab frame the ion has apparently absorbed a photon at one energy and emitted a photon of a different energy, because the light was emitted at a different point along the ion’s trajectory. It would seem that in the lab rest frame, energy has either been added to or removed from the ion’s motion. This line of argument has an exciting meaning in the context of a quantum mechanical treatment - each photon increases or decreases the motional quanta by one level, depending on whether the sideband was red or blue of the carrier, respectively. In order to cool an ion in this way, we must be able to resolve the secular frequency sidebands from one another, which means the secular frequency must be larger than the linewidth of the resonance. For this reason, this process is known as resolved sideband cooling.

Excess micromotion [4] is a problem that has long plagued Paul trapping. From examining equation 2.4, we see that there is a certain amount of micromotion which is fundamental to a Paul trap’s very nature. Its amplitude is proportional to q_x , which can not be reduced without decreasing the ion’s secular motion A or through β_x , which would decrease q_x as

well as ω_s . However, certain departures from ideal trap behavior can cause excess micromotion, beyond this fundamental, necessary amount. The two main causes are the presence of a DC electric field superposed on the quadrupole and also a phase difference between the RF trap electrodes. In the presence of a DC electric field, for example, the pseudopotential and DC potential together give $U = m\omega_s^2 x^2/2 - ZeEx$ which has a minimum at

$$x_d = \frac{ZeE}{m\omega_s^2}. \quad (2.11)$$

If we include the electric field into the original potential equation 2.1 and solve again, we find

$$x(t) = [x_d + 2AC_0 \cos(\omega_s t)] \left[1 + \frac{q_x}{2} \cos(\omega_{rf} t) \right]. \quad (2.12)$$

Since when we add a linear potential to the quadratic pseudopotential field we do nothing except create a new quadratic field with a new equilibrium position, the harmonic motion is not effected at all except to have a shift introduced. However, the actual RF potential $\alpha x^2/2$ added to the DC electric field gives $x_0 = ZeE/\alpha$ when the RF field is positive, and $x'_0 = -ZeE/\alpha = -x_0$ when it is negative. Thus, the RF field drives the ion from x_0 to $-x_0$ over the course of RF oscillation, which is much further than it would in the absence of an electric field. This is excess micromotion. From equation 2.12, it is seen that there is simply a new harmonic oscillation added to the already existing motion, at ω_{rf} . The effect of this motion on the ion's Doppler spectrum can be analyzed in much the same way as for the secular motion, now with modulation index $\xi = kx_d q_x/2$. The modulation index of regular micromotion by contrast is related to the Lamb-Dicke parameter η , and so can be improved by tighter confinement of the ion. To treat the excess micromotion caused by trap electrodes with out of phase RF signals, we would have to break our convention of working in 1 dimension, but the close analogy between these two causes can be easily seen. While a DC electric field causes the RF saddlepoint to oscillate along the direction of the electric field, RF dephasing causes the saddlepoint to reside at a point away from the trap's geometric center, and travel in a loop once per RF cycle. Clearly, this will drive an ion in a basically similar way to a DC electric field.

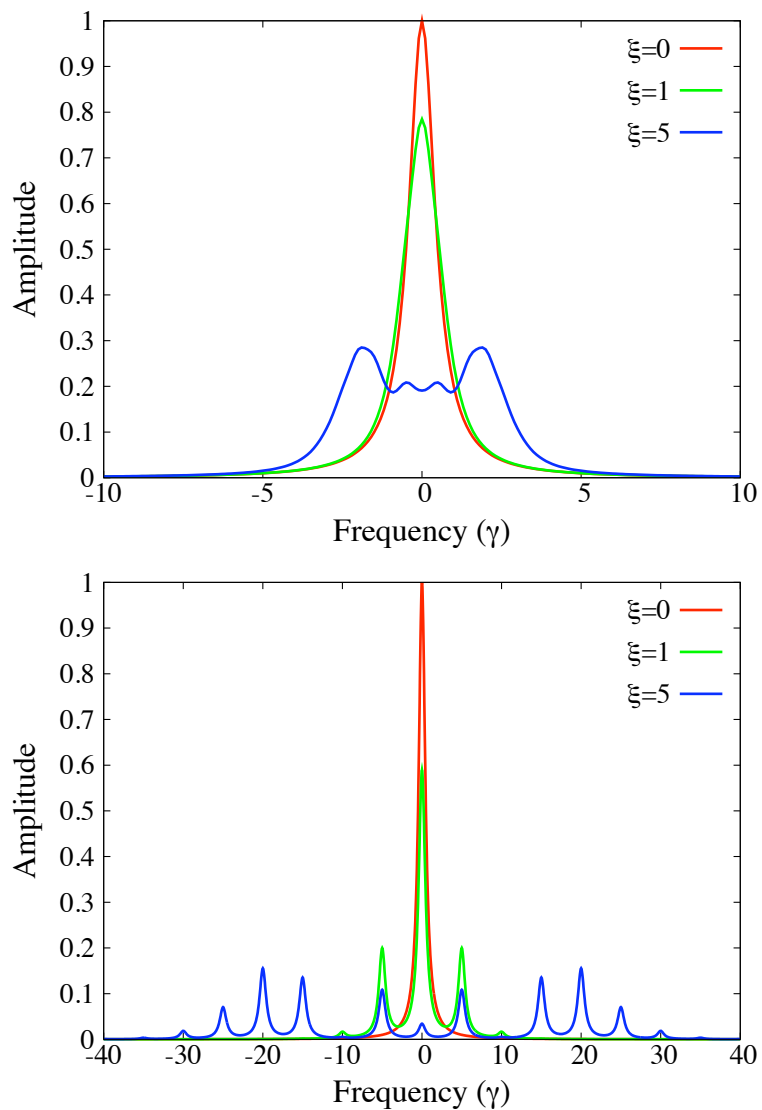


Figure 2.4: The effect of micromotion on an atomic resonance. On the left, the RF frequency is chosen to be smaller than the width of the resonance, so that the individual peaks cannot be resolved and a line blurring occurs. On the right, the RF frequency is chosen to be large, so that the individual peaks can be seen.

Note that regular micromotion and secular motion are coupled together in both equations 2.4 and 2.12. This stands to reason, since if the ion is perfectly at rest at the saddlepoint in an environment without excess micromotion, then it remains perfectly at rest, since the RF quadrupole never needs to push it back towards the center. However, we can see that excess micromotion and secular motion are completely decoupled in equation 2.12. Going back to the previous example, this can be understood because the same ion at rest would always be disturbed by the shifting saddlepoint location, no matter where it is placed. For this reason, it is frequently said that excess micromotion cannot be cooled, because it is driven by the RF field, and is more a property of the trap than of the ion.

As we have seen, it is possible to approximate the behavior of an ion in a Paul trap as a harmonic oscillator with frequency ω_s . Therefore, we expect that a quantum mechanical treatment of the ion's motion should have similar characteristics. In particular, we should be able to treat the ion's motion as having discrete energy levels with equal spacing of ω_s , and we can introduce creation and annihilation operators \hat{a} and \hat{a}^\dagger for movement between these levels. This analysis has been performed in the absence of excess micromotion [36]. This connection between ionic states of motion and the harmonic oscillator makes possible a huge number of analogies between Paul traps and quantum optics. For example, ions can be prepared in quantum superpositions of oscillator state, such as coherent states and squeezed vacuum states [43]. The Cirac-Zoller scheme of quantum computation requires that the qubit ion be prepared in a Fock state, having some definite n level.

2.2 *Optical Molasses*

At first thought it might seem strange that we can make a thing colder by shining a laser at it. After all, doesn't the absorption of light increase the energy of a system? However, temperature is not simply a measure of energy, but more specifically of entropy. And the entropy of a laser is fantastically low - its state is extremely well known, as it is a coherent state with frequency precision commonly exceeding 1 ppb, and intensity that fluctuates relatively slowly at the level of a few percent, depending on the technology. And that's before active stabilization. Therefore, it should not actually be a surprise that when used properly a laser can act as an excellent thermal bath.

To cool an atom, we take advantage of the extreme nonlinearity of its resonant behavior. Operating still in our one dimensional world, imagine two laser beams of the same nearly resonant frequency counterpropagating onto an atom. Impart on the ion now some small velocity. In the atom's rest frame, the laser it moves towards is blue shifted, while the laser it moves away from is red shifted due to the Doppler effect. Consider then the radiation force on the atom due to a laser beam, it is simply the number of photons scattered per second times the momentum transferred by each photon. If the scattering rate as a function of the laser frequency is called $\Gamma(\omega)$, and we take the velocity to be in the positive direction, then the net radiation force can be written

$$F = \hbar k [-\Gamma(\omega + kv) + \Gamma(\omega - kv)], \quad (2.13)$$

and if the Doppler shift kv is small, then

$$\begin{aligned} F &\approx \hbar k \left[2kv \frac{d\Gamma}{d\omega} \right] \\ &= -2\hbar k^2 v \frac{d\Gamma}{d\omega} \\ &\equiv -\kappa v. \end{aligned} \quad (2.14)$$

That is, the ion motion is damped by a force proportional to the resonance slope and the velocity. Now, since the resonance has a positive slope on the low frequency, or red, side, the force decreases the atom's velocity if the lasers are tuned to this side. But on the high frequency, or blue, side of the resonance, the slope is negative, and so the force exponentially increases the atom's velocity if the laser is tuned to a frequency above the resonance. In the cooling case, the dampening behavior is extremely reminiscent of viscous drag, and the analogy can be brought even further.

Clearly, this process cannot proceed uninterrupted forever. This is because the quantum nature of the light-atom interaction causes the the atom's behavior to be repeatedly jostled by finite, discrete impulses. The effect is manifested by the fact that energy is absorbed by the ion in quanta of one photon. This means that in equilibrium, the atom's motion resembles Brownian motion, and we expect from the fluctuation-dissipation theorem that

there should be some residual temperature in equilibrium. The energy dissipation due to the above cooling process is given by $\dot{E}_{\text{cool}} = Fv = -\kappa v^2$, while the energy introduced by scattering is given by $\dot{E}_{\text{heat}} = \dot{E}_{\text{abs}} + \dot{E}_{\text{em}} = 2\dot{E}_{\text{abs}}$. That is, the heating rate is given by the rate of heating due to absorption plus the rate of heating due to emission. In a true 1D model, these will be equal since spontaneous emission is confined to the line, although in 3D the heating rate will in general be less. The heating rate is given by

$$\dot{E}_{\text{heat}} = 2\dot{E}_{\text{abs}} = 2\frac{\hbar^2 k^2}{2m}(2\Gamma), \quad (2.15)$$

where m is the mass of the ion, and we have 2Γ due to the two lasers. In equilibrium, $\dot{E}_{\text{heat}} = \dot{E}_{\text{cool}}$, under which condition we have $\langle v^2 \rangle = \hbar\Gamma/(m\Gamma')$ so the equilibrium temperature is just

$$k_B T = m\langle v^2 \rangle = \hbar\Gamma(\omega) \left[\frac{d\Gamma}{d\omega} \right]^{-1} = \hbar \left[\frac{d}{d\omega} \ln \Gamma(\omega) \right]^{-1}. \quad (2.16)$$

That is, the ultimate limit of Doppler cooling through optical molasses is inversely proportional to the resonance slope, and directly proportional to the scattering rate. It is well known that if the scattering rate for a saturable atom ($s = I/I_s$) is used, the minimum temperature is $\hbar\gamma\sqrt{1+s}/(2k_B)$ at a detuning $\omega - \omega_0 = \gamma\sqrt{1+s}/2$, where γ is the natural linewidth of the transition. This expression fails to account for certain correlation effects and a geometric modification due to emission anisotropy, but these considerations lead to relatively minor corrections [67, 39].

Although excess micromotion is largely independent of the ion temperature, it does influence our ability to perform laser cooling and collect fluorescence. This is because modulation of the absorption resonance reduces the slope and amplitude of $\Gamma(\omega)$, as seen in figures 2.4 and 2.5. There are two regimes of interest. The first is when the RF frequency is less than the transition width, in which case all the modulation sidebands blend into one another, and the result is a greatly diminished resonance with a large central plateau. This is the configuration the work described here was once in, and it has the distinctive characteristic that over a large range of laser frequencies the ion is alternately cooled and heated, but has a relatively constant fluorescence throughout. The other regime is when

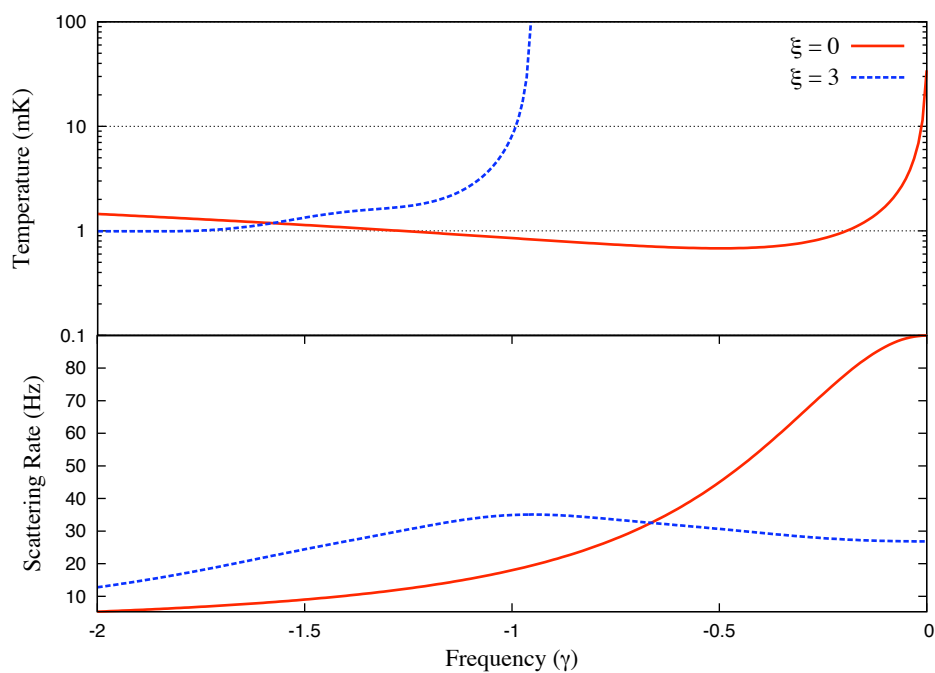


Figure 2.5: A demonstration of the effect of excess micromotion on the Doppler limited temperature of an ion driven below saturation. Observe that without excess micromotion not only is the final temperature somewhat lower, but the scattering rate (thus brightness) of such an ion at its optimal detuning is more than 4 times as high.

the micromotion sidebands are well resolved. In this case, the carrier is depleted by the presence of sidebands, but also, cooling on one transition is slightly heating on another, so that the overall cooling efficiency is greatly reduced. For these reasons, it is very desirable to eliminate excess micromotion by compensation of the original causes.

After Doppler cooling, an ion in a Paul trap will be prepared with a thermal distribution of energy levels [36]. It is significant that this must be a mixed state - although many n levels are occupied, there are no coherences in the density matrix. The figure of merit here is the average occupation number \bar{n} , given by

$$k_B T = \frac{\hbar\omega_s}{\ln\left(\frac{\bar{n}+1}{\bar{n}}\right)} \approx \hbar\omega_s\bar{n}, \quad (2.17)$$

for large \bar{n} . In order to prepare any of the interesting motional quantum states mentioned earlier, some effort must be expended to bring the ion to a definite quantum state, such as the ground state by means of resolved sideband cooling. Of course, this can only successfully be done if the secular frequency is substantially larger than the natural linewidth of the cooling transition, which is not an easily accomplished task. Other sub-Doppler laser cooling techniques, such as Sisyphus and EIT cooling can be employed but are not discussed here.

Chapter 3

ATOMIC PHYSICS

3.1 Atomic Excitation

The simplest excitation of an atomic transition is incoherent, that is, the essentially classical and probabilistic transfer of population into the excited state. In equilibrium, the ion has the same likelihood of being deexcited as excited, and so reaches a 50% excitation probability. The probabilistic excitation probability can therefore be described by

$$P_{inc}(t) = \frac{1}{2} \left(1 - e^{-B \int_{-\infty}^t \frac{I(t)}{(\omega - \omega_0)^2 + (A/2)^2} dt} \right) \quad (3.1)$$

where $A = \gamma$ and B are the Einstein coefficients, ω_0 is the transition's resonant frequency, and I is the instantaneous intensity. Here we assume that the lifetime is long enough that spontaneous decay plays no role. Incoherent excitation dominates when the ion state is measured on a time scale long compared to the phase stability of the incident radiation. Note that the the lifetime of the excited state presents a similar limit. If the phase stability of the light source is good, then it is possible to achieve coherent excitation, where it is appropriate to consider the full quantum state of the ion throughout the excitation process. The solution to the familiar Bloch equations is well known [18, 2] and leads to Rabi oscillations, described by

$$P_{coh}(t) = \frac{\Omega^2}{\Omega^2 + (\omega - \omega_0)^2} \sin^2 \left(t \sqrt{\Omega^2 + (\omega - \omega_0)^2} \right). \quad (3.2)$$

The Rabi frequency Ω is proportional to the electric field strength, or \sqrt{I} , in noted contrast to incoherent excitation, where the excitation rate is proportional to I . More importantly it is possible to achieve 100% population transfer after some time using coherent excitation unlike with incoherent excitation. Also note that as the detuning $\Delta = \omega - \omega_0$ increases, so does the oscillation frequency, but the contrast diminishes, so that full excitation is no longer possible, as seen in figure 3.1.

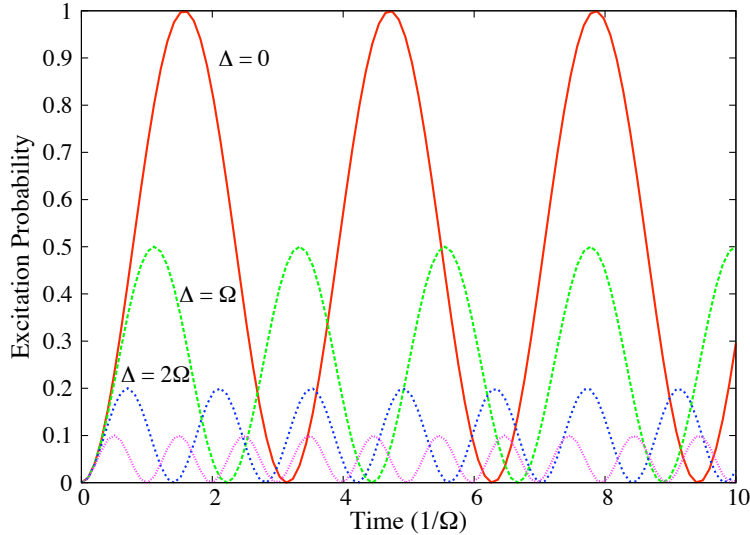


Figure 3.1: A depiction of Rabi oscillations for several values of the detuning. A detuning on the order of the Rabi frequency causes major limitations on the contrast ratio of the oscillations.

Coherent and incoherent excitation are in fact two limits of a continuous spectrum, parameterized by the ratio of radiation coherence time to Rabi frequency. If the ratio is much greater than unity, then coherent excitation can be observed, if much less than 1, then incoherent excitation. If the ratio is of order 1, the exact solution to the Bloch equations leads to dampened oscillation, with a decay time equal to the coherence time.

It should be noted that equation 3.2 depends sensitively not only on the detuning frequency but the radiation intensity. Thus, if one would like to achieve population inversion using Rabi oscillation, both frequency and power must be accurately stabilized. For microwave transitions this is not so difficult, but for lasers it can be a daunting task.

Coherent excitation can also be thought of as a solution to the Jaynes-Cummings model [20],

$$H = \hbar\omega\hat{a}^\dagger\hat{a} + \hbar\omega_0\sigma_z + \frac{\hbar\Omega}{2}(\hat{a}\sigma_+ + \hat{a}^\dagger\sigma_-), \quad (3.3)$$

where the σ operators act on the two level system, in our case an ion, and the \hat{a} operators act on the photon number of the incident field. The content of this Hamiltonian is quite

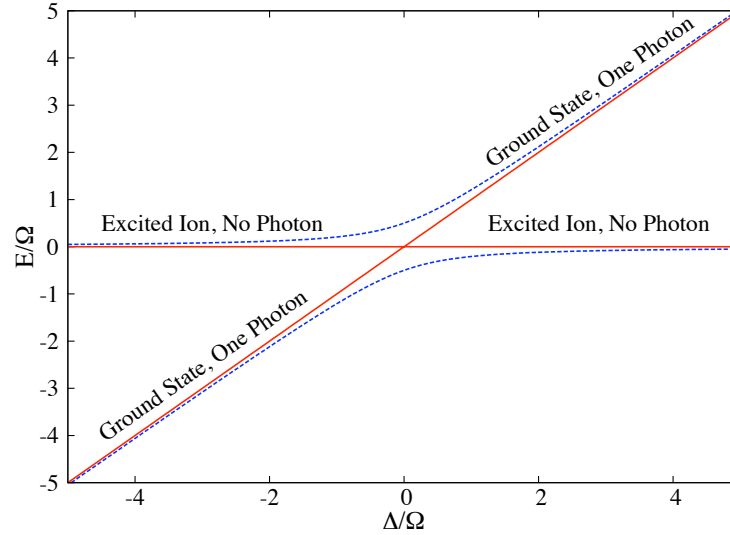


Figure 3.2: A simple demonstration of avoided crossing. The interaction strength is set to unity, and the diabatic curve is shown as a solid line, while the adiabatic curve is dashed. Notice that the separation between the adiabatic curves at their closest point is equal to the interaction strength.

direct - the total energy is equal to the energy contained in all the photons, plus the energy stored in the atomic state, plus the interaction energy.

For starters, let us turn off the interaction energy, setting $\Omega = 0$. Now, imagine we vary the photon frequency ω . Since only one photon can interact with our two level system it is acceptable to rezero the Hamiltonian energy so the energy of the excited state is zero. Hamiltonian 3.3 has two eigenstates, one associated with having an excited ion and no photon, the energy of which remains fixed, and the other having a single photon of energy ω but an unexcited ion. This latter state energy increases linearly with our varying parameter ω . These two eigenstates are degenerate when $\omega = \omega_0$, see figure 3.2.

If we make $\Omega > 0$, thereby turning on the interaction term, then the two eigenstates are coupled and instead of showing a degeneracy, the full Hamiltonian exhibits an avoided crossing, as seen in figure 3.2. The eigenstates can be easily obtained by diagonalizing equation 3.3, and are

$$E_{\pm} = \frac{\hbar}{2} \left[\Delta \pm \sqrt{\Delta^2 + \Omega^2} \right]. \quad (3.4)$$

In the limit that the detuning is very large compared to the Rabi frequency, then equation 3.4 can be written as

$$E_{\pm} = \frac{\hbar}{2} \left[\Delta \pm \left(\Delta + \frac{\Omega^2}{2\Delta} \right) \right], \quad (3.5)$$

and if we associate the extra factor of Δ to the energy of the photon, the energy of the ionic state is shifted by an amount

$$E_{st} = -\frac{\hbar\Omega^2}{4\Delta}, \quad (3.6)$$

which is the usual form of the ac Stark shift.

The adiabatic approximation for a time dependent Hamiltonian [23] applies in situations where the Hamiltonian evolves slowly compared to the system's own evolution but quickly compared to any decohering effects. In this limit, the system evolves smoothly along an eigenstate of the instantaneous Hamiltonian, that is, the ‘‘adiabatic’’ curves of figure 3.2. This stands in contrast to the sudden approximation, where the system has no opportunity to change at all and remains in its initial state throughout the Hamiltonian's evolution, moving along the diabatic curve.

The physical implementation of this procedure is straightforward, we simply sweep the laser's frequency from one side of the resonance to the other at a rate slow compared to the Rabi frequency. The important thing to note about this procedure is that after simply sweeping the frequency ω , we have moved from the asymptotic eigenstate containing 1 photon and a ground state ion to the eigenstate containing 0 photons and an excited ion. That is, the ion is transferred smoothly and completely into the excited state. The process is largely insensitive to the exact value of Ω or ω_0 . This technique is robust and has been used in many atomic systems [73, 76, 17].

The preceding discussion has been largely a steady state one. Studies of the dynamics of adiabatic transfer has led to useful results, the most important being the Landau-Zener model, where the frequency sweep begins an infinite distance away and ends infinitely on

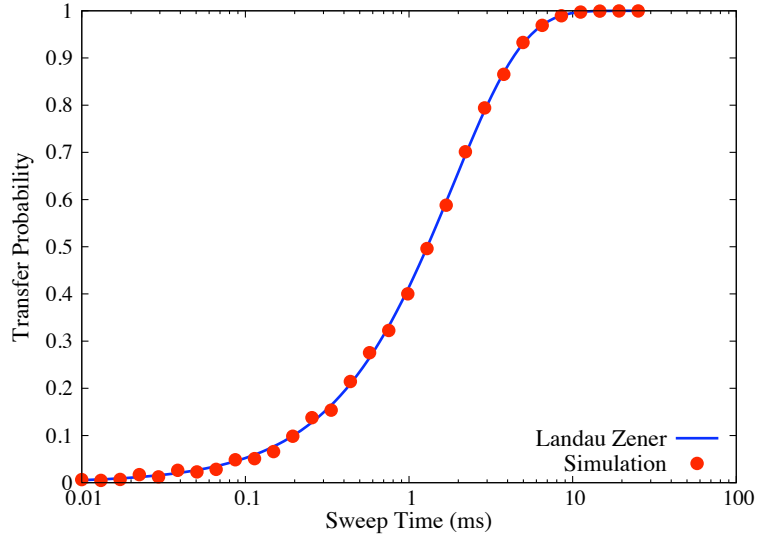


Figure 3.3: A simulation of adiabatic passage by integration of the optical Bloch equations [18] and equation 3.7. The curve is not a fit, but simply the equation 3.7 with parameters substituted, and $C = 1$. Notice the log scale and the region of near linearity. The Rabi frequency was 32 kHz and the sweep width was 3 MHz.

the other side, and the Rabi frequency remains constant throughout. In this model, the probability of state transfer is

$$P_{ad} = C \left(1 - \exp \left[-\frac{\pi \Omega^2}{2|\dot{\delta}|} \right] \right), \quad (3.7)$$

where δ is the sweep size, and $\dot{\delta}$ is the sweep rate, measured in Hz/s. The prefactor C does not appear normally in the Landau-Zener model, but is introduced here to represent the effect of noise processes, which reduce the maximal transfer efficiency. The most notable element of this expression is the strong dependence on Rabi frequency and sweep time. In fact, if plotted on a log scale, one expects a roughly linear growth of the transfer probability as sweep time increases. That is, the probability grows by a fixed amount every octave of sweep time. This observation is common even in places where the Landau-Zener approximation is not very good.

Other observed effects during the simulations was that if the sweep is small or long enough, oscillations can be seen in the graph of population transfer versus time. This

represents the fact that if the frequency scan spends too much time near resonance, then the procedure will achieve something more like Rabi oscillations than adiabatic passage. Those oscillations cause failure of the adiabatic passage to achieve 100% transfer, since the state is somewhat randomized by the oscillations. It was seen that the effect could be moderated by choosing a non-square temporal profile for the Rabi frequency, that is, turning on and off the laser smoothly rather than suddenly. If the profile was chosen to be Gaussian, for example, it was possible to make the sweep width very small, only a few times larger than the Rabi frequency. Halving the sweep size allows one to roughly halve the sweep time, since the relevant factor in equation 3.7 is $d\delta/dt$.

The dynamical picture of adiabatic passage can be represented on the Bloch sphere, as seen in figure 3.4. See [18, 45] for a discussion of how a laser's state is represented on the Bloch sphere. In this picture, a laser far red detuned of the atomic transition is pointed in the negative z direction, and a laser far blue detuned is pointed in the positive z direction. The atomic state precesses around the laser state vector, like a top precesses around the gravitational force vector. Thus, in an adiabatic sweep, the state vector begins either parallel or antiparallel to the atomic state vector, and then moves along the Bloch sphere until it points in the opposite direction. But if the sweep happens slowly enough, the atomic state precession will make small loops around the laser vector's instantaneous position, causing it to follow the laser state vector along its journey from one side of the Bloch sphere to the other. Notice that this works regardless of whether the initial atomic state is parallel or antiparallel to the initial laser state vector, since in the antiparallel case the atomic state will precess around the opposite of the laser state vector, and remain antiparallel to it throughout the laser vector's journey.

Of critical importance is the assumption throughout of coherence. Adiabatic passage is a deeply coherent effect, and the radiation source that drives it must remain phase coherent during the entire time its frequency is near the transition. This is easiest to understand by thinking about the Bloch sphere model. If the phase of the laser is allowed to slip during the transfer, then the laser state vector will shift azimuthally along the Bloch sphere quickly, and the atomic state vector will not be able to follow. In this case, the laser merely drives the transition incoherently for a short time, resulting in very poor population transfer. In

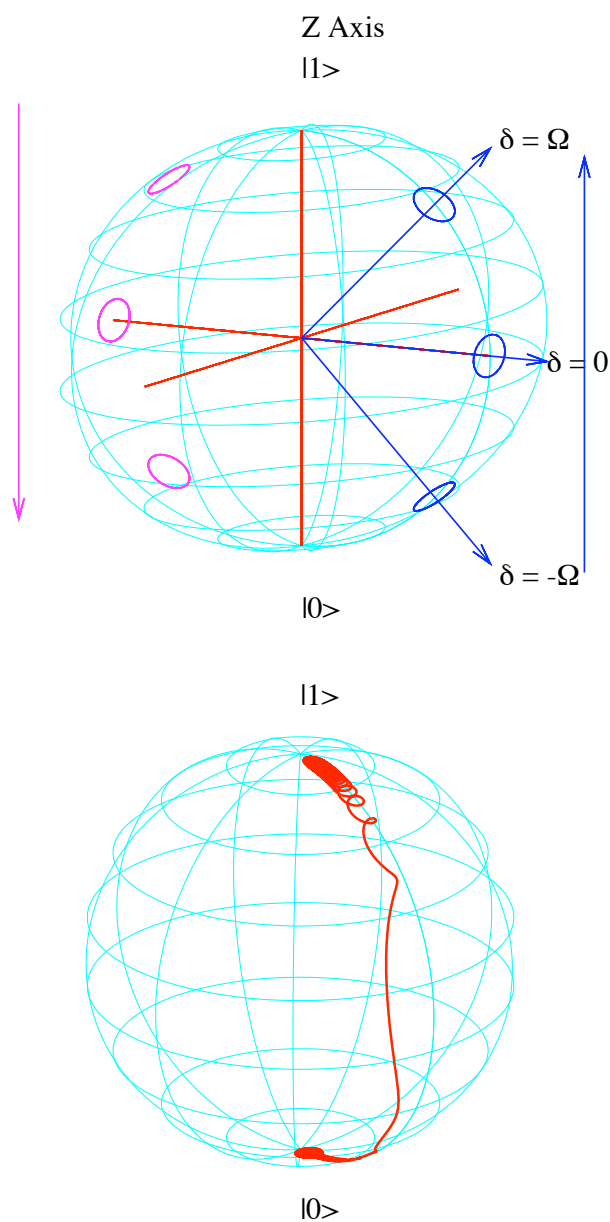


Figure 3.4: On the top is a schematic of adiabatic passage. The straight blue line represents the laser vector which starts with a large negative detuning and ends with a large positive one, while the little blue and magenta loops are the qubit state vector trajectory. The blue curves begin at the state $|0\rangle$ and end at $|1\rangle$, while the magenta goes the other way. On the bottom is a simulation of the full trajectory of adiabatic passage on the Bloch sphere. Rapid, tight rotations around the laser's state vector cause the atomic state to follow the laser's state vector as it moves from one side of the Bloch sphere to the other.

fact, in all previous demonstrations of adiabatic passage, sufficient coherence existed to also demonstrate at least several Rabi oscillations. This is usually facilitated by performing the transfer on a strong dipole transition, which is exactly contrary to the requirements of an optical qubit.

3.2 Quadrupole Transitions

The energy of interaction between a charge distribution and electric field is given by

$$H = d_i E_i + m_i B_i + \frac{1}{6} Q_{ij} \nabla_i E_j + \dots \quad (3.8)$$

$$= E1 + M1 + E2 + \dots \quad (3.9)$$

where the first term corresponds to the electric dipole interaction, the second to magnetic dipole and the last a quadrupole interaction. In atomic systems, a transition connecting states of similar parity must have zero electric dipole moment. Also, since \vec{d} and \vec{m} are both rank 1 tensors, they cannot connect states differing by more than $\Delta J = \pm 1, 0$. These types of observations lead to the well known *selection rules*. If two states are connected by $\Delta J = \pm 2$ and have the same parity, then the lowest order multipole moment for that transition is the electric quadrupole, also known as E2. For a plane wave

$$\vec{E} = \vec{E}_0 e^{i(k_i x_i - \omega t)}, \quad (3.10)$$

so for a quadrupole transition we can write

$$H = \frac{2\pi}{6\lambda} Q_{ij} k_i E_j. \quad (3.11)$$

This equation is represented in Cartesian tensors, whereas it is customary in spherically symmetric systems to work with spherical tensors. Fortunately, if a dot product is used to reduce Cartesian tensors to scalars, the dot product can simply be converted to spherical tensors [69, 70]. However, the usual normalization for the quadrupole moment in spherical

coordinates is not the same as the normalization for the spherical tensor, there is a conversion factor of $\sqrt{3/2}$ (it is $\sqrt{1/6}$ from the usual Cartesian definition), so

$$H = \frac{2\pi(-1)^m}{\sqrt{24\lambda}} Q_m^{(2)} E_{-m}^{(2)} \quad (3.12)$$

with $m = -2 \dots 2$ and $E^{(2)}$ is the second rank tensor formed from the laser's electric field strength $E^{(1)}$ and propagation direction $\hat{k}^{(1)}$, themselves represented as spherical tensors, and combined with Clebsch-Gordan coefficients, to wit

$$E_m^{(2)} = \langle 11ij|2m \rangle E_i^{(1)} \hat{k}_j^{(1)}. \quad (3.13)$$

In the rotating wave approximation, the Rabi frequency is simply the expectation value of the Hamiltonian between the two relevant states, divided by \hbar . When writing this expression, we would like to extract the electric field strength from $E^{(2)}$ and write it in terms of the laser intensity I and the dimensionless polarization/propagation tensor $\epsilon^{(2)}$. Since $I = E_0^2/(2Z_0)$ (Z_0 is the impedance of free space), we can write

$$\Omega = \frac{\pi(-1)^m}{\hbar\lambda} \sqrt{\frac{Z_0 I}{3}} \epsilon_{-m}^{(2)} \langle \alpha' F' J' L' m'_F | Q_m^{(2)} | \alpha F J L m_F \rangle. \quad (3.14)$$

Finally, if we apply the Wigner-Eckart theorem [44], we can write the Rabi frequency of a quadrupole transition in a useful form

$$\begin{aligned} \Omega &= \frac{\pi}{\hbar\lambda} \sqrt{\frac{Z_0 I}{3}} \epsilon_{-m}^{(2)} \sqrt{(2J+1)(2J'+1)(2F+1)(2F'+1)} \\ &\times \left\{ \begin{matrix} L' & J' & S \\ J & L & 2 \end{matrix} \right\} \left\{ \begin{matrix} J' & F' & I \\ F & J & 2 \end{matrix} \right\} \begin{pmatrix} F & 2 & F' \\ m_F & m & -m'_F \end{pmatrix} \\ &\times \langle \alpha' L' || Q || \alpha L \rangle. \end{aligned} \quad (3.15)$$

This result is consistent with [62]. I have neglected an overall phase.

A few observations about this expression. First, because of the 2 present in the 3-j symbol, the Rabi frequency is non-zero for any value of $m = -2 \dots 2$, provided that the polarization tensor ϵ does not prevent it. This corresponds to the fact that in quadrupole

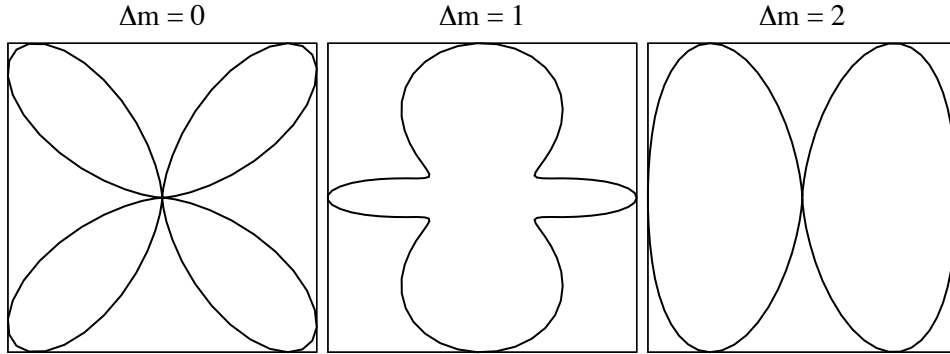


Figure 3.5: The various far-field radiation patterns from a quadrupole radiation source. The quantization axis is vertical in all three graphs.

transitions, $\Delta m = 2$ transitions are perfectly allowable, unlike in dipole transitions where $\Delta m = \pm 1, 0$ is an oft repeated mantra. Secondly, the Rabi frequency is inversely proportional to λ , unlike in dipole transitions where only the dipole strength is of any consequence. This is reasonable, since quadrupole interactions depend on the strength of the gradient of the electric field rather than the electric field strength itself. Thus, a long wavelength should interact only very weakly with any quadrupole transition. The dipole transition lifetime is proportional to $1/\lambda^3$, but this arises from the spectrum of electromagnetic vacuum fluctuations. The quadrupole lifetime is proportional to $1/\lambda^5$, since the gradient effect contributes an additional $1/\lambda^2$ in that case.

The properties of a quadrupole transition can also be determined from classical electrodynamics. From [31] the radiation pattern of a quadrupole source can be described by the vector field

$$\vec{X}_{lm} = \vec{L}Y_m^l(\theta, \phi) = \frac{1}{i\sqrt{l(l+1)}}(\vec{r} \times \vec{\nabla})Y_m^l(\theta, \phi) \quad (3.16)$$

from which the radiation intensity pattern and polarization can be determined, see figures 3.5 and 3.6. Of course, because of time reversal symmetry, these same radiation patterns are appropriate for excitation as well. One thing to note is that radiation incident on the ion

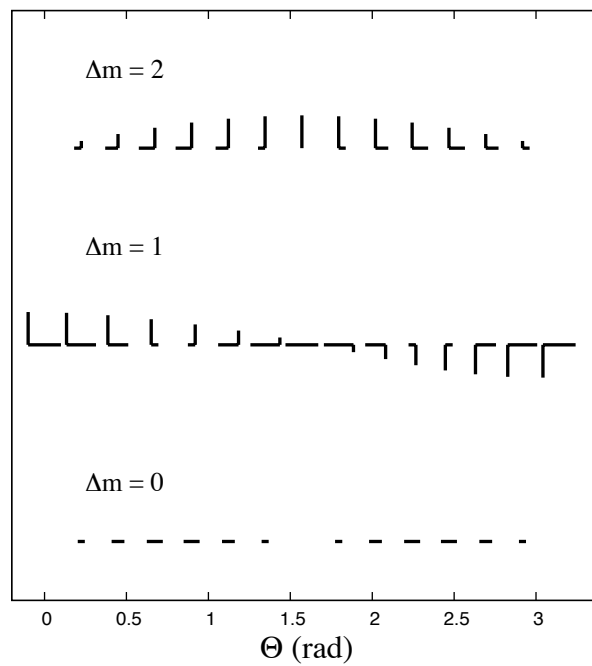


Figure 3.6: The polarization for each transition as a function of angle. Since the distributions are azimuthally symmetric, $\phi = 0$ is chosen. The quantization axis is horizontal. Two lines of equal length at a right angle indicates circular polarization, while unequal length indicates ellipticity. Care should be taken in evaluating the handedness of elliptical polarizations, since this chart is as viewed radially outward from the quadrupole source.

from along the axis of quantization can only excite $\Delta m = \pm 1$, thereby maximizing the effect of the laser. Ideally, as can be seen from the polarization plots, the laser would be circularly polarized to affect this. Linearly polarized light would excite both $\Delta m = \pm 1$, whereas circularly polarized light would excite only one of the two. Light exposed perpendicularly to the quantization axis can cause $\Delta m = \pm 1$ or $\Delta m = \pm 2$ depending on which linear polarization is used. The $\Delta m = 0$ transition requires exposure at an angle 45° with respect to the quantization axis. This transition would be desirable since $m_F = 0$ to $m_F = 0$ is the only magnetically insensitive transition. The analytic expressions for the polarization is given by

$$\vec{\epsilon}_{\Delta m=0} = \left(0, i\sqrt{\frac{15}{8\pi}} \cos(\theta) \sin(\theta) \right) \quad (3.17)$$

$$\vec{\epsilon}_{\Delta m=1} = \left(\sqrt{\frac{5}{16\pi}} e^{i\phi} \cos(\theta), i\sqrt{\frac{5}{16\pi}} e^{i\phi} \cos(2\theta) \right) \quad (3.18)$$

$$\vec{\epsilon}_{\Delta m=2} = \left(-\sqrt{\frac{5}{16\pi}} e^{i2\phi} \sin(\theta), -i\sqrt{\frac{5}{16\pi}} e^{i2\phi} \cos(\theta) \sin(\theta) \right) \quad (3.19)$$

And the power by $|\vec{\epsilon}|^2$.

In order to use equation 3.15, we have to obtain the quadrupole moment and determine the polarization tensor $\epsilon^{(2)}$. For the barium shelving transition at 1762 nm, we have from [22] the quadrupole moment to be $Q = -15.78ea_0^2$. However, as is sometimes customary among theory papers, this number is not the reduced matrix element itself, but rather the reduced matrix element combined with several of the geometric factors. In this thesis, the laser is linearly polarized along the axis of quantization, so that $\Delta m = \pm 1$ is excited, $\epsilon_1^{(2)} = -\epsilon_{-1}^{(2)} = 1/2$, and we can write

$$\begin{aligned} \Omega &= \frac{-15.78ea_0^2\pi}{2\hbar\lambda} \sqrt{\frac{Z_0 I}{3}} \sqrt{(2F+1)(2F'+1)} \\ &\quad \times \begin{Bmatrix} J' & F' & I \\ F & J & 2 \end{Bmatrix} \begin{pmatrix} F & 2 & F' \\ m_F & m & -m'_F \end{pmatrix} \\ &= 670.7\sqrt{\bar{I}(2F+1)(2F'+1)} \begin{Bmatrix} J' & F' & I \\ F & J & 2 \end{Bmatrix} \end{aligned} \quad (3.20)$$

$$\times \begin{pmatrix} F & 2 & F' \\ m_F & m & -m'_F \end{pmatrix} (1/\text{s}).$$

\bar{I} is measured in W/m^2 , and the result is an angular frequency.

Part II

TRAPPING BARIUM IONS

Chapter 4

ATOMIC STRUCTURE OF BARIUM ION

Barium ion has a single valence electron, which simplifies its atomic structure enough to make laser cooling a manageable feat. Atomic species containing many valence electrons can have extremely complicated energy level structures, many of which the subject can spontaneously decay into. In molecules, the situation is further exasperated because of weak selection rules caused by the low symmetry of the system and the multitude of available ro-vibrational transitions. Since every long lived state of the ion must be actively repumped, such species can require a large number of lasers to cool. Despite this, laser cooling and trapping have been demonstrated for simple molecules [16] and neutral atoms and ions having two valence electrons [26, 51], including neutral barium [11].

The elements whose ion possesses a single valence electron are Yb^+ , and groups 2 and 12 on the periodic table. These elements can be divided into two groups, those with low lying long lived D states (Ca^+ , Sr^+ , Hg^+ , Yb^+ , and Ba^+) and those without. Yb^+ is a special case in that it also has low lying F states which are extremely long lived [50]. Since Ba^+ belongs to the former group, comparisons are best drawn between these ions.

The two basic atomic energy schemes can be seen in figure 4.1. Those elements without D states can be cooled with only a single laser, whereas in the elements with a D state the allowed dipole transition from $P_{1/2}$ to $D_{3/2}$ causes the ion to spontaneously decay into that long lived state. Thus, a second *repump* laser is required to cool it, a decided disadvantage of this category of ion.

The availability of these D states, however, leads to numerous interesting possibilities unavailable to those ions without it. The $D_{5/2}$ state is inaccessible by the cooling cycle, being connected to $P_{1/2}$ by an M2 transition, which makes it a *dark state*. This dark state can either be used as an optical qubit [27] or for qubit readout. Also, especially for $^{137}\text{Ba}^+$, the $D_{3/2}$ manifold contains an $F=0$ level suitable as an optical atomic clock transition [59]. The

Ion	Abundances		Lasers			Hyperfine		Shelved State	
	Even	Odd	Cooling	Repump	Splitting (GHz)	Spin λ	Shelving λ	Lifetime	
Ba ⁺	71.7%	11.2%	493 nm	650 nm	8.037	3/2	1762 nm	32 s	
Ca ⁺	96.9%	.135%	397 nm	866 nm	3.226	7/2	738 nm	1 s	
Sr ⁺	82.6%	7.0%	422 nm	1092 nm	5	9/2	674 nm	.39 s	
Yb ⁺	21.8%	14.3%	370 nm	935 and 638 nm	12.643	1/2	467 nm	5.4 yr	
Be ⁺	0%	100%	313 nm	-	1.25	3/2	-	-	
Mg ⁺	79.0%	10%	280 nm	-	1.8	5/2	-	-	
Hg ⁺	29.8%	16.9%	194 nm	-	40.5	1/2	-	-	
Cd ⁺	28.7%	12.8%	227 nm	-	14.5	1/2	-	-	
Zn ⁺	48.6%	4.1%	206 nm	-	7.2	5/2	-	-	

Table 4.1: A summary of various qubit candidates. The abundance for the even isotope given is that of the most abundant even isotope, which is especially significant for Yb⁺, Hg⁺, and Cd⁺ where there are several significant even isotopes. The odd isotope data is provided for the most likely qubit candidate, which was chosen to be ¹¹¹Cd⁺, ¹⁷¹Yb⁺, and ¹⁹⁹Hg⁺, for those particular species. The shelving λ is the wavelength needed to excite the ion from its ground state into the shelved D state.

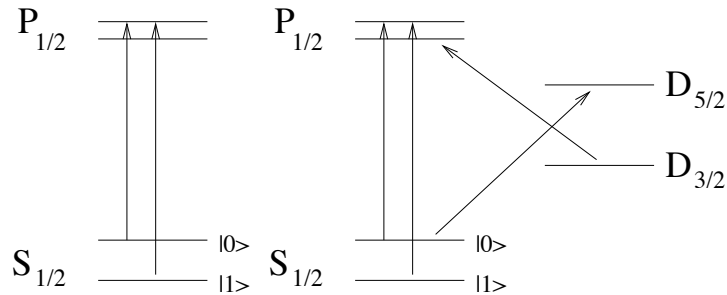


Figure 4.1: A crude diagram of the two basic level structures found in hyperfine ionic qubits. In the first without an available D state, the cooling cycle is closed with a single laser, and there is no shelving state. In the second with an available D state, a second repump laser is required to maintain a closed cooling cycle, but an additional shelving state is available.

so called *lambda structure* of the cooling cycle can also be leveraged in several techniques, including single photon generation [63]. Yb^+ is again a special case, since its D state is not useful as a shelving state, but the F state potentially is, since it has been successfully driven [55].

Barium has a number of advantages over the other D state ions. For one, it is the only such ion having all its cooling transitions in the visible part of the spectrum, as seen in table 4.1. This greatly simplifies laser alignment, and since none of its transitions are in the UV, it is possible to transmit all these frequencies through optical fibers with low loss, a feature barium shares with strontium and to a lesser extent calcium. Also, the abundance of its various isotopes is beneficial. The principal even isotope having no nuclear spin is quite abundant at 71.7% while the odd isotope used for hyperfine qubits is 11.23%, which allows either isotope to be trapped individually without isotope selective ionization. This contrasts with calcium, whose odd isotope is only .135%, so that it cannot be used at all as a hyperfine qubit without selective ionization, although the same fact makes it ideal as an optical qubit. Strontium is similarly favorable to barium, while mercury has its abundances almost evenly distributed among 6 different isotopes. Mercury requires a cryogenic vacuum system to trap, since its vapor pressure is too high at room temperature.

A major disadvantage of barium is its two infrared electric quadrupole transitions. The 1762 nm light is difficult to generate in quantity, and fluorescent film is only weakly sensitive

to that and the 2050 nm wavelengths. Electro-optic devices such as isolators and AOMs for these frequencies tend to be opaque to visible light, which further frustrates alignment. Most other species have their shelving transitions in the visible or near IR. This disadvantage is however closely related to a useful advantage, which is an extended dark state lifetime. Because spontaneous decay lifetimes for quadrupole transitions scale as λ^5 , the dark state lifetime is considerably longer in Ba^+ than in, for example, Ca^+ , with 32 seconds versus 1 second. Spontaneous decay remains a significant source of readout error [46], as well as placing a hard upper limit on the coherence time of optical qubits, although not limiting at this time [58].

The primary isotope of barium, $^{138}\text{Ba}^+$, has no nuclear spin and so no hyperfine structure. Although this greatly simplifies trapping, the isotope is useless as a hyperfine qubit. The next most abundant isotope, $^{137}\text{Ba}^+$, has hyperfine structure as shown in figure 4.2. For this isotope, $I=3/2$, giving a ground state splitting of 8.037 GHz. Because the ground state does not contain an $F=0$ level, the ion must be optically pumped by a polarization method, unlike some other species such as $^{111}\text{Cd}^+$ [6], $^{171}\text{Yb}^+$ [50], and $^{199}\text{Hg}^+$. These species can be optically pumped by simply disabling one of the cooling sidebands, forcing the ion into the singlet ground state. The radioactive isotope ^{133}Ba $I=1/2$, which is used in medical applications as barium sulfate, has a half-life of 10.53 years and does have a singlet hyperfine level, which would simplify optical pumping. The standard way of making ^{133}Ba is by the reaction $^{133}\text{Cs} + p \rightarrow n + ^{133}\text{Ba}$. That isotope has been isolated in a Paul trap before, and has a hyperfine splitting of 9.925 GHz [34].

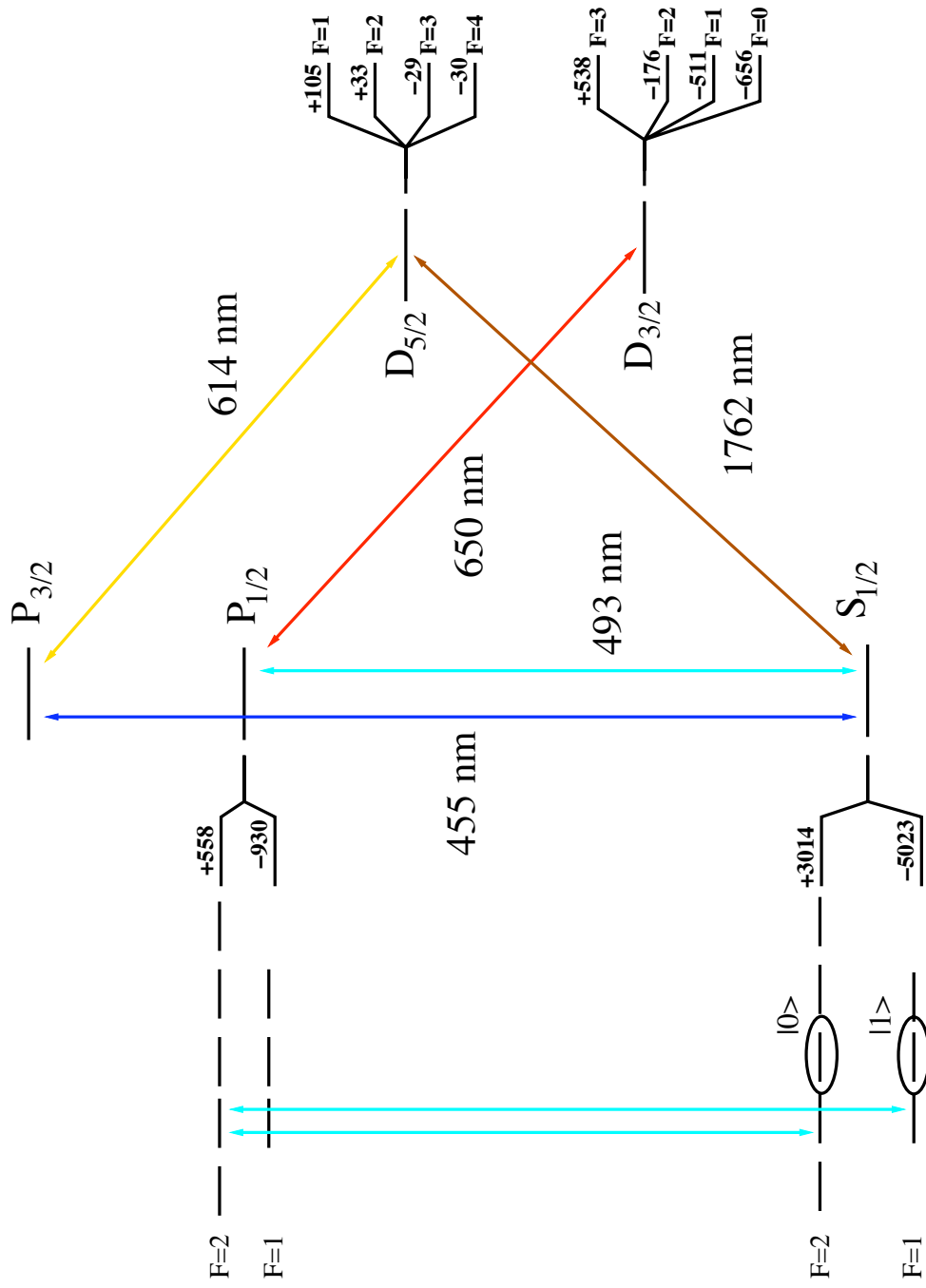


Figure 4.2: The level diagram of $^{137}\text{Ba}^+$. Hyperfine shifts are listed in MHz.

Chapter 5

APPARATUS

A successful Paul trap requires a configuration of trap electrodes that generates a quadrupole saddlepoint. Fortunately, it so happens that this is not as stringent a requirement as it might seem, as practically any symmetrical arrangement of RF and grounded DC electrodes will cause some quadrupole moment at its center, as long as the symmetry is not more than four fold. The history of Paul traps has been rather amusing in this regard. In the beginning, carefully machined pairs of hyperbolic electrodes were used to provide exact boundary conditions for a quadrupole potential at its center [48]. This configuration was expensive, difficult, and obstructed most of the optical access to the ion. Today, it is not uncommon to simply drill a hole in a plate, and not even necessarily provide DC electrodes [14, 32].

A substantial taxonomy of trap designs has developed from the great flexibility possible in configurations. The two major families are linear and non-linear traps. The non-linear designs are rather like the first Paul traps, a single azimuthally symmetric RF electrode with or without DC endcaps. In these cases, it is sufficient to treat an infinitely far away distance as ground, and a quadrupole moment strong enough for ion trapping will still exist. These trap configurations inherently have only a single point where the saddlepoint will accommodate an ion, which makes such a trap unsuitable for quantum computing. Linear traps are only actual Paul traps in 2 dimensions, the third dimension is secured by a pair of high voltage DC endcap electrodes. Note that in this type of trap the endcaps are not optional, since the ion will escape out the ends without them. An interesting subcategory of this latter type is a surface trap, where all trap electrodes are confined to a plane, and the quadrupole saddlepoint resides somewhat above the plane. Because such a setup can be easily generated by modern lithographic techniques, it is relatively simple to make microscopic versions, which is an interesting future direction of ion trap

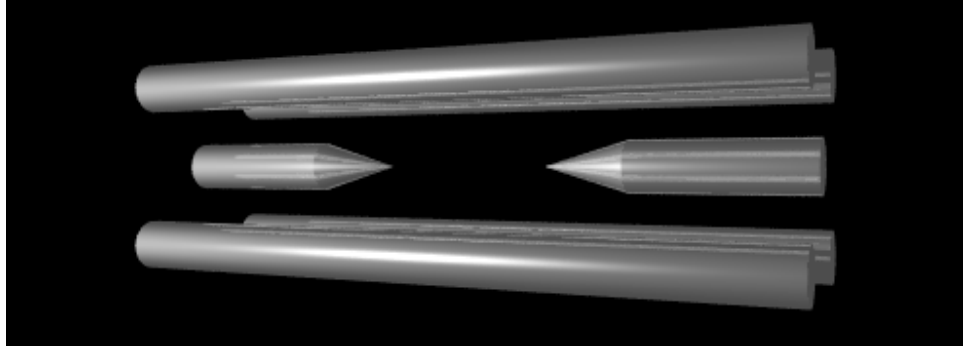


Figure 5.1: A 3D model of our trap design, not to scale.

quantum computing. Although a non-linear surface trap should be possible, because of its low applicability to quantum computing, it has not been pursued with much vigor.

Our trap is a macroscopic linear trap constructed with 4 tungsten “rods” stretched equidistant and parallel to one another, separated by .5 mm, see figure 5.1. Rods opposite to one another are electrically connected, and one such pair is grounded while the other is powered by high voltage RF, as in figure 5.2. The endcaps are two tungsten “needles” whose tips are separated by about 3.16 mm and charged with high voltage DC. In both cases, high voltage is of order 1 kV. Tungsten is used because its low ductility prevents the apparatus from shifting much during use. Also, tungsten is unusual in that it is a strong metal that can be electropolished in an easily obtained solution of potassium hydroxide. The apparatus is supported by two machined alumina holders held in place by a stainless steel support structure. The entire setup is in a UHV stainless steel vacuum chamber, pumped by a titanium sublimation pump and an ion pump to a pressure of about 10^{-11} Torr.

The RF high voltage is provided by delivering a 50Ω source impedance 1W source of 12.38 MHz RF to a helical resonator [41] with a quality factor of about 200. This resonantly impedance matches the source to the capacitive load of the trap, which is of order 10 pF dominated by the high vacuum feedthrough. Since $Q^2 = R_l/R_s - 1$ (ref [8]), and $P_l = V^2/R_l$ we have $V_l \approx Q\sqrt{PR_s} = QV_s \approx 1.4$ kV.

Eight fused silica viewports are available for optical access, six small ones around the

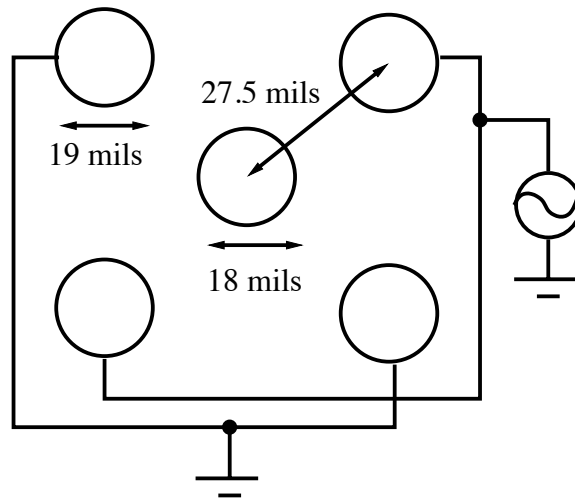


Figure 5.2: A cross section schematic of the trap design, including dimensions and electrical connections. Although not shown, the central pin is electrically connected to high voltage. One mil is one thousandth of an inch.

outer diameter of the trap chamber at a radial distance of 2.5 inches from the trap, while larger viewports sit above and below the trap at a distance of about 1 cm for imaging the ion. The imaging setup is as found in figure 5.3. It is a dual telescope arrangement with spatial filter pinhole at the focus of the first low magnification telescope and a 493 nm interference filter in the second, higher magnification stage. The first stage has a magnification of about 3.4 and the second about 220, so a total of about 750. The first lens is a NA .28 microscope objective, but since the ion does not sit at that optic's focal point, the total numerical aperture of the system is limited to about .23. The interference filter and spatial filter greatly reduce background noise from entering the CCD and PMT, although the interference filter is only 52% efficient transmitting 493 nm light. The interference filter has a useful additional feature in identifying the presence of an ion. Since only 493 nm cooling light can pass the interference filter, disabling the 650 nm laser should have no effect on the background counts observed by the PMT. However, if the 493 nm light detected is from a barium ion, then disabling the 650 nm laser will cause the ion to go dark and the PMT counts will dramatically decrease. This is powerful evidence for the presence of trapped barium ions.

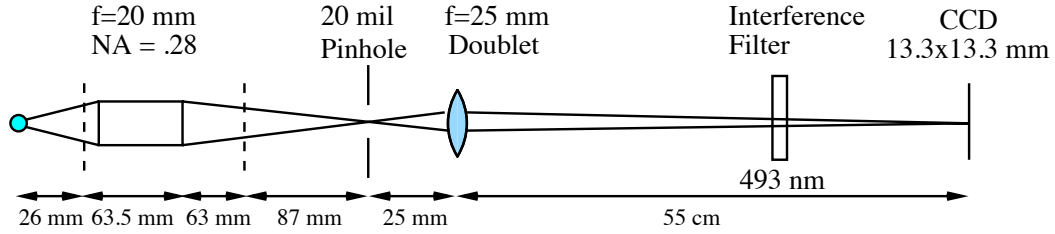


Figure 5.3: A ray diagram of the optical setup. The dashed lines represent the working planes of the microscope objective, which is a Mitutoyo 378-803-2 objective. The first magnification stage is from the ion to its image in the pinhole, and the second magnification stage is from the pinhole to the CCD camera.

The image can be viewed on either the Andor iXonTM CCD camera or on a PMT from HamamatsuTM. The latter is used during experiments due to its high quantum efficiency and speed, while the former is used for diagnostic purposes. In particular, it is easier to identify the number of ions and conditions such as whether the ion is cooled well using the camera.

Lasers and other radiation sources enter the system by way of 1 cm diameter anti-reflection coated viewports along the chamber's outer diameter. The two collimated cooling lasers enter along one diagonal while the 791 nm ionization laser and 1762 nm shelving laser enter through the opposite window. The N₂ ionization laser and optical pumping beam enter through the other two diagonal viewports, while the qubit rotation microwaves enter from one of the viewports normal to the trap, and the viewport opposite that one is left unused. The bottom viewport has been used in the past for a 614 nm deshelving LED (see section 10.3 and figure 5.4).

Laser light is provided by two ECDL's, one at 986 nm and the other at 650 nm. The 986 nm laser is frequency doubled with a potassium niobate crystal in a bow tie cavity to the required 493 nm. Both setups are commercial laser systems, the former is a TopticaTM TA-SHG-110 laser system, while the latter is a TopticaTM DL100.

The cooling lasers are processed by first modulating them (chapter 7) to obtain the necessary sidebands for cooling ¹³⁷Ba⁺. Then an AOM is introduced to allow for rapid switching of the lasers on and off. AOM's are superior to mechanical switches for this

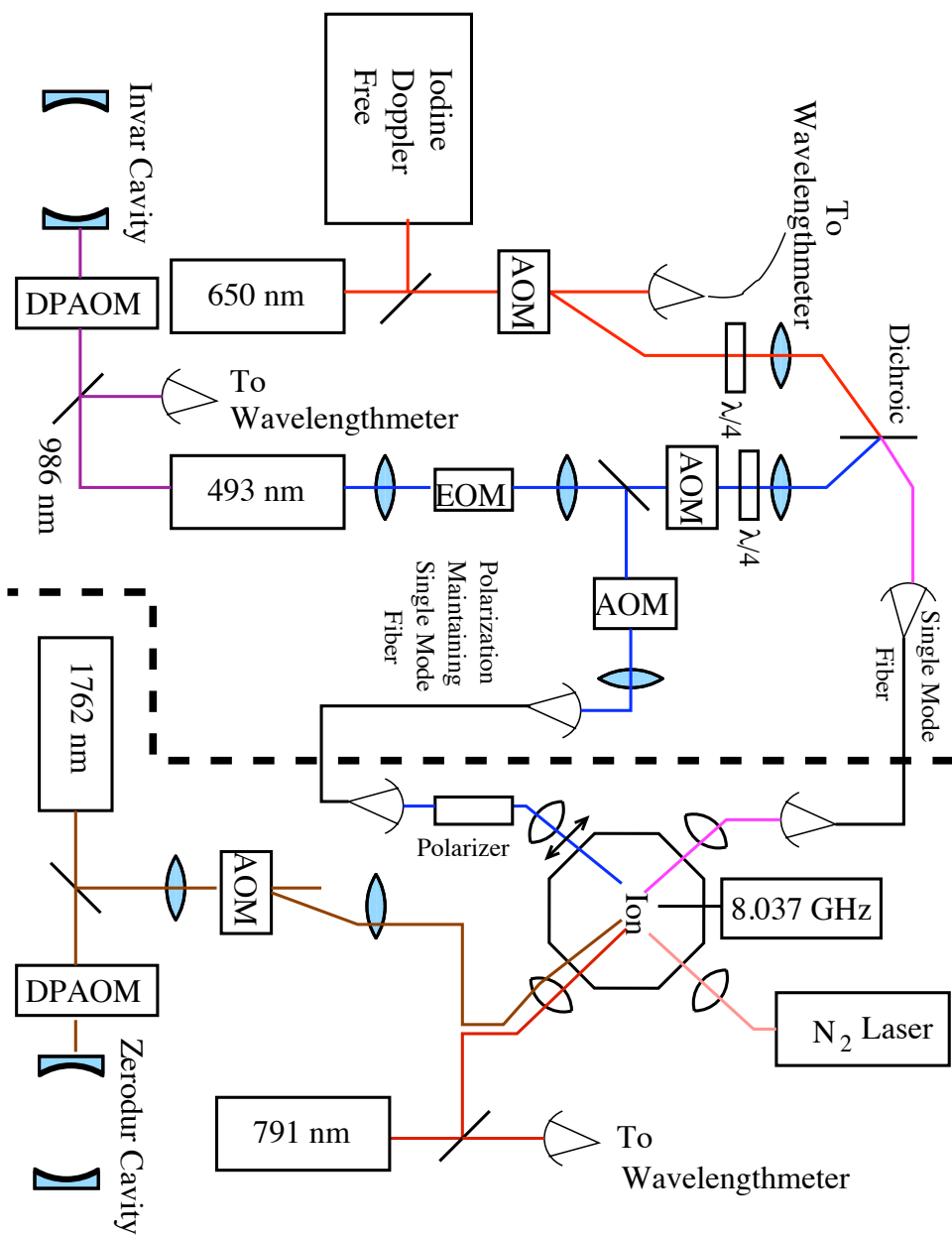


Figure 5.4: A block diagram of the laser setup.

purpose both because they are faster and because they do not cause mechanical vibration on the optical table, which causes lasers and doubling cavities to unlock, among other problems. Before the AOM the optical pumping beam is split off from the main cooling 493 nm beam and sent through its own switching AOM. Then the cooling lasers are combined onto a dichroic mirror, which reflects 493 nm light and transmits 650 nm light. Then these lasers are together coupled into a single mode optical fiber and piped to the trap setup. This is useful because it ensures perfect overlap between the cooling lasers. Also, optical components preceding the fiber coupler can be adjusted without misaligning the cooling laser to the trap. Finally, this has made it possible for us to operate two traps in separate rooms from the same set of cooling lasers, since the fiber coupling makes it possible to send light from one room to the other.

Central electronic control of the entire setup belongs to a PC having two National InstrumentsTM cards, a PCI-6220 and a PCIe-6351. Labview programs are created to orchestrate complicated experimental sequences. They are primarily used to turn on and off various lasers and light sources at appropriate times through RF switches and TTL outputs. The ability of these DAQ boards to act with hardware speed latencies is critical in a number of our experiments, especially those requiring pulses of a fixed duration or that need to be triggered on some other event, such as the phase of the wall voltage. The PMT output is read in by the DAQ's onboard counter.

Chapter 6

LOADING AND IONIZATION

Barium, like most of the alkali earths, has an extremely low vapor pressure at room temperature. As a result, it is necessary to heat these species to a considerable temperature in order to make an atomic beam suitable for loading into the Paul trap. Our oven is a simple hollow alumina cylinder wrapped in a tungsten filament coil containing a chip of barium metal. An aperture on the oven is necessary to direct and limit expansion of the atomic beam. This is because barium is a metal, and when coated on a surface, for example a vacuum viewport, is completely opaque and not even an especially good reflector. Also, careful consideration of the beam divergence should be made if state selective photoionization is to be used.

The high temperature involved in this process is somewhat problematic, since the radiated heat causes the Paul trap structure to warp and bend somewhat. This can cause the place that the ion rests to shift by as much as a hundred microns between turning on and off the oven. As long as the shift is smaller than the laser beam waist, this is of little concern. But it is possible for the ion to move further than this, which means that no cooling occurs as long as the oven is on, making single ion trapping impossible. It is desirable to create oven designs which shield the Paul trap from heat, or are more efficient, causing less radiated heat in the first place.

6.1 Ionization

A number of methods have been successfully used to ionize barium here. The simplest method involves an electron gun, where a tungsten filament is heated to almost 3000 K (yellow hot) and biased by a high voltage stainless steel pinhole which lies between it and the trap. Electrons shed by the filament due to thermionic emission are accelerated by the high potential on the pinhole. Those electrons that are not absorbed by the biasing plate

are launched towards the trap with a high velocity. Those electrons scattering off neutral barium atoms have some chance to free a bound electron, thereby creating Ba^+ . Those events happening within the trapping region can be laser cooled, and if laser cooling is sufficiently efficient while ion creation is sufficiently inefficient, it is possible to capture a mono-ion oscillator through due diligence on the part of the operator.

Photoionization has become the preferred method in recent years, wherein a UV light source is used to ionize the atomic beam directly. Not only does this technique occupy fewer high vacuum electrical feedthroughs, but since it doesn't emit a large flux of electrons towards the trap, it is generally considered to cause less patch charging on nearby dielectric, which is detrimental to ion trapping. We have demonstrated barium photoionization using a xenon arc flash lamp as well as a deuterium lamp. Theoretically, a deuterium lamp should have its largest spectral density [57] very near the barium ionization threshold at 237 nm [24], while xenon has its spectrum spread very widely throughout the visible; indeed it has been suggested as a sunlight replacement. However, when compared in practice, the two methods were found to have similar ionization efficiencies, both adding cool ions to the trap at roughly similar rates. This is likely because of the difficulty we had in focusing our deuterium light source to a tight spot, because the image of an arc lamp light source is an extended thread of light.

It should be noted that the work function of barium is well below the ionization threshold of atomized barium, around 460 nm. Since the trap electrodes are all completely coated in barium metal, we expect that any UV light hitting the electrodes will result in photoelectrons, causing many of the same problems as with the electron gun. Deuterium lamps are capable of stripping photoelectrons off of stainless steel, and so the problem is potentially more serious in that case.

6.2 Isotope Selectivity

Our objective of demonstrating multi qubit gates requires that we be able to trap multiple qubits in a single trap. Although the abundance of $^{137}\text{Ba}^+$ is high enough to trap without isotope selectivity, the probability of trapping 2 ions of $^{137}\text{Ba}^+$ and no other ion is exceedingly small. Trapping two $^{137}\text{Ba}^+$ ions has only occurred once in my tenure, and it was only

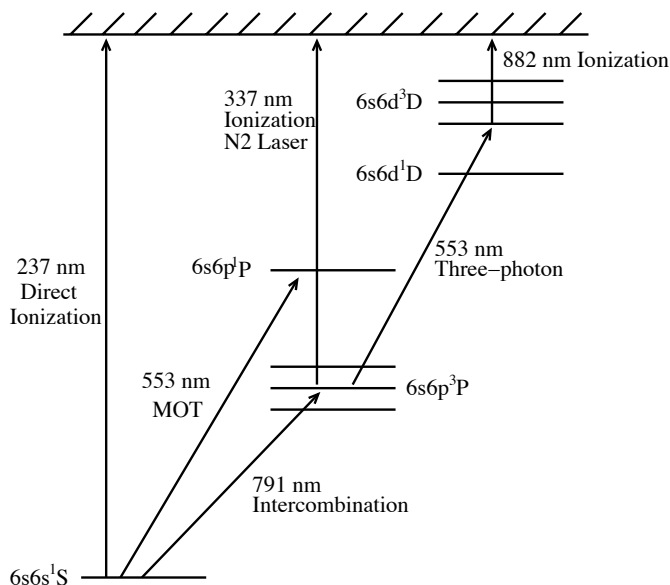


Figure 6.1: A few relevant levels in neutral barium. There are other irrelevant D and F levels not shown.

by remarkable luck that no third ion was also trapped. Thus, it is necessary to find some mechanism by which we can trap only the desired isotope and none other.

Previous experimenters [15] used an enriched source of barium so that only $^{137}\text{Ba}^+$ was emitted from their oven, eliminating all need for finesse in trapping technique. If in the future we wished to experiment with $^{133}\text{Ba}^+$, an enriched source will be necessary since that isotope does not occur naturally. Another technique where undesired isotopes of Mg^+ were ejected after being trapped has been explored with some success [28], but the strength and high trap depth of our linear trap design seems to make this impossible in our setup. Also, the trick is facilitated in Mg because the qubit isotope is the heaviest abundant isotope, where ^{137}Ba is neither the heaviest nor the lightest isotope.

We chose to implement isotope selective photoionization because of the high reported efficiency and versatility of the technique. Also, one setup can be shared among several traps, giving them all the appropriate selectivity. The technique, first demonstrated for barium in [66, 33], uses a two step ionization technique. First, a narrow band diode laser at 791 nm is used to excite neutral barium by an intercombination line (linewidth 50 kHz) to

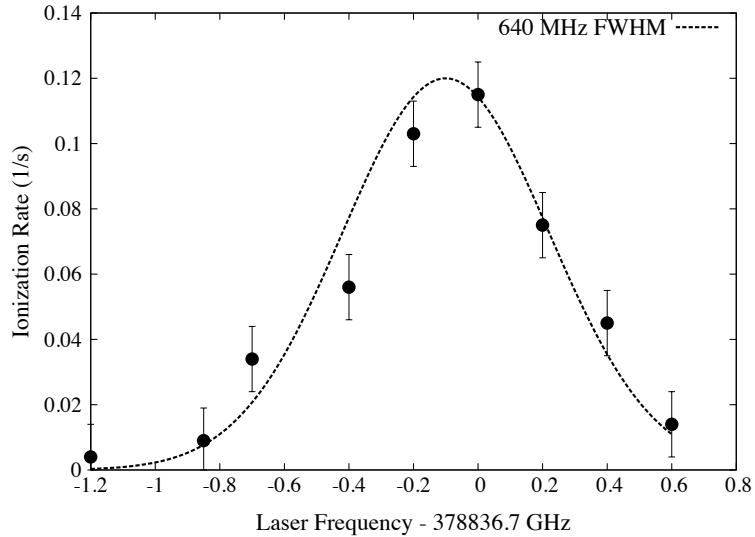


Figure 6.2: Measurements of the ionization and trapping rate as a function of 791 nm laser frequency for $^{138}\text{Ba}^+$. The ionization rate for $^{137}\text{Ba}^+$ is too low in our setup to measure accurately in this way, although one can see that the 1.8 GHz frequency separation is well resolved at this oven temperature. The FWHM of this line is about 640 MHz.

the $^3\text{P}_1$ state. Because of the substantial hyperfine splitting in barium, there is a 1.8 GHz difference between 137 and 138 [10], so that it is possible to only excite 137 and not 138 in this step. From here, a light source at 340 nm is sufficient to ionize only the chosen, excited atoms. Thus, only the desired isotope can be trapped. Note that with sufficient care, it should be possible to choose whatever isotope the experimenter wishes.

Two primary effects were found to limit this procedure in our setup. The first is Doppler broadening. As the oven temperature increases and the angle between the 791 nm laser and atomic beam decreases, the intercombination line is broadened significantly as seen in figure 6.3 [18], decreasing the possible isotope selectivity. Decreasing the oven temperature is undesirable since that exponentially decreases the availability of atoms and therefore greatly decreases trapping rates. For this reason, an angle as close as possible to 90 degrees is extremely important. In our present trap design, no consideration was given to this, and instead the oven sits at about a 50 degree incline with respect to the 791 nm laser. Although 137 selectivity has been observed in this setup, the ability to trap is extremely

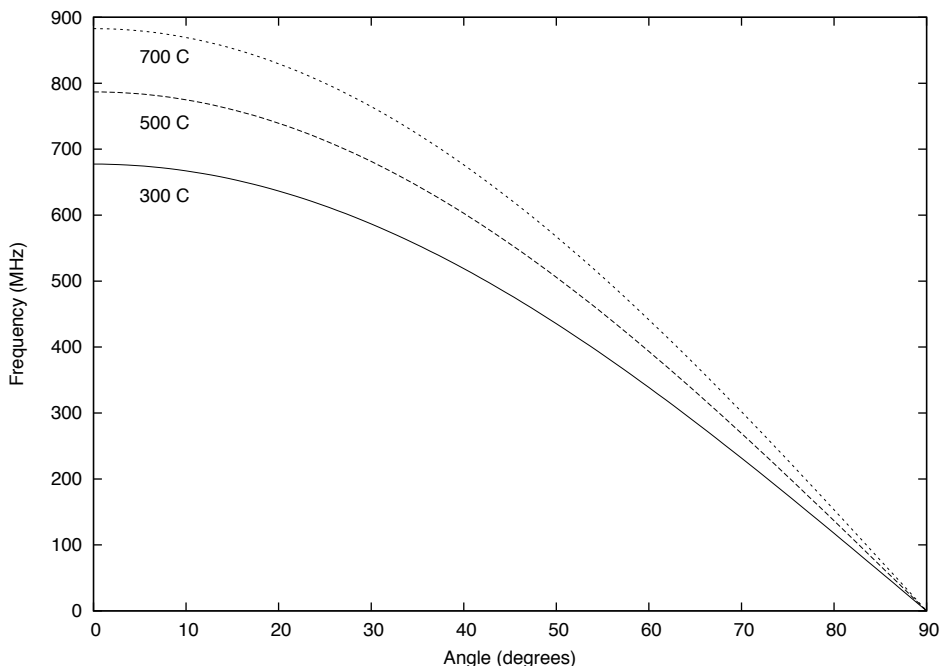


Figure 6.3: Doppler broadening of a neutral barium atomic beam as a function of angle and temperature.

sensitive on oven temperature, and it must be run at a very low temperature to be successful. Alternatively, because the ionization is so efficient, it is not necessary to run the ovens at a high current, eliminating the problems associated with a very high temperature. It should be noted that the experimenter's ability to eliminate Doppler broadening in an atomic beam is always limited by the collimation of the atomic beam and that of the excitation laser. That effect can only be eliminated by improved collimation or by Doppler free techniques discussed below.

The second major effect is the presence of photoelectrons caused by the ionization laser. We use a N_2 laser to obtain collimated 337 nm light for photoionization. However, being shorter than 460 nm, this laser is capable of making photoelectrons and generating ions in that way. This method was first demonstrated with the Xe lamp in our lab, and may in fact be the principal method of ionization with that light source. Here, collision with photoelectrons has proven to be nearly as efficient as photoionization in producing ions.

Indeed, a large number of barium ions can be trapped without the use of an oven by simply focusing the nitrogen laser onto any part of the trap electrodes. The dual ablation and photoelectron collision process is enormously effective in this case. However, since this ionization channel is not isotope selective, it must be carefully avoided. Hence the need for a well collimated and focused light source. We had a low level of success working with a UV LED, since this source was difficult to collimate and focus while avoiding the trap electrodes. Ionization was observed, but never isotope selectivity.

One might envision a two or three photon ionization scheme that avoids the use of any light source having wavelength less than 460 nm. Neutral barium does in fact have a set of F states in the narrow window that would allow a two photon method, but since the S to F transition is almost completely forbidden, that seems unlikely. One three photon scheme would be to use a 553 nm laser in addition to the 791 nm to excite to the $6s6d^3D$ state from the 3P_1 . Then ionization would occur at 884 nm, which either laser is capable of exciting. This has the downside of requiring the stabilization of a second laser to achieve ionization. However there is potential in that a 553 nm would be useful for a neutral barium MOT, since it is coincidentally the $^1P_1 \leftarrow ^1S_0$ wavelength as well [11]. Also, a three photon method could be done in a Doppler free way by counterpropagating the two laser beams, partially lifting the restrictions on careful oven alignment. This type of photoionization may be necessary in the future as traps become smaller and the poor mode structure of nitrogen lasers prove an impediment to effective focusing.

Chapter 7

LASER COOLING**7.1 Cooling Scheme**

In order to maintain a closed cooling cycle in $^{137}\text{Ba}^+$ it is necessary to apply sidebands to the cooling laser frequencies so that all hyperfine levels are affected by the cooling lasers. The cooling sideband transitions must be carefully selected. In particular, because of the extremely weak Clebsch-Gordan coefficients of the $\pi P_{1/2}(F=1) \leftrightarrow S_{1/2}(F=1)$ transition, see figure 8.1, it must be avoided in any feasible scenario. In fact, while experimenting with different configurations, it was found that placing the weak sideband on the F=1 to F=1 transition with the strong carrier on F=2 to F=2 resulted in an unobservably dark ion, and switching the sideband and carrier made the ion observable but extremely dim. In order to avoid this effect, previous researchers used an elaborate AOM switching scheme to reverse the circularly polarized cooling light every few nanoseconds, so as to avoid the weak π transitions [15]. It would be possible to drive F=1 to F=2 and F=2 to F=1 with 6.519 GHz modulation, but this would exclude the possibility of optically pumping with linearly polarized light. Therefore, we chose to drive from both ground state hyperfine levels to the $P_{1/2}$ F=2 level.

To accomplish this we can either use 4.018 GHz modulation and cool the ion using only sidebands, setting the carrier half way in between, or 8.037 GHz modulation and choose one transition to be cooled by the strong carrier. The latter choice was made in our case because it makes more power available for laser cooling and it forces all the laser frequencies away from any isotope besides ^{137}Ba , so that its essentially impossible to make a false identification of $^{137}\text{Ba}^+$. However, an important advantage of the 4.018 GHz scheme is that a very effective cooling laser shutter can be made by disabling the modulation RF. This would be a far more effective shutter than using an AOM alone, since the attenuation on RF switches is much greater than what can be achieved with an AOM optical switch.

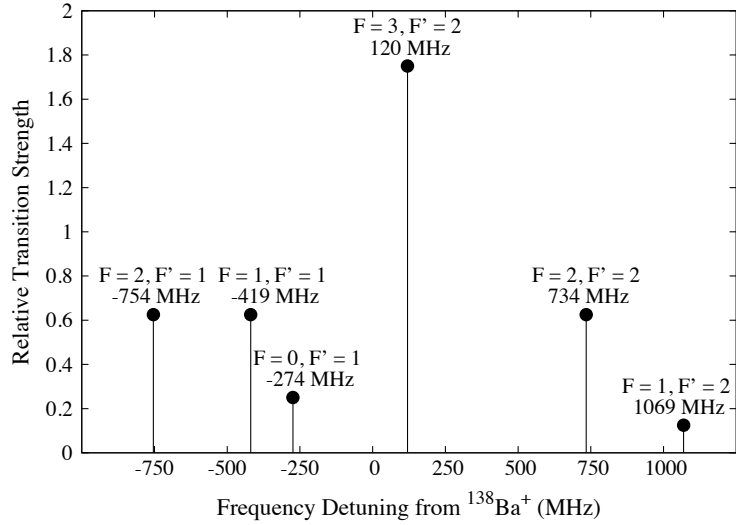


Figure 7.1: Theoretical strengths and frequencies of various 650 nm repump transitions in $^{137}\text{Ba}^+$. These strengths were obtained by averaging over all m levels and polarizations in both P and D states. For cooling $^{137}\text{Ba}^+$, the carrier is set to the 120 MHz transition and modulated at 614, 539, and 394 MHz.

The configuration with the carrier frequency on S F=1 to P F=2 was chosen because this was the only possibility near a Te_2 resonance.

The 650 nm sideband scheme is substantially more complicated but simultaneously more forgiving. Because the hyperfine structure of the $D_{3/2}$ state is so much smaller than in the S or P states, it is actually possible to cool $^{137}\text{Ba}^+$ without any red sidebands, relying entirely on power broadening to repump. However, the ion is considerably brighter with properly chosen sidebands. As seen in figure 7.1, all the $D_{3/2}$ states can be repumped effectively with only three modulation frequencies, 614, 539, and 394 MHz. These frequencies are low enough that the necessary sidebands can be generated by direct modulation of the red laser diode via a bias-T. One weakness of this strategy is that there is no place in the beam line with unmodulated 650 nm laser light, which would be helpful for laser locking.

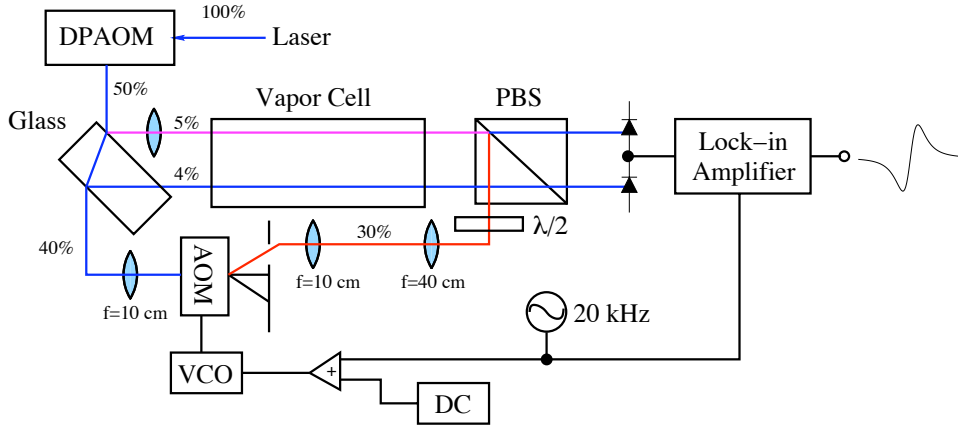


Figure 7.2: A diagram of a Doppler free saturated absorption spectroscopy setup. Approximate relative powers are listed in percentages to the side, and the pump beam is shown in red, while the place where pump and probe overlap are in purple.

7.2 Laser Stabilization

Several methods for frequency stabilizing the cooling lasers have been attempted in the history of our lab. In neutral atom trapping, the customary way to lock the cooling lasers involves simple Doppler free spectroscopy on a vapor of the very same species you intend to trap. However, since a vapor of barium would contain very little Ba^+ , a substitute must be found for ion trapping. An opto-galvanic cell can be used to find the Ba^+ transitions [60], and has been used with some success before in ion trapping, but to my knowledge cannot be done in a Doppler free manner.

A diagram of a Doppler free spectroscopy setup can be seen in figure 7.2, and described theoretically in [18]. Basically, the easiest way to measure the location of a molecular resonance is by simply passing light through vapor, and then detecting the fractional absorption of that light as a function of frequency. This approach is severely limited by the Gaussian distribution of atomic velocities whose independent Doppler shifts cause a broadening of the resonance. The strength of this effect is inversely proportional to the species' mass, but can easily be of order GHz. It is desirable to somehow select only the molecular population with some specific velocity, so that all the contributing molecules have the same Doppler shift and thus the apparent resonance will again be narrow. In Doppler free spectroscopy, two laser

beams are counterpropagated, and only those molecules which are resonant with both lasers cause signal. If the two laser beams have the same frequency, the only such molecule is one at rest, or that has its velocity perfectly perpendicular to the counterpropagating beams. In this way, Doppler effects are completely eliminated. This technique tends to be limited by pressure broadening, which arises from the decrease in excited state lifetime resulting from stimulated decay due to collisions, although the amount of pressure broadening varies considerably between species. Because of that, the lines tend to be substantially broader than the natural lifetime. If the beams are frequency shifted with respect to one another by an amount ν , then the only counted molecules will be those with the appropriate velocity to red shift one beam and blue shift the other beam by the same amount, so that they appear to be the same frequency to the molecule. Note that in this case the molecular resonance will appear shifted by an amount $\nu/2$ with respect to its natural wavelength as measured in its own rest frame. Finally, Doppler free resonances are not completely free from drift effects. The pressure shift is the effective renormalization to the atomic resonance due to the influence of nearby atoms, and so if the temperature is unstable, so can the atomic resonance be. Zeeman shifts are less prevalent, since Doppler free techniques are usually not sensitive enough to resolve individual Zeeman levels. Normally modulation is required to obtain an error signal, but there do exist methods that do not require modulation of the laser itself [74] or no modulation at all [52].

Since only a tiny fraction of the available molecules are engaged in Doppler free spectroscopy, the detected signal is extremely weak, and the technique is usually limited by signal to noise ratio. To detect the signal, modulation and lock in methods must be employed. Balanced photodetection is needed to cancel the effect of intensity fluctuations in the laser, since these can easily swamp the error signal. The strength of the signal nominally decreases with temperature, however, since elements that are solid at room temperature are used here, the signal is actually found to increase dramatically with temperature initially, and then decrease only at temperatures above the melting point. The cells are evacuated to limit pressure broadening and shifts while lowering the boiling/sublimation point.

In balanced photodetection, the laser beam is split equally into two beams, one of which is then made to carry a signal while the other idles. Then both beams are measured and

Frequency (MHz)	Description	Frequency (MHz)	Description
-690	Te ₂ Line	1766	Strong Te ₂
-550	Weak Te ₂	4301	Te ₂ Line
-440	Weak Te ₂	5780	¹³⁷ Ba ⁺ Cutoff
0	Reference Te ₂	5851	Te ₂ Line
16	¹³⁸ Ba ⁺ Cutoff	5891	Te ₂ Line

Table 7.1: A correlated list of Te₂ Doppler free and Ba⁺ resonances. The differences were measured using our commercial wavelengthmeter, and were all referenced to a line very near the ¹³⁸Ba⁺ cooling frequency. The line listed as a strong Te₂ resonance could be seen even with very low pump powers, a couple hundred μ W, and so would make a good reference point, except it is far from any of the relevant barium transitions. The weak ones could only be seen with great effort, and were extremely difficult to lock to. Although unmeasured, the point halfway between $P_{1/2}(F = 2) \leftrightarrow S_{1/2}(F = 2)$ and $P_{1/2}(F = 2) \leftrightarrow S_{1/2}(F = 1)$ is about 1762 MHz on this scale, which would be the frequency to lock the carrier to if a 4.018 GHz modulation scheme were used. This is very near the strong line.

the difference in power is used as the signal. This allows laser intensity fluctuation to be eliminated to first order, increasing SNR. This can be accomplished by simply putting the photodiodes in series and tapping your signal off from the center, as in figure 7.2; if the two photodiode currents are equal then all the current from one will pass through the other. Any imbalance in current must pass out through your tap and be detected. Since the efficiency of any two photodiodes will in general differ, it is necessary to attenuate one beam by a fixed percentage with a neutral density filter to make the time average of the two currents equal. A similar effect can be achieved with the clever use of a potentiometer acting as a voltage divider [30]. Also, a circuit has been developed that will automatically apply an electronic zero to the the difference in currents [29]. Finally, its important to note that since the output is a difference rather than a ratio, it only approximately cancels small fluctuations. Better in this regard would be to take the difference of two photodiodes connected to logarithmic detectors, although this approach tends to have low bandwidth and a high noise floor.

Te₂, as it so happens, is nearly a perfect frequency reference for the 493 nm cooling laser,

and has been used before [78]. A reference chart correlating the $^{138}\text{Ba}^+$ and $^{137}\text{Ba}^+$ transitions to tellurium can be found in table 7.1. This chart was obtained by comparing differences in frequency with the AngstromTM WS-7 wavelengthmeter. Since tellurium is a metal at room temperature, it has to be heated above 600°C to get a thick enough vapor for a good Doppler free signal. The greatest challenge involved with the oven design was to ensure that the coldest spot on the glass tellurium cell was not on the optical viewports, because in this case the tellurium would condense on the viewport and obstruct the probe beam. Normally, a so called “cold-finger” would be blown into the glass cell to make a space far from the heater bulk where a low temperature could be made to isolate the unvaporized tellurium. However, since the entire glass cell needed to be completely surrounded by an extremely hot oven, this didn’t prove very effective. Instead, several metal heat sinks were put in contact with the glass cell, with some measure of success. The high temperature increases the required intensity of the pump laser beam, so that the setup was always difficult to operate below about 3 mW of pump light. This proved a source of significant frustration, since the amount of available light was contingent on the ever shifting alignment of the 493 nm doubling cavity. Since any correction of the doubling cavity demanded readjustment to the entire beam line that followed, a great deal of time was spent maintaining this system from day to day. One untested possible solution is to instead lock the undoubled 986 nm laser light to some other atomic species. One possible candidate is water vapor, which is reported to have a transition at 303.718452 THz [56], about 2.3 GHz blue of the $^{137}\text{Ba}^+$ transition. Although some of this difference might be made up through pressure shifting [71, 53], it is possible that an electro-optic modulator would be required to bridge such a frequency difference.

It is possible to lock the 650 nm laser to a line in I_2 observed with Doppler free spectroscopy. Because of iodine’s hyperfine structure, there exists a whole sequence of lines over several hundred megahertz of relevant range which can be successfully locked to. I_2 is especially interesting because of the great wealth of spectroscopy done on it. In particular, the known P19 reference line exists a mere 4 GHz from the barium transition at 461.3076910 THz [77, 72], providing a convenient calibration standard. A less useful line occurs in Te_2 at 607.651176 THz [21], some 215 GHz away from barium. Iodine is much easier to manage

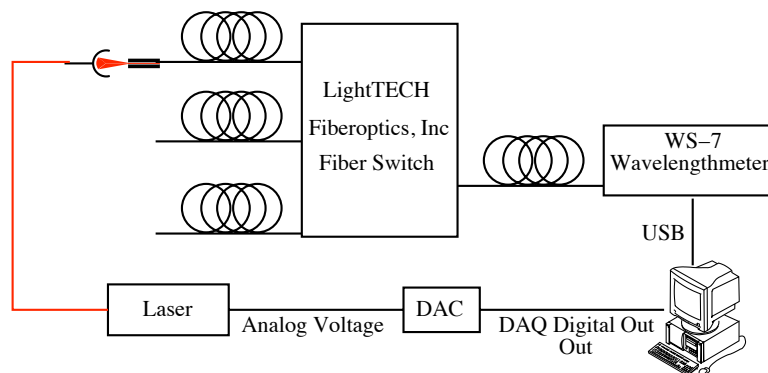


Figure 7.3: A block schematic of the wavelengthmeter based lock concept. Several lasers are coupled into a fiber switch (only one is shown here), which then selects one beam to be sent to the wavelengthmeter. The measured laser frequency is then stabilized in feedback by the computer, using an external DAC.

than Te_2 . Because iodine at a pressure of 1 mbar sublimates at a temperature slightly above room temperature, a much stronger signal that is more reliable from day to day (because of room temperature variations) can be obtained by heating it to about 31°C . At atmospheric pressures the sublimation temperature is 113.7°C . Although a similar condensation problem can occur with iodine, since the “oven” can be as simple as heater tape with aluminum foil, control of the heat distribution is much easier than in Te_2 .

Due to the chronic maintenance issues involved with the Te_2 setup, it was decided to move away from that to a wavelengthmeter based paradigm. In this setup, figure 7.3, a computer controlled fiber switch chooses which laser to send to the wavelengthmeter. The output of the wavelengthmeter is then read in by the computer, which by means of an external digital/analog converter returns a feedback signal to the laser being measured. By continually rotating between many inputs, a large number of lasers can be stabilized using the single wavelengthmeter; as many as five has been demonstrated to date. Having this mechanism available accelerates development time enormously, since there is no need to find and implement a new atomic frequency reference for each laser introduced to the lab.

It was known to us long before beginning this project that the wavelengthmeter frequency baseline can drift by 50-100 MHz in a day, well above the tolerance of effective laser cooling. There was also a suspicion that this drift was wavelength dependent, since the location of

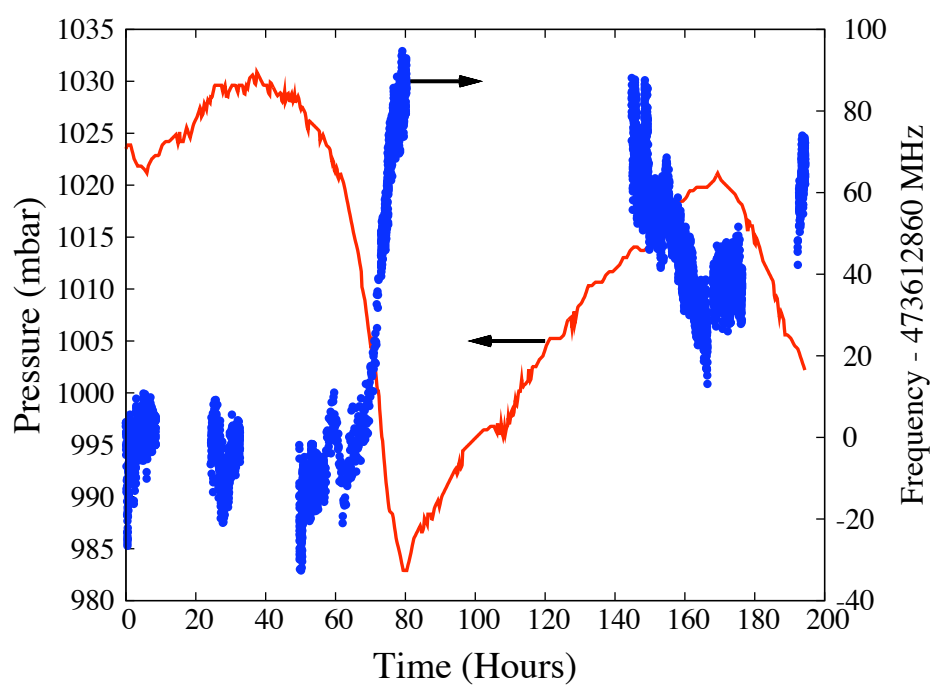


Figure 7.4: A comparison of the measured frequency of a HeNe laser and the atmospheric pressure. A strong anti-correlation can be seen here.

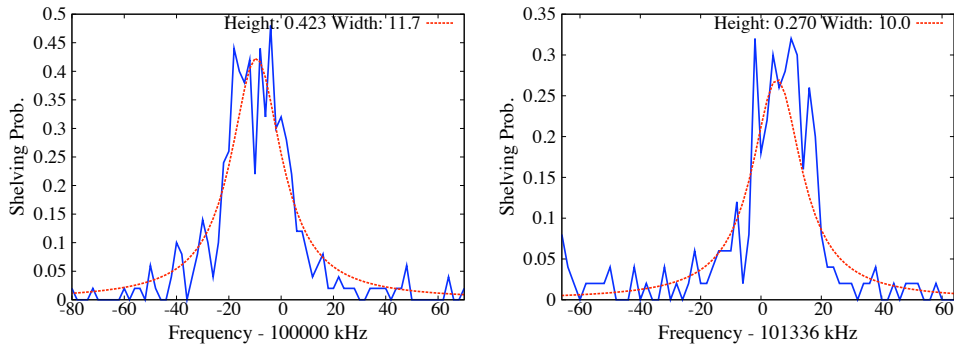


Figure 7.5: An attempt to use secular, axial sidebands to measure the absolute temperature of the ion. As can be seen, the red sideband (left) was found to be larger than the blue sideband (right), which does not correspond to any temperature. This apparent effect was probably due to the cooling efficiency changing substantially during the time between measuring the two sidebands.

Te_2 resonances was seen to drift by a different amount than I_2 . It was eventually found that most of this drift is correlated to atmospheric pressure, see figure 7.4. Because the wavelengthmeter standard is simply a calibrated and temperature controlled glass etalon, the most likely physical mechanism is that the increase in atmospheric pressure compresses the etalon, changing its spectroscopic properties, including thickness and index of refraction. Since the index of refraction for glass changes substantially over the relevant frequency range, it would not be surprising if this effect were wavelength dependent. To combat these effects, a frequency stabilized Helium Neon laser was purchased. The wavelengthmeter lock program internally calibrates itself against that reference, subtracting the apparent HeNe drift from all other frequency readings. This has improved the day to day reliability of ion trapping, since it accounts for most of the pressure shifts.

Despite this effort, the final result was less than satisfactory. The ion fluorescence was seen to change greatly over the course of several hour long experimental run, which is problematic for effective readout. More critically, during experimental runs with the 1762 nm, a dramatic dependence of shelving efficiency on laser cooling was seen, which from time to time resulted in impossible results such as measuring a stronger red motional sideband than blue, as in figure 7.5, which is not possible at any ion temperature. Also,

tests of adiabatic passage efficiency were seen to vary wildly between repeats with the same settings. This is in fact one of the major limiting factors in our ability to use the 1762 nm laser for detection, since almost no experiment can be done well with a time varying detection efficiency.

To address this issue we have recently constructed an invar spaced optical cavity to stabilize the 986 nm laser light. It has a finesse of about 200 and an FSR of 1.2 GHz. After shifting the 986 nm laser light we have a full milliwatt of laser power, we expect to obtain good SNR. The limiting factor will be the temperature coefficient of invar, which is about 1 ppm/K so that 10 mK corresponds to 3 MHz, which would be sufficient for laser cooling, though not necessarily without power broadening of the cooling transition. An error signal has been obtained by frequency modulating the AOM and mixing the transmission signal with the modulating signal using a lock-in amplifier. This has the added benefit of homodyning away laser amplitude noise. Hopefully, we will soon find our ion cooling to be far better behaved than in the past.

Part III

REALIZATION OF QUBIT OPERATIONS

Chapter 8

OPTICAL PUMPING

The first necessary task at hand is to prepare the qubit in a known level through some highly reliable process. Without high fidelity qubit preparation, all following steps in any quantum computation will be corrupted. Among the advantages of ionic quantum computing over competing qubit implementations is the long established technique of *optical pumping* [18], which can be used to drive an atomic system into a specified hyperfine level with better than 99% fidelity [40, 50]. Optical pumping can be performed in a small number of spontaneous decay cycles, putting the requisite preparation time to order 100 ns.

There are two primary methods of optical pumping used for hyperfine atomic qubits. In species possessing an $F=0$ level, it is sufficient to simply disable the laser frequency used to cool on that energy level. Since there is only one existent m level, the ion is guaranteed to eventually decay into $F=0$, $m_F=0$ of the ground state, and the qubit is effectively prepared. The second method, used here, leverages polarized light and selection rules to force a similar effect. The polarization method's fidelity is unfortunately limited by the experimenter's ability to align the ambient magnetic fields with the optical pumping beam, whereas the frequency method is much easier to implement. Also, the extinction ratio of the polarizer on the optical pumping beam is an additional systematic, whereas the frequency method extinction ratio can be much higher. Although $^{137}\text{Ba}^+$ cannot be prepared using the frequency method, $^{133}\text{Ba}^+$ can, see chapter 4.

In $^{137}\text{Ba}^+$, the qubit states are the $F=2$ and $F=1$, $m_F=0$ levels of the ground state. Our cooling laser is configured to drive both of these levels to $F=2$ manifold of the $P_{1/2}$ state. Now, it can be seen that in general $m_F = 0$ to $m_F = 0$ transitions are in fact forbidden in the dipole approximation when the F quantum number is the same for both states. This is a pure consequence of the system's symmetry, which is reflected in the Clebsch-Gordan coefficients, see figure. 8.1. As a result, if the ion is cooled with π polarized light, it will be driven out

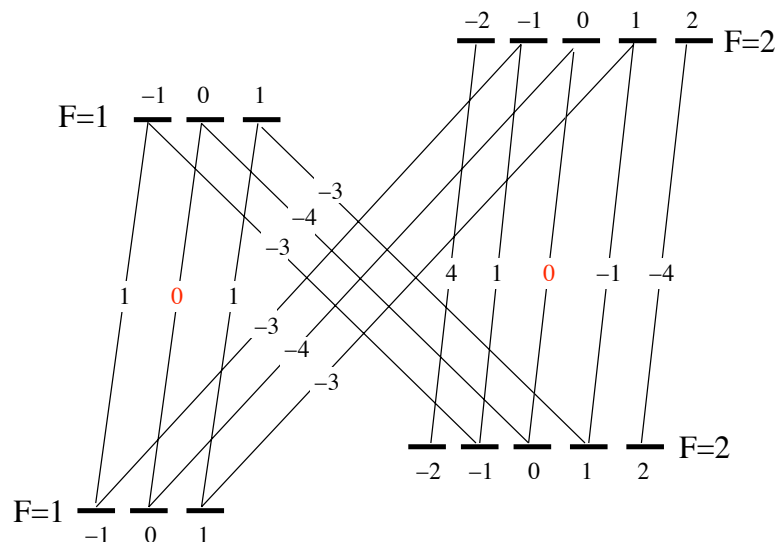


Figure 8.1: A representation of the phase and relative transition strengths due to geometric factors for all the π transitions in the $S_{1/2} \leftrightarrow P_{1/2}$ line of $^{137}\text{Ba}^+$. Note the two forbidden transitions. Although they are not shown here, the $F=1$ to $F=1$ σ transitions are similarly weak. From [45].

of every state and randomized by spontaneous decay until it reaches $(F=2)_{m_F=0}$. Since this process takes a short period of time, the ion will appear dark to the experimenter, who will know that it has been prepared in the upper qubit state. The reason for the $F=2$ state is because of the choice of sideband schemes on the cooling transitions, see chapter 7.

The exact pulse sequence to perform optical pumping is as follows. At first, both cooling lasers are active, and then, the 493 nm cooling laser is turned off, leaving the 650 nm for repumping. Next, the π polarized optical pumping beam is enabled for a fixed period of time. Then, before disabling the optical pumping beam the 493 nm sidebands are turned off. This is to ensure that even if the ion is not pumped into the $m=0$ state, it is at least pumped into the $F=2$ manifold. Moreover, if there remains any leakage cooling laser light, the possibility of that undoing the optical pumping is mitigated. Finally, the optical pumping beam is turned off and then the repump.

The cooling laser and optical pumping beam are set perpendicular to each other, and four coils are set up near the trap in order to control the magnetic field, see figure 8.3.

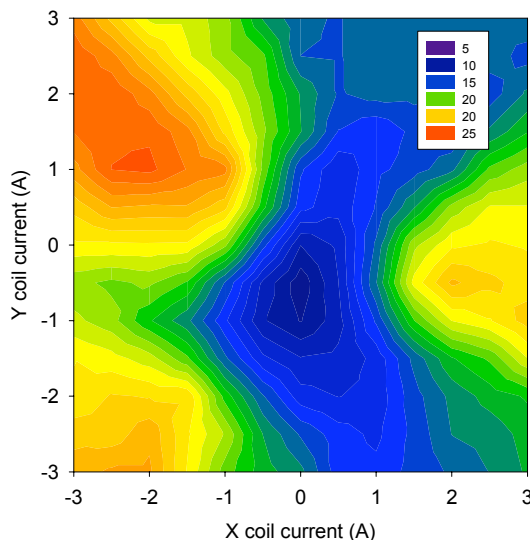


Figure 8.2: A contour graph of ion brightness caused by the optical pumping beam as a function of adjustment coil current. The dark spot near the center corresponds to the alignment where optical pumping is best. The scale is given as a percentage of observed fluorescence to total fluorescence with the non-optically pumping cooling laser enabled.

One pair of coils provides the bulk of the field, of order 7 gauss, to break the magnetic degeneracy and coarsely align the field along the cooling laser axis. It is important to break the degeneracy of the Zeeman levels, since otherwise some superposition of Zeeman levels will result in a dark state, that the ion will always eventually find. The strength of this field is generally fixed to control the size of Zeeman splittings, which affects cooling efficiency and adiabatic passage, see chapter 10. The other two coils are adjusted to precisely align the field to be perpendicular to the optical pumping beam. The polarization of the optical pumping beam is carefully prepared to be in the plane of the trap using a high extinction ratio Glan-Thompson polarizer. The cooling beam needs to be polarized such that it is not circular since this will cause optical pumping into the stretched $m_F = \pm 2$ state. Notice that this concern applies for both cooling and repump lasers.

If the alignment is far from accurate, then the optical pumping beam together with the red repumping beam will cause the ion to fluoresce. Once alignment is complete, the ion will appear dark, as mentioned before. Thus, by observing the fluorescence of the ion as

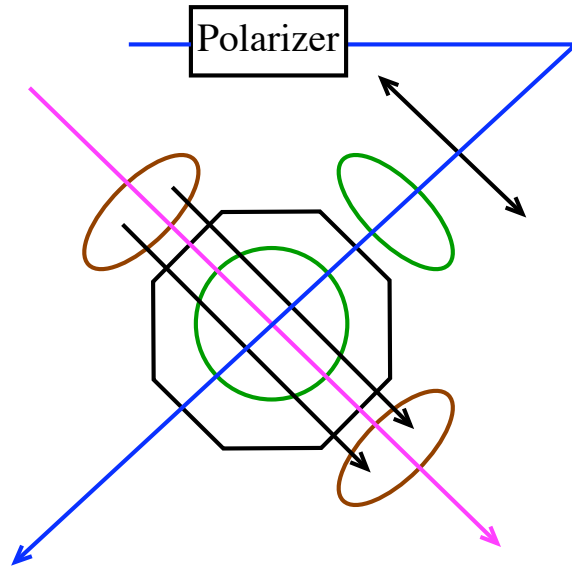


Figure 8.3: A diagram of the magnetic field configuration. The main coils are in brown, and carry about 3A of current. The alignment coils are in green and carry of order 100 mA. The main cooling lasers, both 493 nm and 650 nm are in magenta, and the optical pumping beam is blue.

the two alignment coils are adjusted, the appropriate settings can be discovered and optical pumping achieved. The results of such an experiment can be found in figure 8.2. Since this method relies on finding a configuration that minimizes PMT counts, it suffers from a number of systematics, such as PMT dark counts, laser scatter, room light background, and fluctuations in laser brightness. Also, ion fluorescence is a relatively weak function of misalignment angle [60], so that there can be a considerable uncertainty in the recorded contour's minimum. The optical pumping fidelity is similarly insensitive however, so that problem is not as great as it might seem. The systematics can be mitigated somewhat by careful subtraction of backgrounds from each data point, as well as normalization by laser intensity. However, the process remains a fairly tedious one.

The success of optical pumping is most easily observed by exciting transitions with the 1762 nm laser. By scanning the laser frequency and detecting the rate of shelving events as a function of frequency, it is possible to identify each of the ground state hyperfine levels. Their relative heights show the population of each level, since the exposure time

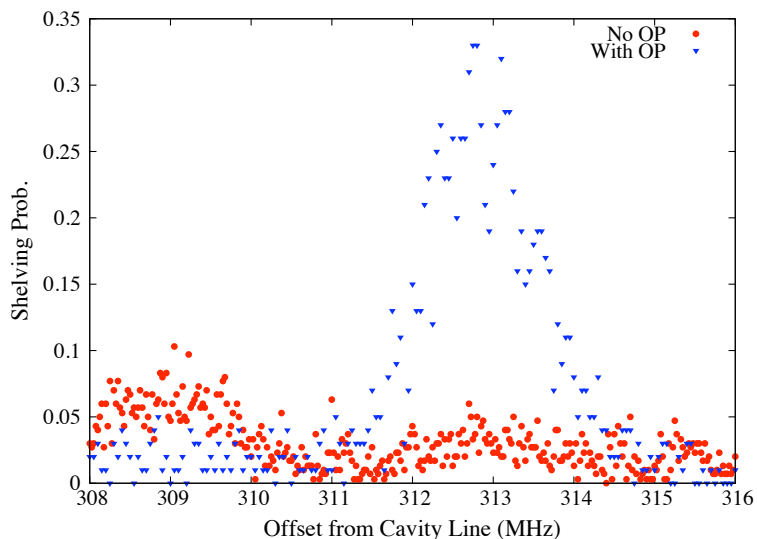


Figure 8.4: Demonstration of optical pumping into the $m_F = 0$ state. In one run (red points), no optical pumping is used, and one can see that several m_F levels have been occupied. In the next run (blue points), the entire experimental procedure remains unchanged except the optical pumping sequence is applied briefly before the 1762 nm laser. In this case the depletion of other states and the increase in $m_F = 0$ can be clearly seen.

at each step is equal. By choosing whether or not to utilize an optical pumping exposure, the experimenter can observe changes in the ground state population caused by optical pumping, as can be seen in figure 8.4. Because taking this sort of data is costly in terms of time, a single run may take half an hour or more, it does not provide a suitable feedback for aligning the magnetic field coils. However, it does provide excellent evidence that the optical pumping is in fact working. Also, proof positive for the effectiveness of optical pumping can be seen in the Rabi flop data, as in figure 9.1, since it would be impossible for this curve to reach 0% or indeed fall beneath the inverse of the number of ground state m levels, 12.5%, without optical pumping.

Chapter 9

QUBIT ROTATION

9.1 Hyperfine Qubits

The primary goal of this research is to demonstrate a hyperfine qubit in $^{137}\text{Ba}^+$. For a single qubit, this requires the ability to perform qubit rotations, a complete set of which would include σ_x and σ_z rotations. In the paradigm of hyperfine qubits driven by resonant microwaves, a σ_z rotation is caused by introducing a phase shift to the microwave clock, and so is primarily a technological requirement of the microwave source. To this end, we have been developing a “pulse programmer” which, by means of a DDS, is capable of generating 8 GHz signals with arbitrary amplitude envelope and phase control. In the mean time, it is satisfactory to demonstrate σ_x rotations in the form of Rabi flops. The ability to drive and observe Rabi oscillations exhibits all of the techniques developed in this work, including the ability to trap and cool $^{137}\text{Ba}^+$, optically pump, perform readout, and resonantly excite the hyperfine transition.

To perform a microwave Rabi flop experiment, we first apply the optical pumping pulse sequence (see chapter 8) to prepare the ion in the $F=2$ $m_F=0$ state. Next, with all lasers off, the ion is exposed to a pulse of microwave radiation for a period of time exactly specified by the computer’s National InstrumentsTM card. Next, with all other lasers still off, the 1762 nm adiabatic passage sequence is applied (see chapter 10). The cooling lasers are turned back on, the 493 nm sidebands are enabled, and the PMTs are counted for a set period of time to determine if the ion is bright or not. The result of that measurement is recorded, and if dark, a deshelling sequence is initiated. Then the whole sequence is repeated. This continues until a set number of sequences has occurred, which is chosen by the experimenter to provide adequate statistics. Then, the experimenter chooses a new exposure time for the microwaves and repeats the experiment in an effort to map out the qubit rotations.

The result of such an experiment can be found in figure 9.1. Several important facts

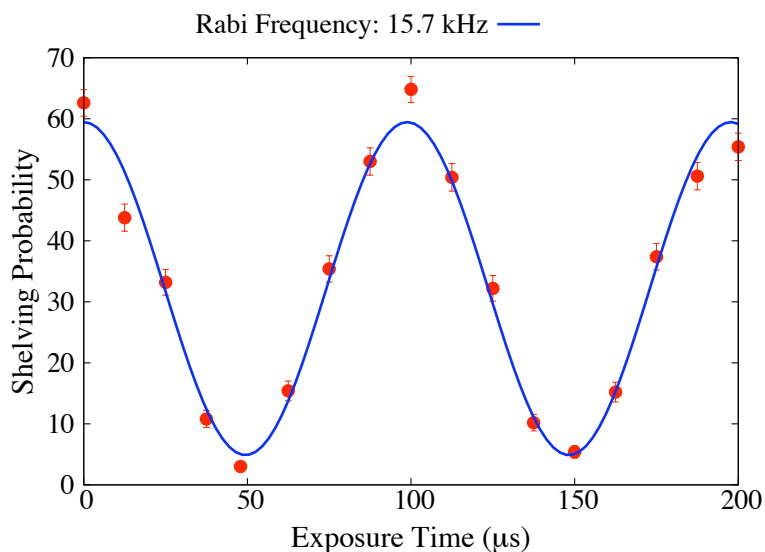


Figure 9.1: A demonstration of RF Rabi oscillations. The observed Rabi frequency is about 15 kHz, and the contrast is about 54%. If optical pumping did not succeed, the lower bound could not fall below 12.5%, since this would be the occupation of any given m_F level without optical pumping.

can be deciphered from this data. First, the Rabi frequency is about 15 kHz, which is largely a consequence of the great distance from the RF source to the ion, about 5 cm. The RF source could not be placed closer, because the trap support structure obstructed the radiation. Also, the curve drops nearly to zero, which could only happen if optical pumping were effective. Finally, the highest limit of the curve is about 60%, which is limited by the effectiveness of the adiabatic passage. The adiabatic passage appears to be limited by both the coherence of the laser and the poor, inconsistent cooling due to the lasers. Considerable effort has been applied to improve this contrast, but with limited success. Because of the weakness of the quadrupole transition, the coherence requirement of the shelving transition is extremely strong. Even though the laser linewidth has been reduced to below 10 kHz (see chapter 11), the shelving efficiency has not yet improved substantially.

9.2 Optical Qubits

Whereas in a hyperfine qubit the quantum information is stored in two levels separated by a microwave transition, it is also possible to store information in two atomic levels separated by an *optical* transition. In our case, the two relevant levels would be the $S_{1/2}$ ground state and the $D_{5/2}$ shelved state. This technique has the significant advantage of not requiring a separate shelving step in the readout procedure - the ion is already shelved when in the excited state, and so readout is accomplished simply by activating the cooling lasers. It has the significant disadvantage of requiring an extremely stable laser to coherently excite the transition.

Because of the rapid spontaneous decay rate of dipole transitions and resulting low coherence time, optical qubits are chosen to be connected by a quadrupole transition. This however results in the transition being extremely narrow spectrally, and very large amounts of power are necessary to drive it with any speed. Thus, a high power, long coherence time laser is necessary to implement such a qubit. The appropriate criterion is that the driven Rabi frequency must be much greater than the laser line width to affect useful quantum gates.

Because an optical qubit doesn't require the atom to have hyperfine structure, one could in principle implement such a qubit in $^{138}\text{Ba}^+$. However, the absence of a magnetically insensitive transition causes electronic interference to be a major limiting factor. Such experiments should be done phase locked to the wall circuit's 60 Hz AC power, such that every experiment is initiated when the magnetic field induced by the wall circuit is at some fixed value. This limits experiments to be performed at 60 Hz (or potentially 120 Hz), a highly undesirable feature. In $^{137}\text{Ba}^+$ magnetically insensitive transitions do exist, and would partially lift this restriction. Such a transition is not used here however due in part to the difficulty in driving such a transition, see section 3.2.

Considering the demonstrated stability of our infrared laser, several efforts have been made to demonstrate an optical qubit, usually in $^{138}\text{Ba}^+$, although also in $^{137}\text{Ba}^+$. Figure 9.2 contains the results of one such attempt. The beginnings of a single Rabi flop can be seen, demonstrating that the laser's linewidth is slightly less than the Rabi frequency, the

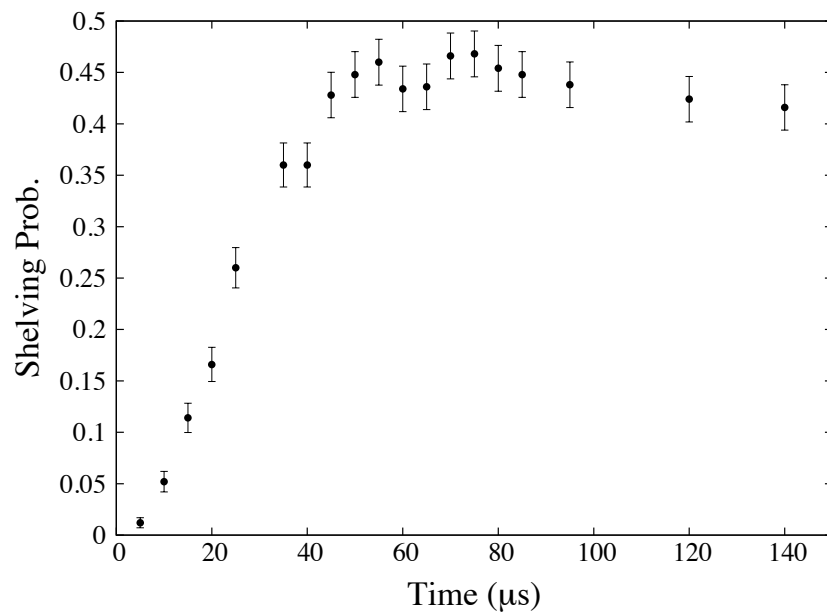


Figure 9.2: An attempt at an optical Rabi flop. Notice the resolved “wiggles” suggesting the beginning of coherence.

latter of which is roughly 5 kHz. This corresponds well with the results from linewidth measurements, which show that the transition is indeed power broadened, although the effect of laser incoherence is observable, see chapter 11.

Chapter 10

READOUT**10.1 Basics**

Readout is another major advantage of ionic qubits, because of the high signal to noise and contrast ratio that can be achieved using the electron shelving technique [47]. To use this technique, the ion is selectively excited into the dark $D_{5/2}$ state at the end of some computing sequence, and then the cooling lasers are activated. If the ion is found to be dark, then it was in the 0 qubit level, and if bright then it was in the 1 qubit level. Because the difference in scattered light is dramatically different between a fluorescing and non-fluorescing ion, this provides a very strong signal for state discrimination.

Fundamental limitations to the speed of this technique should be considered. First, since only spontaneously emitted light is detected, the number of utilizable photons can be no more than the natural linewidth of the cooling transition. For Ba^+ this is about 95 million photons per second. Also, it is difficult to collect and detect more than a percent of all available photons. These considerations together tend to limit the number of collected photons to about 200 thousand per second. Both of these limitations can be overcome if cavity QED methods are employed [12]. Also, work has been done in our lab to use high numerical aperture mirrors to increase the overall collection efficiency by an order of magnitude [63]. In either case considerable technical challenges exist. In systems with lambda configuration cooling cycles such as barium it is difficult to approach even this rate because of interaction between the two lasers. The presence of hyperfine structure also tends to exasperate the situation, since the splitting tends to mimic the effect of excess micromotion in terms of cooling. In the trap used here, it is rare to observe more than 20 thousand counts per second.

Assuming Poissonian statistics, it is necessary to wait 6.64 times the average delay between photons to ensure a 99% probability of correctly identifying the ion state, see

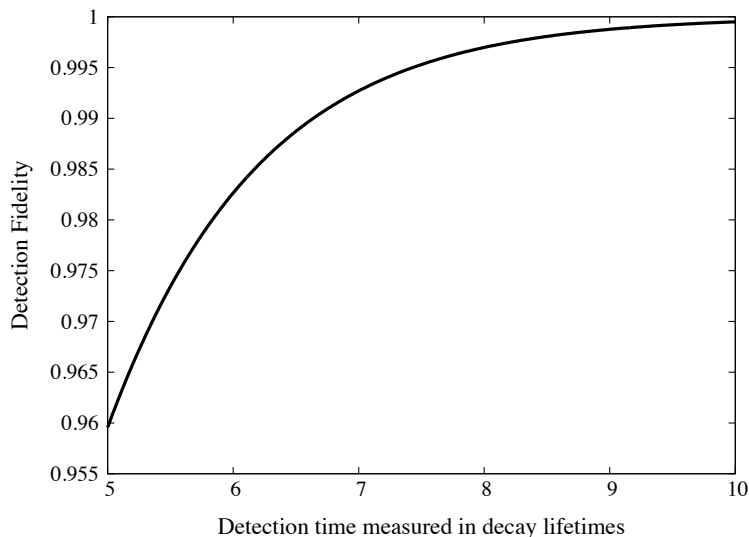


Figure 10.1: The confidence level one has that a spontaneous decay has occurred as a function of wait time, according to Poissonian statistics.

figure 10.1. So with the quoted photon rate of 20000, 99% fidelity requires a wait time of 332 μs . This wait time can on average be decreased by short circuiting the detection period after the arrival of a single photon, or more generally after a sufficiently convincing number of photons. Such a scheme has been explored in ref [46]. Note however that any such method can only decrease the time of detecting a bright ion, a dark ion detection must wait the full statistically required time. It is in general more difficult to detect a dark state than a bright state.

Additionally, one must consider the loss in fidelity due to noise. The dark counts of a PMT is an unavoidable noise source, while background laser scatter is a large though reducible problem. Dark counts for high performance PMTs can be as much as 300 counts/second, though potentially as low as 25, while background light can contribute easily as much. In the previous analysis, a single detected photon was considered sufficient to conclude the ion is bright, meaning that each dark count can potentially result in a false positive. Thus, with the previously stated wait time of 332 μs , and say a total background of 200 counts per second, the infidelity can be as high as 6.6% from noise alone.

Consider a histogram of photon counts in some fixed time frame, such as that found in

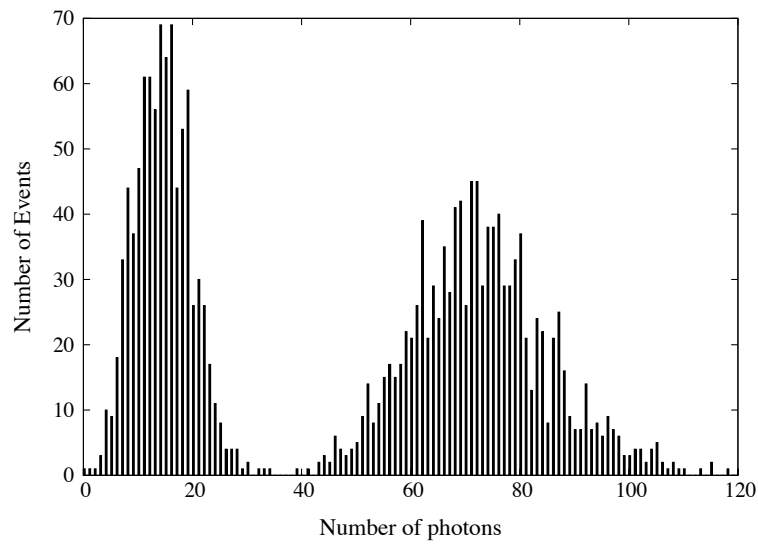


Figure 10.2: Histogram of events from an experimental run. There are two peaks, the lower one corresponding to a dark ion, and the higher one corresponding to a bright ion. The number of counts in the former case is not zero because of background light. The appropriate threshold in this experiment to distinguish bright from dark would be about 35 photons. A run with a long sampling window, about 50 ms, was chosen for demonstrative purposes.

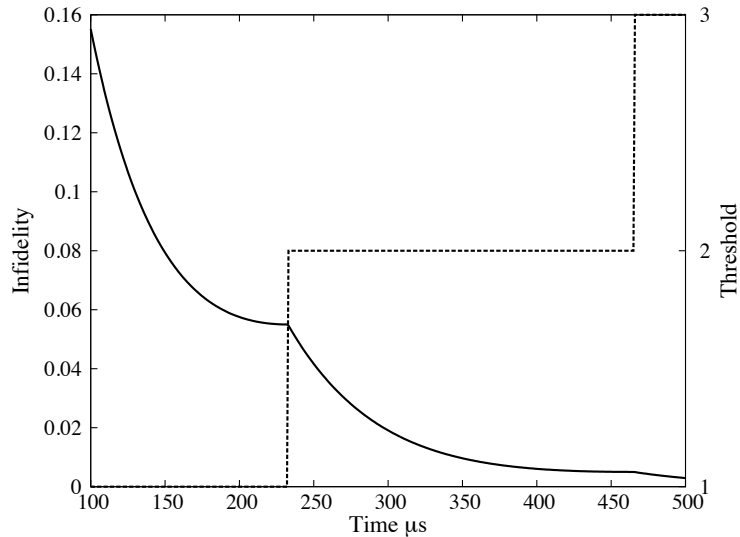


Figure 10.3: The solid lines shows the optimized detection infidelity that can be achieved after allowing for the user to set a threshold for detection higher than 1 photon. The threshold required to obtain said fidelity is shown as a dashed line. The number of background photons is assumed to be 200 per second, while the number of signal photons is 20000 per second.

figure 10.2. Two peaks occur, the first corresponding to a dark ion and the second to a bright ion. If we observe some number of photons during the detection window, we would like to know with what probability that belongs to the dark peak or the bright peak. This is most simply done by setting a threshold photon number below which we consider the ion dark and above which the ion is bright. In this way, it is possible to reduce the number of false positives caused by noise. Again assuming Poissonian statistics, it is possible to calculate the threshold number that gives the minimum error rate, and plot that error rate as a function of the window length. As shown in figure 10.3, by increasing the threshold number to 2 photons the error rate at a window of $332 \mu\text{s}$ is reduced to 1.2%. An exposure time of $350 \mu\text{s}$ is necessary to reobtain 99% fidelity. Notably, contrast is not the relevant factor. Since the standard deviation of *each* peak is \sqrt{N} rather than N , if one doubles both the ion fluorescence and the background noise, the detection time scales as $1/N$ as the fluorescence increases.

It has also incidently been found in ref [46] that not all significant forms of background

take on a Poissonian form, in particular, PMT detection of cosmic rays does not. In our setup, it was also found that intensity noise from our laser system has a variance substantially greater than Poissonian, which makes the preceding discussion an underestimate of the effect of noise sources. Furthermore, we have found that effects like background gas collisions can cause false dark events at the percent level. Finally, the lifetime of the excited state places another limit on the fidelity of these measurements, since as we increase the detection window to decrease infidelity due to other sources, that finite lifetime becomes increasingly prevalent. The previous reference also shows that this effect can be diminished somewhat by noticing that a spontaneous shelving event tends to have an abnormal number of photons near the end of the detection window.

10.2 *Selective Excitation*

We selectively excite the ion using a narrow band fiber laser at 1762 nm (see chapter 11). The anticipated Rabi frequency of this transition for a laser power of 20 mW with the designed focused waist size of about 70 μm is of order 10 kHz (see section 3.2), so that the fiber laser would need to be stabilized to a level much lower than this in order to be used for coherent transfer to the excited state. Instead, it was decided to effect the shelving using adiabatic passage [45]. This has the advantage that the laser only needs sufficient stabilization to avoid other transitions. The nearest observed transition occurs about 700 kHz away due to the axial secular frequency of the trap. This occurs at the expense of speed - adiabatic passage requires as a precondition that the interaction Hamiltonian change slowly with respect to the strength of interaction, that is, the Rabi frequency. For details, see section 3.1. The result of such an experiment as a function of exposure time can be seen in figure 10.4.

The optical setup for adiabatic passage was chosen to allow for rapid and smooth changes in the frequency observed by the ion without disrupting the cavity lock. Therefore, the AOM used for switching the IR laser to the ion is also used for sweeping the laser frequency (figure 10.6). That AOM is driven by a voltage controlled oscillator (VCO) which is itself set by an analog ramp generator box that can be triggered by a digital signal from the computer, the circuit diagram of which can be found in figure 10.5.

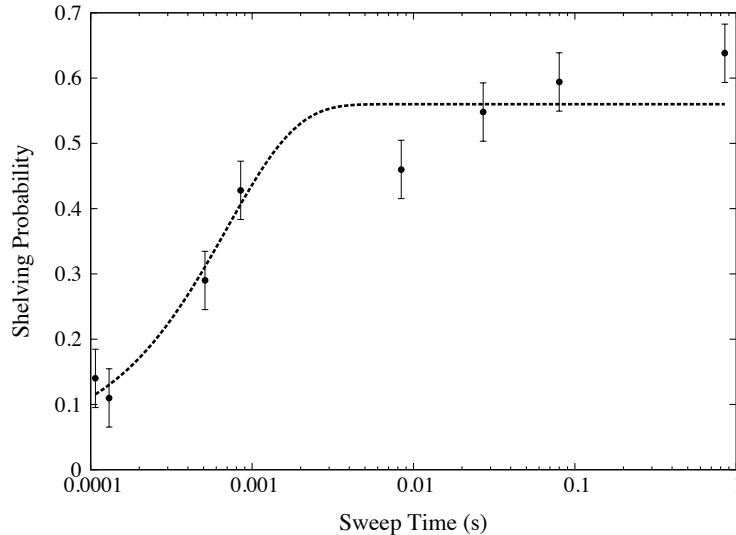


Figure 10.4: Adiabatic passage efficiency as a function of sweep time. The fit is according to equation 3.7. The parameter C is used to simulate the effect of the limitation at 60%, which is due to poor ion cooling and 1762 nm laser incoherence.

It is necessary to ensure that the ion is only exposed to 1762 nm light while the ramp is occurring, so that the AOM is activated only when the ramp begins and deactivated as soon as the ramp ends. Since the analog control box sets the ramp size and duration, the computer is unaware of when exactly the ramp ends. Thus, an analog comparator is used to judge the beginning and end of the ramp period. This makes it possible to accurately control the AOM switch as well as measure the ramp time. A similar feat can be accomplished using the analog trigger feature of some National Instruments DAQ boards. One must utilize a Schmitt trigger in order to ensure a clean trigger from the analog ramp signal.

10.3 Deshelving

Once the ion has been shelved and the dark state has been correctly identified, it is necessary to deshelve the ion and return it to the cooling cycle in preparation to perform the experiment again. A number of methods have been attempted in this research.

The most obvious is directly through the 1762 nm quadrupole transition, however this requires the entire apparatus of the infrared laser to be operating and available. We have

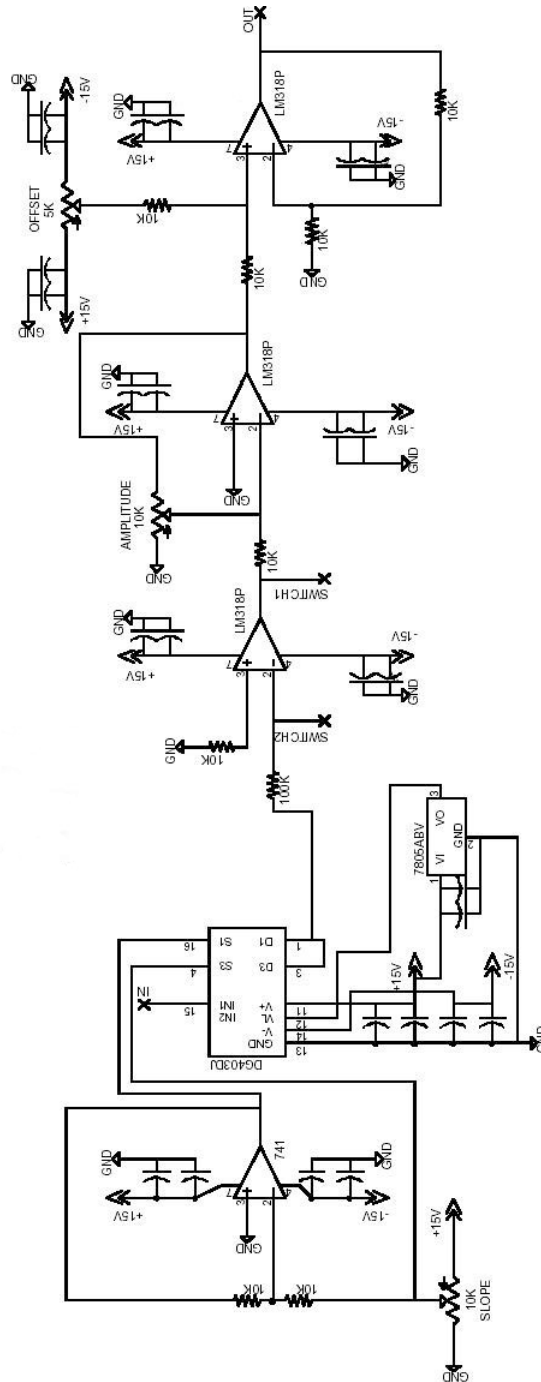


Figure 10.5: Circuit diagram of analog ramp generator.

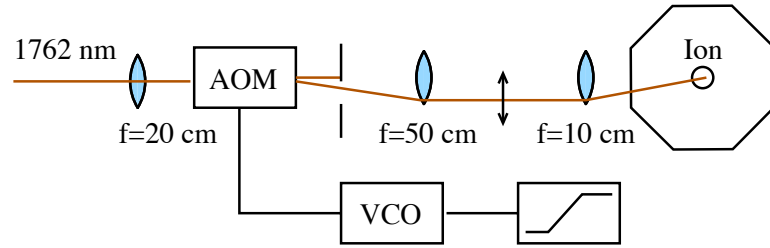


Figure 10.6: The optical setup of the adiabatic passage system. The AOM frequency is swept, which causes some a change in deflection for the first order beam. However, the two lenses which follow the AOM effectively image the focal point of the first lens onto the ion. Thus, as the frequency sweeps, even though the 1762 nm beam shifts vertically, the focus of the last lens remains in place.

demonstrated a somewhat simplified, unstabilized version of this technique where the infrared laser and 493 nm cooling laser are activated together, without the 650 nm laser. This ensures that once the 1762 nm transition is driven, it is never driven back into the shelved state, since the 493 nm laser optically pumps the ion into the $D_{3/2}$ state. This method can be performed in less than 50 ms. It can also be deshelled indirectly through the $P_{3/2}$ state, where the $D_{5/2}$ to $P_{3/2}$ transition is driven until the ion spontaneously decays into the ground state. This transition occurs at 614 nm, for which no convenient laser exists. Broadband LEDs near this wavelength have been used in the past, but because of the low spectral density prove very slow, requiring more than 100 ms of exposure to successfully deshelve the ion. An alternative is to generate the light from a doubled 1228 nm stabilized diode, an expensive and somewhat difficult proposition. Finally, we have preliminary data on the possibility of deshelling through the $D_{5/2}$ to $P_{1/2}$ magnetic quadrupole transition at 685 nm. This will be necessarily slower than the 614 nm laser approach, and is currently under evaluation.

Chapter 11

STABILIZATION OF FIBER LASER**11.1 Motivation**

The Koheras 1762 nm fiber laser exhibits frequency drifts on the order of megahertz per hour, which is much too high to maintain successful adiabatic passage throughout a lengthy data run. Since the wavelength is too long to be detected by the silicon photodiodes in our commercial wavelengthmeter, we have few available resources for monitoring or locking the infrared frequency. As a result, we opted to stabilize the laser with respect to an available high finesse optical cavity [79] that had previously been used for a similar purpose. This cavity has a free spectral range of 500 MHz, and a finesse of about 1000, giving it a linewidth of 500 kHz.

However, the drifts associated with an open air optical cavity, even one made from ZerodurTM glass, are still too great for the task at hand. The principal source of error is shifts in the ambient air pressure. A quick estimate concludes that a shift in air pressure of 1 mbar would correspond to a frequency shift of roughly 500 MHz. Clearly, for the cavity to be any use at all it must be sealed in an airtight container.

The next significant source of drift is related to temperature. Using the thermal expansion coefficient of ZerodurTM, which is about 100 ppb/K at 35°C, one can conclude that a 1 degree Kelvin shift in room temperature would result in a drift of roughly 17 MHz. Since we would like to independently access the carrier and sideband during an experiment, which sit a few hundred kHz apart, the cavity temperature can drift by no more than 20 mK or so. In order to map out one of the quadrupole resonances, drifts less than 1 kHz are required, which would mean 50 μ K stability.

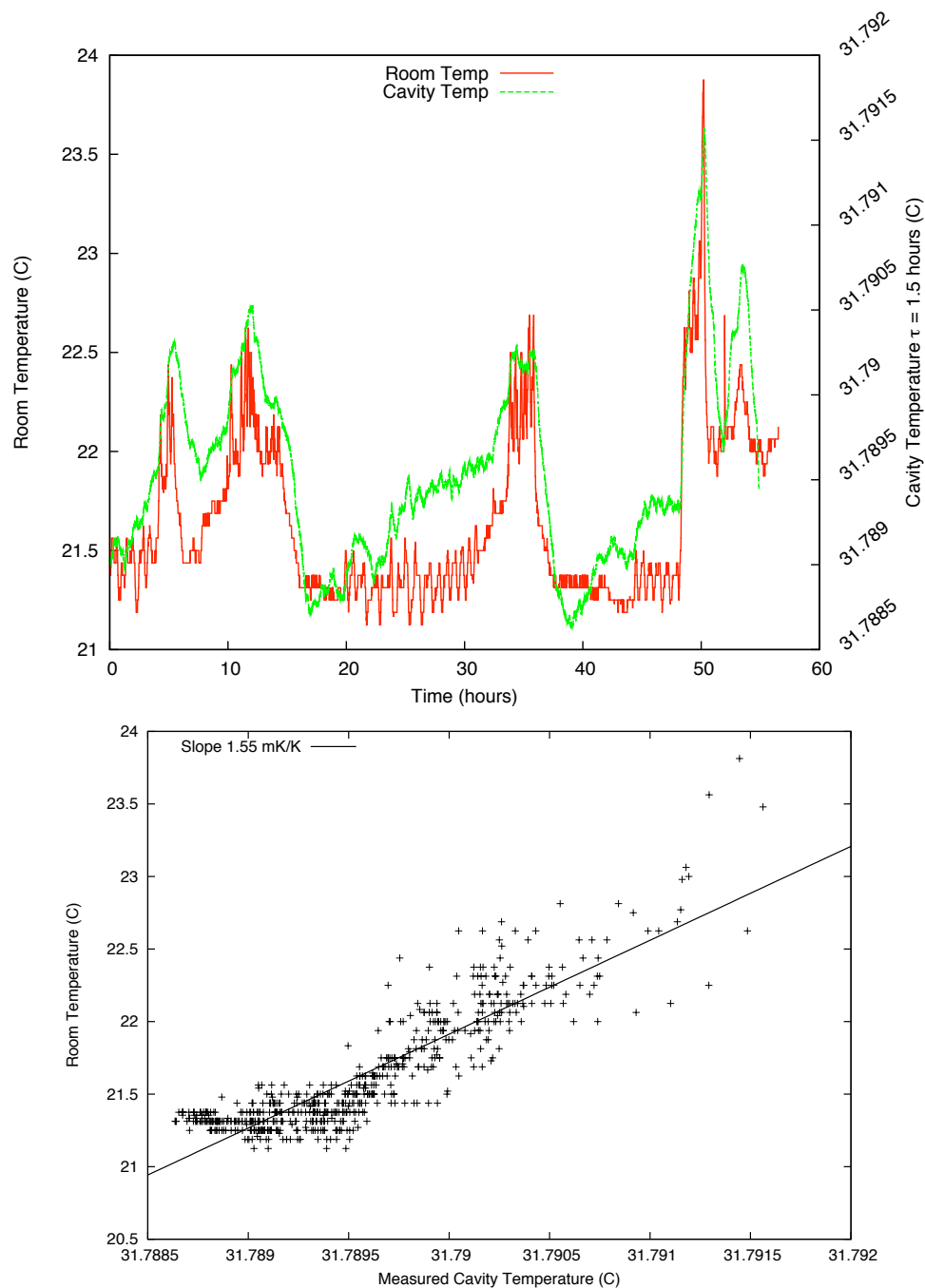


Figure 11.1: Data related to the temperature stabilization of the optical cavity. In the first, the room temperature and cavity temperature are plotted together. In the second, room temperature is plotted versus cavity temperature in an effort to extract a correlation, which is observed to be about 1.5 mK/K. In both cases, the cavity temperature is found by time averaging the raw measured data of the vacuum chamber's surface, in an effort to determine the actual temperature of the optical cavity.

11.2 Setup

These goals are best accomplished by sequestering the cavity in a vacuum, the walls of which are temperature controlled by a servo circuit, shown in figure 11.2. From the geometry and thermal properties of the vacuum chamber and optical cavity, blackbody radiation is expected to cause a thermal time constant of about 1.5 hours, which has been substantiated by cavity line shift rates observed after disabling the temperature controller. Our ability to measure the temperature stability is limited by the performance of the ADC in our National Instruments card, which is greatly distressed by the noisy electrical environment of our lab. Additionally, according to specification has a significant temperature coefficient in any event, 25 ppm/K, or about .6 mK/K, where a correlation of 1.5 mK/K is observed (see figure 11.1). The lab room temperature varies greatly as a result of being a rather small room (roughly 14' by 14' by 19') without an independent thermostat filled with a large amount of high power dissipation electronics. Shifts of 1-2 Kelvin are observed between having the lab door open and shut. Since the correlation of measured cavity temperature to room temperature is quite strong, good temperature stability can be achieved in any event by ensuring that the room door remains open during experimental runs.

The construction of a good temperature controller involves the management of many systematics, since it is desired to measure the temperature to high precision with low drift over long periods of time. One important systematic involves the temperature coefficient of various resistance references within the control box. The resistor labeled as being metal film needs to have an extremely low temperature coefficient, since it is being used as an absolute temperature reference for measuring the thermistor resistance. A carbon film resistor can easily have 100 ppm/K coefficients, which will be several millikelvin per degree change ambiently. Similarly, the setpoint potentiometer should never be two separate components, since it is critical that the resistance above and below the wiper have the same temperature coefficient and be in thermal equilibrium. Also, despite being in a Wheatstone bridge configuration, V_{ref} must not be allowed to drift, since this will cause the heat dissipation of the thermistor to change, causing a drift in the temperature difference of the cavity and thermistor. In this case, even if the temperature controller reports the thermistor to be

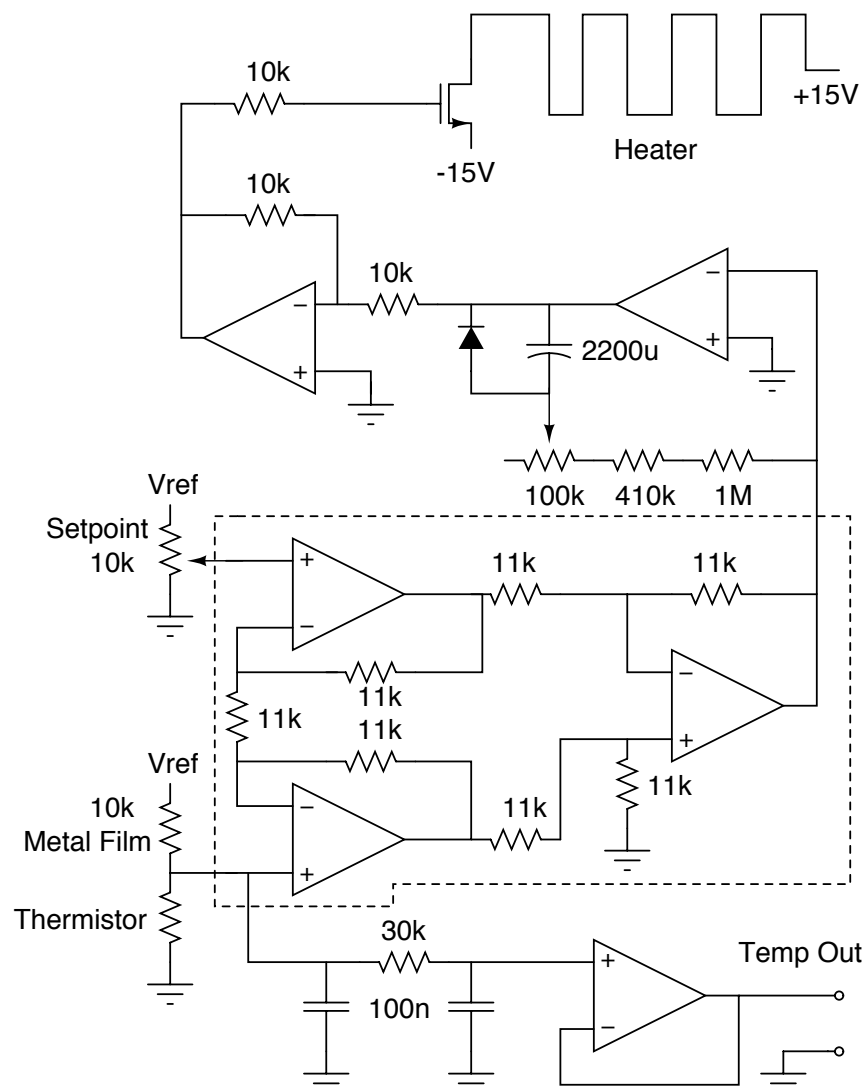


Figure 11.2: Circuit diagram of the temperature controller. The op amps are all LF411. The portion contained in the dashed line is equivalent to an instrumental amplifier, and should be replaced by a single commercial device, such as an AD620 or INA128.

perfectly stable, the cavity temperature will vary uncontrollably. A low drift, low voltage output linear regulator should be used to generate V_{ref} . At some level, the thermoelectric effect will become significant in measuring the thermistor resistance. Finally, the leading systematic in the circuit shown here is the poor temperature coefficient of the home built instrumentation amplifier. The two inputs of any operational amplifier have a voltage offset between them, and unfortunately, this voltage offset is temperature dependant. A precision commercial device should be used in that place with high CMRR and low drift.

Precision measurements of the narrow quadrupole transition in barium has demonstrated that the temperature stability of the ZerodurTM cavity is at least at the level of $200\mu\text{K}$ over several days, since the transition has been observed to be stable within our 5kHz resolution on that time scale, figure 11.4. An earlier longitudinal study showed stability within a 100 kHz (60 mK) resolution over 3 months, see figure 11.3. In any event, experience has demonstrated that the temperature stability is more than sufficient for the needs of adiabatic passage and simple spectroscopy.

The customary method of locking a laser to a Fabry-Perot cavity is the Pound-Drever-Hall technique [5]. In this method, the laser to be locked is frequency modulated and then guided into the cavity. The rejected, retroreflected beam off the cavity mirror surface is detected with a fast photodiode. This electrical signal is then mixed with the modulation signal and amplified to create a suitable error signal for feedback control, see figure 11.5.

The appropriate method of laser modulation is an interesting topic. If the laser oscillator itself is modulated directly, the modified frequency spectrum will exist on the entire beamline, including that laser light which is directed to the ion. Moreover, the modulation frequency sets the absolute possible bandwidth of all other processes, and so it is desirable to make this frequency very high, in excess of a MHz if one wishes to obtain 100 kHz feedback bandwidth reliably. But the existence of such a high bandwidth modulation mechanism on the laser introduces a major source of possible noise, which should be avoided. The traditional method uses an electro-optic modulator (EOM) to create the necessary sidebands on only the beamline to the cavity. This technique has some of its own problems, mostly associated with the large size of the crystal usually required. Not only is such a device quite expensive, but its large capacitance and high voltage requirements (V_{π} commonly in excess

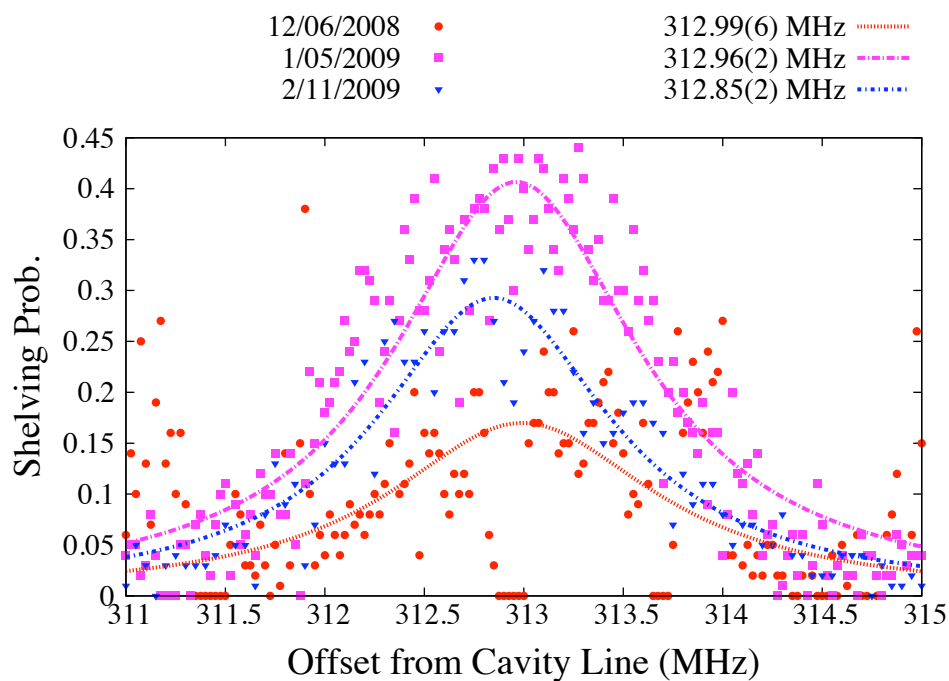


Figure 11.3: A longitudinal study of cavity stability. The location of the $^{138}\text{Ba}^+$ resonance is measured over several months, and a shift smaller than the linewidth of the optical cavity is observed.

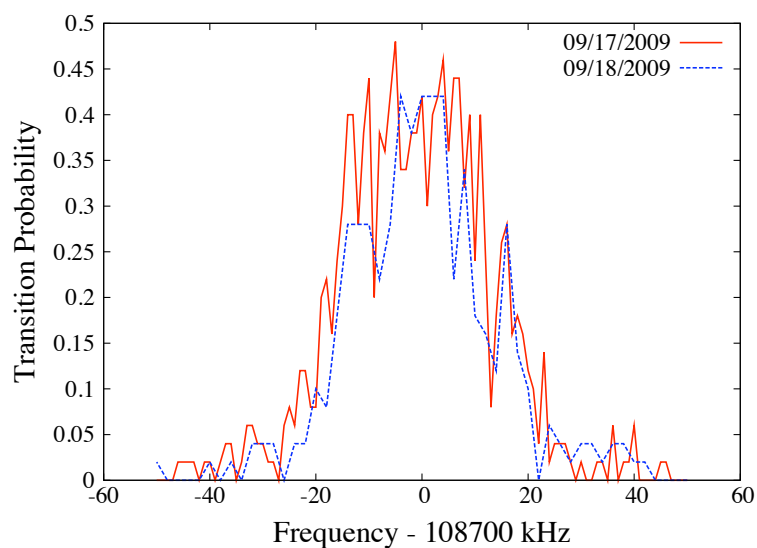


Figure 11.4: A shorter, higher resolution demonstration of cavity stability. The same ion transition is measured on two different days, and found to have the same displacement with respect to the ZerodurTM cavity.

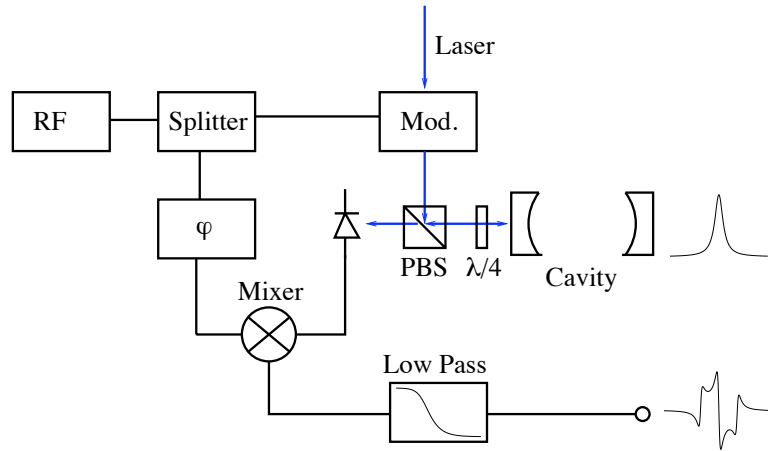


Figure 11.5: An abstracted block diagram of a generic PDH system. The function of a PDH setup is to convert a Lorentzian transmission peak into a useable error function. The modulation shown in the figure can be one of several different types, as discussed in the text, but must create frequency modulation of the laser beam.

of 1 kV) makes it difficult to drive with RF.

An alternative method involves a double passed acousto-optic modulator (AOM). Since the frequencies of the cavity resonances is largely determined by temperature, an electronic frequency shifting mechanism is almost always required to make up for the difference between the ionic resonance and cavity line. This is usually accomplished by sending laser light through an AOM twice to rob the device of its frequency/angle dependence. Since that device is required anyhow, why not use it for our modulation needs? AOMs can also be purchased more cheaply and driven with RF more easily than EOMs.

A few cautions are in order however. First, AOMs have a frequency dependent diffraction efficiency, which will cause any frequency modulation to be mirrored to some extent in the form of amplitude modulation. Amplitude modulation at the PDH modulation frequency will appear to the system as a frequency independent offset to the error signal. This would be acceptable and easily canceled if the total laser power would remain perfectly stable, but it does not, and the resulting drifts and noise appear effectively as signal on the PDH circuit. This so called residual amplitude noise is a major limiting factor in EOM based schemes, where it results from etalon effects in the crystal [75, 68]. For AOMs, it means that

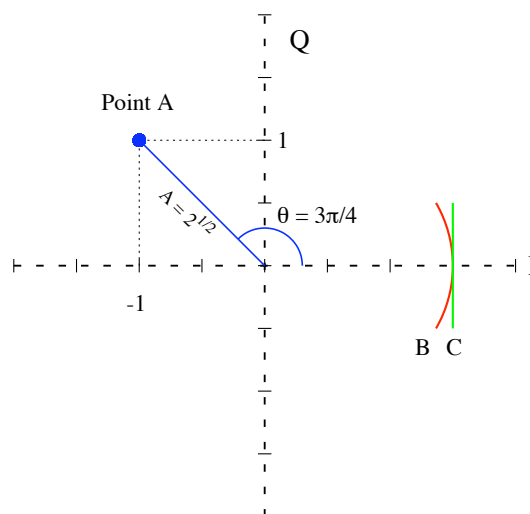


Figure 11.6: A simple sketch of the action of an I/Q modulator on an input signal, and demonstration that it can be used to approximate an FM signal. Point A represents an output that has the same frequency as the input, offset in phase by $3\pi/4$ and an amplitude of $\sqrt{2}$. Curve B is exact frequency modulation, and curve C is the approximation most suitable for an I/Q modulator.

the modulation frequency is limited by the flatness of the diffraction efficiency curve. In our case, dramatic improvement to the residual amplitude noise was observed at modulation frequencies below 1 MHz. Also, there is some improvement by selecting frequencies that place the central frequency at the top of the (roughly quadratic) gain curve. This causes the amplitude modulation to appear at twice the system modulation frequency and be eliminated by the lowpass.

The second caution regards a subtlety in RF modulation. A common RF mixer will generate not frequency modulated output, but rather amplitude modulated output. When this is sent to the AOM, the laser intensity will be affected rather than frequency, and the PDH system will fail. The usual method for obtaining an FM signal in the lab would be to modulate the RF source directly, but the modulation bandwidth of most voltage controlled oscillators (VCOs) and RF synthesizers is less than 100 kHz, which greatly limits the entire scheme. Fortunately, RF engineers have provided us with an alternative in the form of I/Q modulators. With careful manipulation of the two I/Q inputs, practically any form

of modulation of a third input carrier signal can be achieved. One can make a reasonable approximation of FM by inputting a DC signal into the I port and the modulation signal into the Q port. Reversing the roles of I and Q gives the same result, except phase shifted by π radians, which has the net effect of flipping the error signal's sign. Some amplitude modulation occurs from this approach, but it is at twice the modulation frequency, where it is filtered out by the PDH circuit.

An I/Q modulator generates points directly on the I/Q plane. The I/Q plane should be thought of as plot of phase where the I (in phase) axis rotates in phase with the input carrier sine wave, see figure 11.6. Thus, a point that rests on the Q (quadrature) axis proceeds at the same frequency as the carrier, but 90 degrees out of phase with it. The radial distance corresponds to the output amplitude, so that a point at the origin is zero output. An I/Q modulator takes an input carrier and generates an output that corresponds to its I and Q inputs. Thus, point A in figure 11.6 could be generated by providing -1 (in some units, say mA) to the I input, and 1 to the Q input. It is useful to think of the I/Q plane as being the xy plane of a Bloch sphere (see section 1.1).

In this picture, frequency modulation appears as oscillation along a circular arc centered at the origin, as in curve B of figure 11.6. This corresponds to a sinusoidally varying phase with constant amplitude output. However, to generate this on an I/Q modulator would be difficult since it requires two carefully balanced oscillating signals out of phase with one another, one with a DC offset. Instead, it is possible to approximate an FM signal by applying a DC signal to the I input and sinusoidally varying the Q input, as in curve C. For small modulation amplitudes, this provides an excellent approximation. Furthermore, its principal deviation from an FM signal is that the amplitude also varies, so that there is AM as well. However, the AM occurs at *twice* the modulation frequency; as can be seen from curve C, for every one full cycle the output takes along that curve, it passes the minimum amplitude twice.

In implementation, the I/Q modulator works well, but has problems related to an internal phase shifter. Because RF phase shifters are inherently narrow band, the input carrier frequency is restricted to a range slightly smaller than the normal bandwidth of our AOM, about 20 MHz. Also, within this range the device's responsivity is not very flat, which has

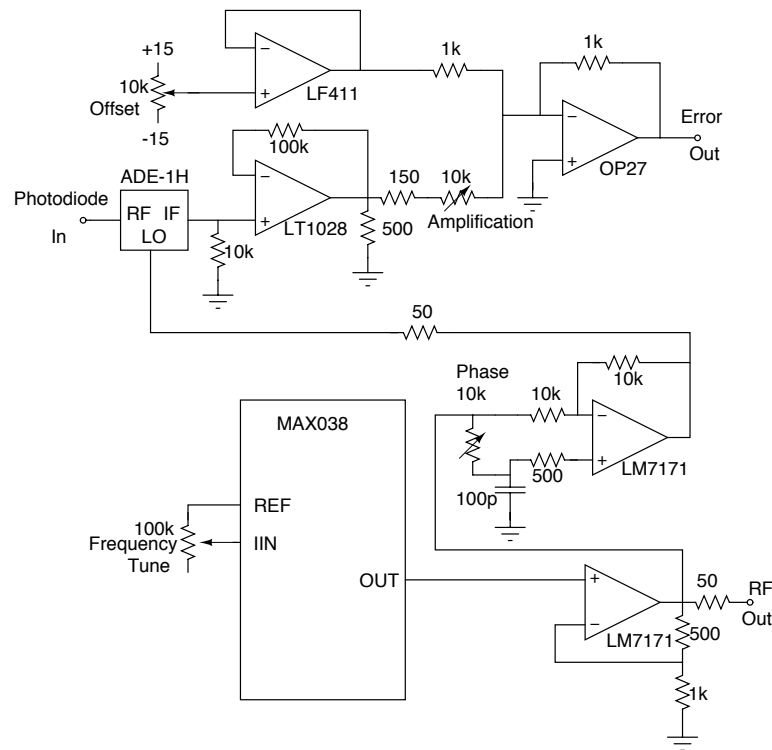


Figure 11.7: A circuit diagram of a complete Pound-Drever-Hall system. The MAX038 generates an RF signal at a frequency determined by a potentiometer, which is then split. One path is amplified to a useful level then output to the I/Q modulator. The other path is phase shifted and mixed using a Minicircuits ADE-1H surface mount RF mixer with the photodetector output. This mixed signal is amplified using the low noise LT1028, then added to an offset before being sent to the microcontroller servo. Future designs should use a DDS programmed with some microcontroller in order to extend the usable bandwidth and improve noise characteristics.

the effect of a frequency dependant offset to the PDH signal. It would be interesting to find an I/Q modulator that doesn't rely on a phase shifter, since that should be free of such defects. One nice feature of operating in the range of about 1 MHz modulation frequency is that all signal processing can be done easily with an op amp circuit rather than the usual combination of RF phase shifters and amplifiers. A diagram of the circuit used here can be seen in figure 11.7.

Once the error signal is generated, a servo mechanism must be put in place to lock the laser onto one of the cavity lines. Although the nominal circuit required for feedback

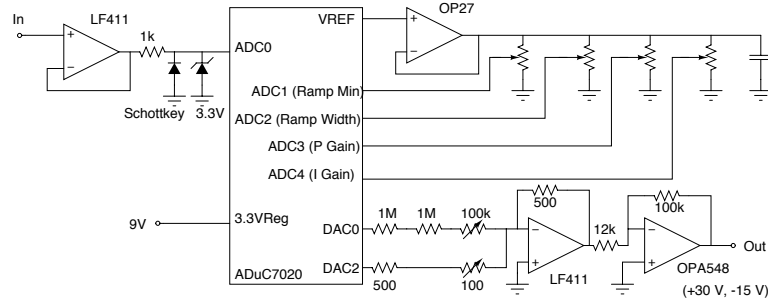


Figure 11.8: Circuit diagram of the microcontroller based servo mechanism.

is relatively simple, experience has shown that the experimenter's quality of life is greatly improved if the servo has a number of important features. For one, a frequency scan mode is needed so that the experimenter can make a comparative selection of the correct cavity line. This is necessary because all cavity resonances look the same for a properly mode matched cavity except for a slight difference in intensity. It is also important to have some mechanism for detecting when the laser has unlocked and rellocking it to the correct line, rather than to one of its neighbors. An entire experimental run can be ruined if the operator fails to notice that the laser has acquired a lock on the wrong cavity line while he wasn't looking.

This list of features is best implemented not with a sophisticated analog circuit, but with a digitally controlled one, whose behavior can be programmed on a computer. Microcontrollers are ideally suited for this task, since they contain integrated analog and digital peripherals such as analog/digital and digital/analog converters and counters. This greatly simplifies the programming process, since no time need be wasted learning to communicate to off-chip peripherals via some bus standard. The implemented circuit can be found in figure 11.8.

This type of digital programmable design has considerable promise. The circuit is simple and can be rapidly reproduced, saving students many hours of labor. Normally an analog circuit would have to be modified for the exact specifications of the specific laser system at hand, and those changes frequently cause subtle problems in an existing design which can be extremely difficult and time consuming to debug. With a digital design however, the

program can be rapidly altered and tested without any need for soldering or readjustment. Since a digital processing unit is involved, the entire gamut of digital signal processing techniques can in principal be applied to the feedback loop, enabling the user to rapidly field and test sophisticated filters or experiment with various gain curves without resorting to difficult analog filter design.

Another useful technique made available by the microcontroller lock technique is the ability to identify piezo resonances. By programming the microcontroller to issue a slight impulse to the laser's piezo while maintaining a frequency lock, the response function of the laser system can be identified by observing the behavior of the PDH error signal. Since the timing of the impulse is precisely known, it is possible to trigger on the event and average over many runs, giving an extremely high resolution scan. The results of this experiment on the KoherasTM laser system can be found in figure 11.9. The peaks correspond to piezo mechanical resonances, notice that the lowest is at about 32.6 kHz, which puts an absolute upper bandwidth limit on any laser lock performed using the piezo actuator.

Unfortunately two facts became clear during the implementation of this servo. First, the noise floor of the on board DACs is too great to provide an adequate dynamic range. Even though naively one would expect that two 12 bit DACs could be combined into a single 24 bit DAC, it so happens that the noise floor of conventional DAC design is very high, and they are usually designed with only a slim margin between the bit resolution and effective analog signal to noise ratio (SNR). Care is required on the part of the designer since many DAC designers "neglect" to specify the noise floor well, as is the case with the ADuC7020. Most DACs can not be combined to make a DAC with even 1 additional bit of resolution, let alone 12. This is partly because dithering is considered a desirable trait in converter design, since it reduces correlated distortion such as harmonic generation.

Secondly, the sampling rate in our final design was 250 kHz, which would nominally give us a usable analog bandwidth of perhaps 25 kHz, adequate considering the lowest piezo resonance of 32.6 kHz. However, when examined, the system demonstrated an excessive group delay (see figure 11.10) with 360 degrees of phase at the Nyquist frequency (72 degrees at 25 kHz), four times what would be expected from a zero order hold. This is because the microcontroller does not actually output a response for the first sample until it

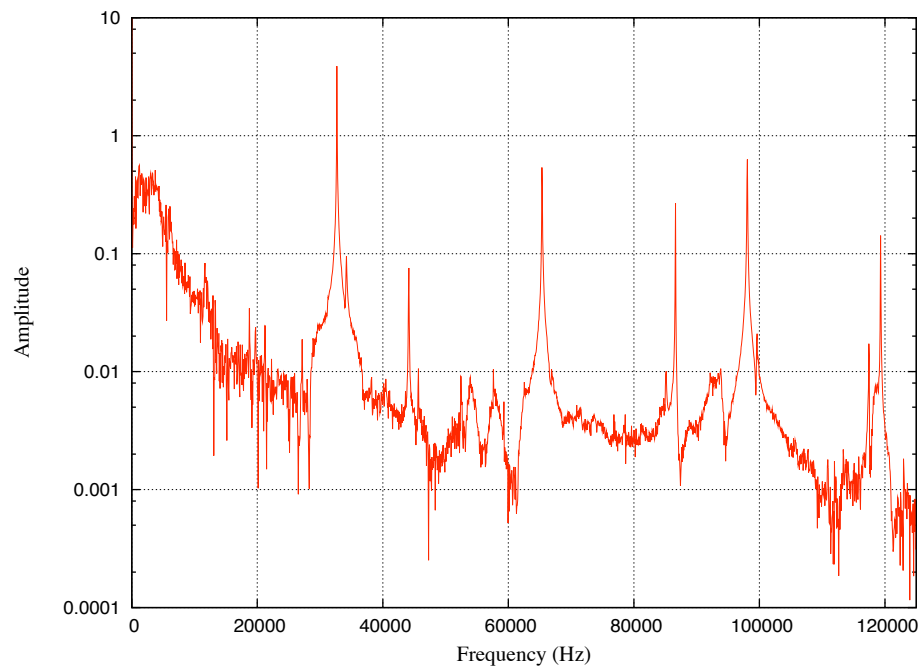


Figure 11.9: A high resolution frequency scan of the fiber laser's response function, which was facilitated by features of the digital lock box. The above represents 10^5 captured and averaged impulse events.

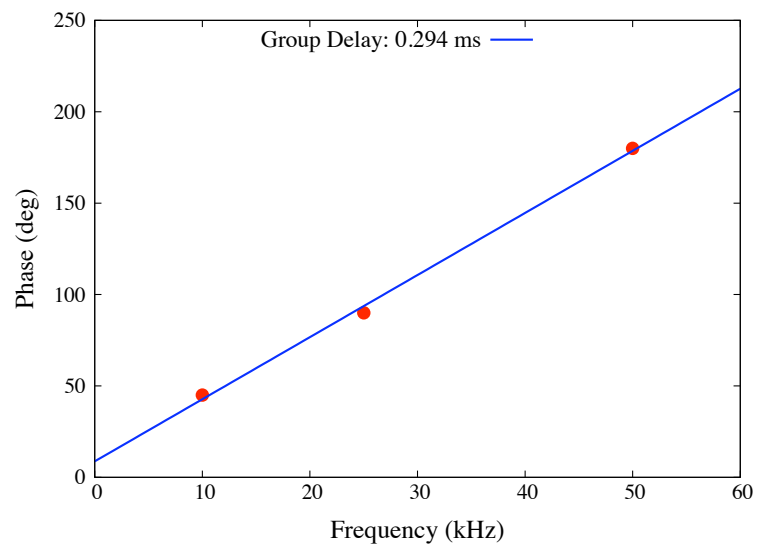


Figure 11.10: A measurement of the delay associated with the microcontroller lock box. Critically, the slope is linear, so there is very little dispersion and the group delay is about $300 \mu\text{s}$. A pure group delay is suggestive of a digital sampling rate problem, since analog filters tend to give a highly dispersive shape, but slow sampling gives a pure group delay. This data was taken by observing the lock box's input and output in XY mode on an oscilloscope, leading to Lissajous figures. This accounts for the low number of data points.

has already initiated the third sample, causing a substantial servo delay. Although in audio processing group delay is irrelevant, in feedback design the loss of phase margin is fatal and the servo was routinely observed to oscillate at the 5-10 kHz range due the combined phase shift of output filters and microcontroller group delay. The digital filter exasperated the problem, since without that feature the sampling rate was much greater (closer to 600 kHz) due to the reduction in needed processing power.

For now, these combined problems have been solved by heavy filtering of the piezo input, effectively reducing the lock bandwidth to a couple hundred Hz, which is sufficient to servo out some 60 Hz noise associated with the lab's AC power. This results in a laser with total stability better than 10 kHz integrated over several hours, as indicated by observations of the quadrupole transition. Future development could lead in several directions. The Toptica DigilockTM system is entirely based on a field programmable gate array (FPGA), ostensibly using its massive parallelism and high clock speeds to avoid our observed group delay issues. Programming an FPGA is more expensive in terms of time and resources than a microcontroller, and moreover still faces many of the noise/dynamic range problems that would be faced with any pure digital technique. Implementing a digital filter would be more difficult on an FPGA based system than on a microcontroller or DSP for example. One could also imagine a mixed analog/digital system where the digital part is only responsible for implementing the basic frequency scan and relocking features, while all the feedback is managed by an analog stage. This of course completely abandons the filter and gain curve manipulation described earlier, and is similar to a product offered by Stanford Research Systems. The approach closest to the one already attempted would be to replace the microcontroller with a digital signal processor (DSP) having a much higher clock rate and several fast ADC and DACs with which the DSP communicates through a bus. A DSP seems ideally suited to the aforementioned goals; some DSPs even possess built in digital filter coprocessors. With proper selection of converters, a setup like this may very well manage all the desired features.

11.3 Results

The best measurement of laser noise available is to generate an Allen or Hadamard deviation plot by beating two independently stabilized lasers against one another and analyzing the spectral properties of that beat pattern [38]. However, no second laser or optical cavity is available to make such a measurement. Another rigorous test is to use the laser to measure the linewidth of Ba^+ . This is possible, and we have done it. However, such a test tells the experimenter little about the nature of the noise and requires lengthy data runs, half an hour or longer to obtain a curve. The most expedient path is to assume the cavity is a perfect, noise free resonator and use the electronic error signal generated by the servo loop as a measurement of laser noise. This is preferable because it is a measurement that can be rapidly performed and gives spectral information about the nature of any frequency noise. Unfortunately, it is difficult to connect the result of such an experiment to an actual laser linewidth, and so is mostly useful as a diagnostic tool rather than an absolute measurement of frequency stability.

Since cavity noise associated with vibration or thermal fluctuation is expected to be at the 100 Hz level, the noise free optical cavity assumption should be meaningful at this level of precision, since the specified laser linewidth is of order 20 kHz. Another issue is noise introduced by the PDH detection itself, such as amplitude residual noise. This will cause any noise measurement to be systematically high, and in any event can be studied by measuring the error signal spectrum when the laser is non-resonant with the cavity or blocked entirely. One possible issue is that the error signal will not contain information about any noise above the bandwidth of the PDH detector, and so if that bandwidth isn't high enough to capture all of the important signal, the total noise might be underestimated. An example of this technique at work can be found in figure 11.11, where the error signal is evaluated with and without a low pass filter on the laser piezo input. The dramatic improvement on the noise at most frequencies is a result of filtering out the large noise contribution from the microcontroller's DAC system.

The most rigorous test is a measurement of the quadrupole line shape. This type of experiment is sensitive to any frequency deviation of the laser happening on a time scale

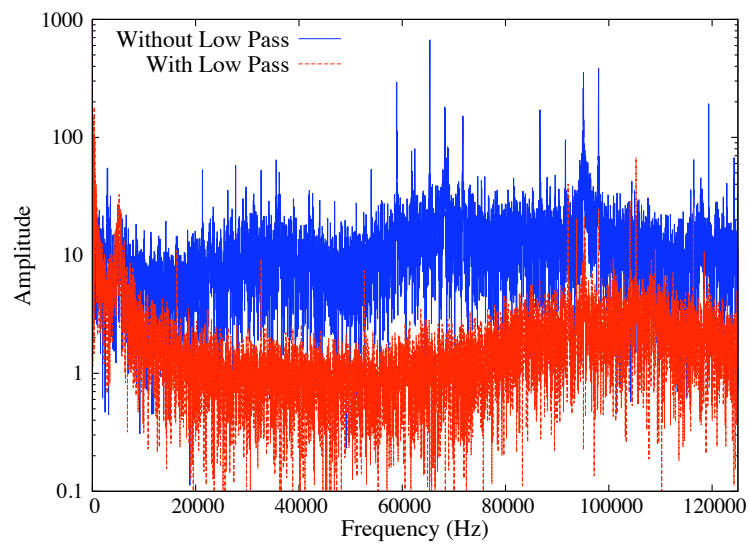


Figure 11.11: Laser noise measured from the PDH error signal with and without a low pass filter on the laser piezo input. Since placing a low pass filter at that stage does not directly influence the PDH output, the improvement must be because of an actual decrease in laser noise. Notice that most of the remaining noise exists below 10 kHz, a fact that remains unchanged even with a lower cutoff filter. Since the piezo bandwidth is 32 kHz (see figure 11.9), there is hope that this noise can be servoed out with an improved lock box.

faster than that of the experimental run. And since the ion's natural linewidth is less than 1 Hz and mostly drift free, it is immune to the concerns associated with the optical cavity. If the frequency scan takes 1 hour to complete, any noise or drift faster than $280 \mu\text{Hz}$ will appear as broadening to the line shape. The problem is that no information of any kind can be obtained about the nature of this noise; since the spectral width of a noise broadened laser is not related simply to the noise amplitude [1], not even that can be determined with any certainty. Moreover, if the barium transition is observed to be broad, it can be difficult to demonstrate that this is not due to the temperature of the ion itself, rather than the laser. Regardless, if the shape is found to be narrow, then a rigorous lower bound on the stability of the laser can be stated.

The exact sequence for this type of experiment consists of two nested program loops. In the outer loop, the synthesizer controlling either the double or single pass AOM is first set to some frequency using the available GPIB controller. So long as the feedback loop remains locked, this precisely controls the frequency seen by the ion. Then, in the inner loop, an optical pumping sequence is performed as in chapter 8. Next, in much the same way as the microwaves in the Rabi flop experiment, the 1762 nm laser is exposed for a fixed period of time. Then the 1762 nm laser is deactivated and the cooling lasers are turned back on along with the 493 nm sidebands. Then the PMT is counted for some set time to determine if the ion is bright or dark. The result is recorded and if the ion was found to be dark, a deshelling sequence is initiated. Once deshelled, the inner loop is repeated. The inner loop is repeated for a fixed number of times in order to build up statistics for that specific infrared frequency. Only after completing that many cycles is the outer loop iterated, and the infrared frequency updated. The frequency is stepped by some fixed interval every outer loop iteration until the desired range is covered. The benefit of controlling the double pass synthesizer is that the ion is exposed to a uniform laser power throughout the scan, whereas if the single pass AOM is used, then the risk of laser unlock is greatly decreased.

Even if all this is accounted for, the lineshape measurement will still be only a lower limit on the laser stability, due to power broadening of the transition. Therefore, it is necessary to retake the lineshape at several laser powers in an effort to quantify this effect. Such an experiment can be seen in figure 11.12. The narrowest of these transitions has a linewidth

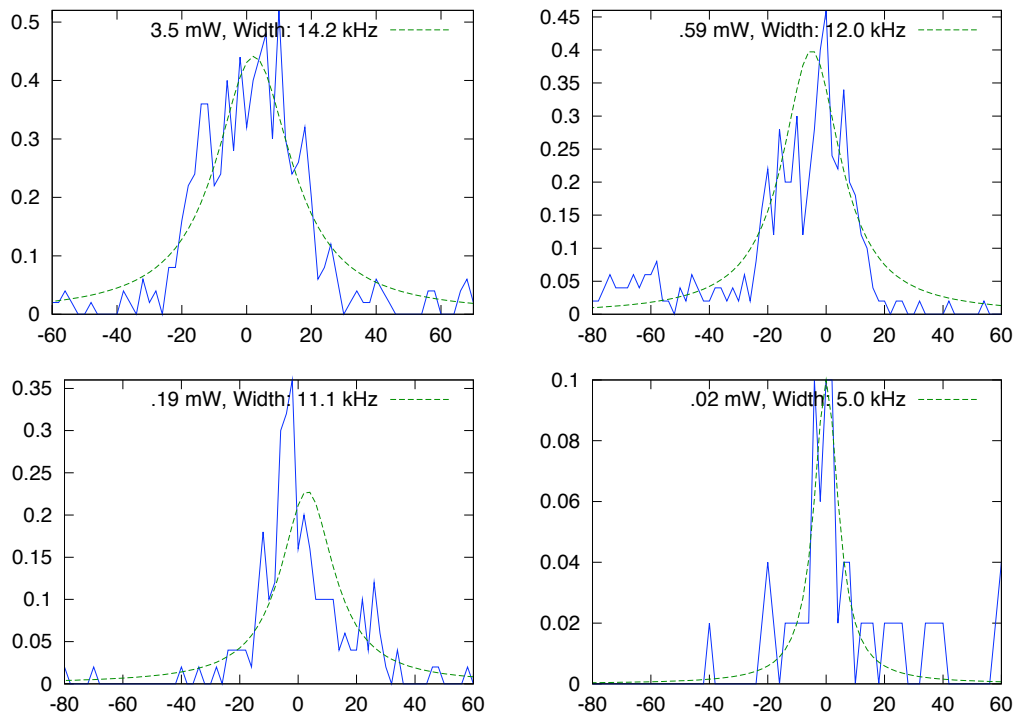


Figure 11.12: A demonstration that the resonance is power broadened. By decreasing the laser power, there is a decided decrease not only in resonance amplitude, but more importantly in width.

of 10 kHz, and took about 30 minutes to complete. Now, the analytic expression for power broadening is

$$\gamma' = \gamma\sqrt{1 + I/I_s} \quad (11.1)$$

where γ is the natural linewidth, I is the laser intensity, and I_s is the saturation power. Since γ is expected to be of order 200 mHz, this data would have to correspond to an enormous saturation number $s = I/I_s$. However, since the linewidth does not scale as the square root of power, we can conclude that we are nearly limited by some noise in either the ion or laser, so that the Rabi frequency should be of order the coherence time. This conclusion is consistent with observations from attempted optical qubit Rabi flop attempts, see chapter 9. Its worth noting that this is roughly consistent with our expected linewidth. If this transition is $F = 2$ to $F = 4$, waist size about 70 μm , and laser about 5 mW, then the expected Rabi frequency from equation 3.20 is about 20 kHz.

11.4 Conclusions and Outlook

The primary goal of this experiment, to demonstrate a hyperfine qubit, has been accomplished. Initialization, readout, and rotations have all been demonstrated in the preceding pages. However, the quality of these techniques remains poor. Especially in readout, work remains to obtain high fidelity readout. At this level of fidelity, it is not yet possible to demonstrate a violation of Bell's inequality without a detection loophole, and so multiqubit entangling gates will remain elusive until this problem is resolved. The heart of the issue probably lies in our failure to achieve coherence on the 1762 nm shelving transition. Even though the linewidth is dominated by power broadening, the noise remains too great for coherent excitation. Fortunately, it would seem that the bulk of the laser noise lies at a frequency accessible to feedback techniques, and so there remains hope that pursuit of an improved servo mechanism will yield increased contrast ratios. Another method would be to significantly increase laser power, since the requirement for coherence in this case is that the Rabi frequency be must faster than the decoherence time. Since the power broadening data suggests that we are very near this limit, an increase in laser intensity of a factor of 5

or more should accomplish a similar goal. Also, work continues on a reliable and versatile laser lock system, which will allow us to operate closer to the Doppler limit.

As for multiple qubit operations, the success of the 791 nm laser system is promising for our ability to perform same-trap entangling operations. Recently, Nathan Kurz has demonstrated 493 nm ultrafast pulses from a titanium sapphire laser system, which is extremely important for ultrafast gates and single photon generation for ion-photon entanglement. Gang Shu has also been working on trap designs that integrate an aluminum mirror to achieve high collection efficiencies, which will prove useful for the longer term goal of remote ion-ion entanglement.

BIBLIOGRAPHY

- [1] Michael Bass. *Handbook of Optics*. McGraw-Hill, New York, NY, 2001.
- [2] Gordon Baym. *Lectures on Quantum Mechanics*. Westview Press, New York, NY, 1990.
- [3] J. S. Bell. On the Einstein Podolsky Rosen paradox. *Physics*, 1(3):195, 1964.
- [4] D. J. Berkeland, J. D. Miller, J. C. Bergquist, W. M. Itano, and D. J. Wineland. Minimization of ion micromotion in a paul trap. *J. Appl. Phys.*, 83(10):5025–5033, May 1998.
- [5] Eric D. Black. An introduction to pound-drever-hall laser frequency stabilization. *Am. J. Phys.*, 69(1):79–87, January 2001.
- [6] B. B. Blinov, D. L. Moehring, L.-M. Duan, and C. Monroe. Observation of entanglement between a single trapped atom and a single photon. *Nature*, 428:153–157, March 2004.
- [7] Max Born and Emil Wolf. *Principles of Optics*. Cambridge University Press, Cambridge, UK, 1999.
- [8] Chris Bowick. *RF Circuit Design*. Newnes, 1982.
- [9] J. I. Cirac and P. Zoller. Quantum computations with cold trapped ions. *Phys. Rev. Lett.*, 74(20):4091–4094, May 1995.
- [10] Umakanth Dammalapati. *Metastable D-State spectroscopy and laser cooling of barium*. PhD thesis, University of Groningen, Groningen, Netherlands, 2006.
- [11] S. De, U. Dammalapati, K. Jungmann, and L. Willmann. Magneto-optical trapping of barium. *Phys. Rev. A*, 79(4):041402, 2009.
- [12] F. DeMartini and C. Monroe, editors. *Proceedings of the International School of Physics “E. Fermi” Course CXLVIII: Experimental Quantum Computation and Information*. 2001.
- [13] David Deutsch. Quantum theory, the Church-Turing principle and the universal quantum computer. *Proc. Royal Soc. of Lon. A*, 400:97–117, 1985.

- [14] Ralph G. DeVoe. Elliptical ion traps and trap arrays for quantum computation. *Phys. Rev. A*, 58(2):910–914, August 1998.
- [15] Ralph G. DeVoe and Christian Kurtsiefer. Experimental study of anomalous heating and trap instabilities in microscopic $^{137}\text{Ba}^+$. *Phys. Rev. A*, 65:063407, June 2002.
- [16] M. D. Di Rosa. Laser-cooling molecules. *The European Phys. J. D*, 31(2):395–402, November 2004.
- [17] Christopher R. Ekstrom, Christian Kurtsiefer, Dirk Voigt, Oliver Dross, Tilman Pfau, and Jürgen Mlynek. Coherent excitation of a He^* beam observed in atomic momentum distributions. *Optics Comm.*, 123:505–511, Feb 1996.
- [18] Christopher J. Foot. *Atomic Physics*. Oxford University Press, New York, NY, 2005.
- [19] J. J. García-Ripoll, P. Zoller, and J. I. Cirac. Speed optimized two-qubit gates with laser coherent control techniques for ion trap quantum computing. *Phys. Rev. Lett.*, 91(15):157901, Oct 2003.
- [20] Christopher C. Gerry and Peter L. Knight. *Introductory Quantum Optics*. Cambridge University Press, Cambridge, UK, 2005.
- [21] J. D. Gillaspay and C. J. Sansonetti. Absolute wavelength determinations in molecular tellurium: new reference lines for precision laser spectroscopy. *J. of the Opt. Soc. of Am. B*, 8:2414–2419, December 1991.
- [22] Geetha Gopakumar, Holger Merlitz, Rajat K. Chaudhuri, B. P. Das, Uttam Sinha Mahapatra, and Debashis Mukherjee. Electric dipole and quadrupole transition amplitudes for Ba^+ using the relativistic coupled-cluster method. *Phys. Rev. A*, 66:032505, September 2002.
- [23] Kurt Gottfried and Tung-Mow Yan. *Quantum Mechanics: Fundamentals*. Springer-Verlag, New York, NY, 2004.
- [24] U Griesmann, B Esser, and M Aslam Baig. The total photoionization cross section of barium including 7snp, 6dnp and 4fnd double excitations. *J. of Phys. B*, 25(16):3475–3488, 1992.
- [25] Lou K. Grover. A fast quantum mechanical algorithm for database search. *Proceedings of the 28th Annual ACM STOC*, pages 212–219, May 1996.
- [26] J. R. Guest, N. D. Scielzo, I. Ahmad, K. Bailey, J. P. Greene, R. J. Holt, Z.-T. Lu, T. P. O’Connor, and D. H. Potterveld. Laser trapping of ^{225}Ra and ^{226}Ra with repumping by room-temperature blackbody radiation. *Phys. Rev. Lett.*, 98(9):093001, 2007.

- [27] S. Gulde, H. Häffner, M. Riebe, G. Lancaster, C. Becher, J. Eschner, F. Schmidt-Kaler, I. L. Chuang, and R. Blatt. Quantum information processing with trapped Ca^+ ions. *Phil. Trans. R. Soc. Lond.*, 361:1363–1374, 2003.
- [28] T. Hasegawa and T. Shimizu. Removal of irrelevant isotope ions in the presence of laser cooling in a rf trap. *Appl. Phys. B*, 70:867–871, March 2000.
- [29] Philip C. D. Hobbs. Ultrasensitive laser measurements without tears. *Applied Optics*, 36(4):903–920, 1997.
- [30] Philip C. D. Hobbs. *Building Electro-Optical Systems: Making it All Work*. John Wiley and Sons, New York, NY, 2000.
- [31] John David Jackson. *Classical Electrodynamics*. John Wiley and Sons, Hoboken, NJ, 1999.
- [32] S. R. Jefferts, C. Monroe, A. S. Barton, and D. J. Wineland. Paul trap for optical frequency standards. *IEEE Trans. on Instrum. and Meas.*, 44(2):148–150, 1995.
- [33] M A Kalyar, M Rafiq, Sami ul Haq, and M A Baig. Absolute photoionization cross section from the $6s6p\ 1,3P1$ excited states of barium. *J. of Phys. B*, 40(12):2307–2319, 2007.
- [34] H. Knab, M. Schupp, and G. Werth. Precision spectroscopy on trapped radioactive ions: Ground-state hyperfine splittings of $^{133}\text{Ba}^+$ and $^{131}\text{Ba}^+$. *Europhys. Lett.*, 4(12):1361–1364, 1987.
- [35] P. J. Lee, B. B. Blinov, K. Brickman, L. Deslauriers, M. J. Madsen, R. Miller, D. L. Moehring, D. Stick, and C. Monroe. Atomic qubit manipulations with an electro-optic modulator. *Opt. Lett.*, 28(17):1582–1584, 2003.
- [36] D. Leibfried, R. Blatt, C. Monroe, and D. Wineland. Quantum dynamics of single trapped ions. *Rev. Mod. Phys.*, 75(1):281, January 2003.
- [37] D. Leibfried, B. DeMarco, V. Meyer, D. Lucas, M. Barrett, J. Britton, W. M. Itano, B. Jelenković, C. Langer, T. Rosenband, and D. J. Wineland. Experimental demonstration of a robust, high-fidelity geometric two ion-qubit phase gate. *Nature*, 422:412–415, March 2003.
- [38] Judah Levine. Introduction to time and frequency metrology. *Rev. Sci. Inst.*, 70(6):2567–2596, 1999.
- [39] M Lindberg and S Stenholm. The master equation for laser cooling of trapped particles. *J. of Phys. B*, 17(16):3375–3389, 1984.

- [40] D. M. Lucas, B. C. Keitch, J. P. Home, G. Imreh, M. J. McDonnell, D. N. Stacey, D. J. Szwer, and A. M. Steane. A long-lived memory qubit on a low-decoherence quantum bus. 2007, quant-ph/0710.4421.
- [41] W. W. Macalpine and R. O. Schildknecht. Coaxial resonators with helical inner conductor. *Proceedings of the IRE*, 47(12):2099–2105, December 1959.
- [42] D. N. Matsukevich, P. Maunz, D. L. Moehring, S. Olmschenk, and C. Monroe. Bell inequality violation with two remote atomic qubits. *Physical Review Letters*, 100(15):150404, 2008.
- [43] D. M. Meekhof, C. Monroe, B. E. King, W. M. Itano, and D. J. Wineland. Generation of nonclassical motional states of a trapped atom. *Phys. Rev. Lett.*, 76(11):1796–1799, Mar 1996.
- [44] Albert Messiah. *Quantum Mechanics*. Dover Publications, New York, NY, 1999.
- [45] Harold J. Metcalf and Peter van der Straten. *Laser Cooling and Trapping*. Springer, 2001.
- [46] A. H. Myerson, D. J. Szwer, S. C. Webster, D. T. C. Allcock, M. J. Curtis, G. Imreh, J. A. Sherman, D. N. Stacey, A. M. Steane, and D. M. Lucas. High-fidelity readout of trapped-ion qubits. *Phys. Rev. Lett.*, 100(20):200502, 2008.
- [47] Warren Nagourney, Jon Sandberg, and Hans Dehmelt. Shelved optical electron amplifier: Observation of quantum jumps. *Phys. Rev. Lett.*, 56(26):2797–2799, Jun 1986.
- [48] W. Neuhauser, M. Hohenstatt, P. E. Toschek, and H. Dehmelt. Localized visible Ba⁺ mono-ion oscillator. *Phys. Rev. A*, 22(3):1137–1140, Sep 1980.
- [49] Michael A. Nielsen and Isaac L. Chuang. *Quantum Computation and Quantum Information*. Cambridge University Press, Cambridge, UK, 2000.
- [50] S. Olmschenk, K. C. Younge, D. L. Moehring, D. Matsukevich, P. Maunz, and C. Monroe. Manipulation and detection of a trapped Yb⁺ ion hyperfine qubit. *Phys. Rev. A*, 76:052314, 2007.
- [51] E. Peik, G. Hollemann, and H. Walther. Laser cooling and quantum jumps of a single indium ion. *Phys. Rev. A*, 49(1):402–408, Jan 1994.
- [52] T. Petelski, M. Fattori, G. Lamporesi, J. Stuhler, and G.M. Tino. Doppler-free spectroscopy using magnetically induced dichroism of atomic vapor: a new scheme for laser frequency locking. *The Euro. Phys. J D*, 22(2):279–283, Feb 2003.

- [53] V. Pevtschin and S. Ezekiel. Investigation of absolute stability of water-vapor-stabilized semiconductor laser. *Opt. Lett.*, 12(3):172–174, 1987.
- [54] Michael O. Rabin. Probabilistic automata. *Information and Control*, 6(3):230 – 245, 1963.
- [55] M. Roberts, P. Taylor, G. P. Barwood, W. R. C. Rowley, and P. Gill. Observation of the $^2S_{1/2}$ - $^2F_{7/2}$ electric octupole transition in a single $^{171}\text{Yb}^+$ ion. *Phys. Rev. A*, 62(2):020501, Jul 2000.
- [56] L. S. Rothman and et al. The *HITRAN* 2008 molecular spectroscopic database. *J. Quant. Spec. and Radiative Transfer*, 110:533–572, 2009.
- [57] R. D. Saunders, W. R. Ott, and J. M. Bridges. Spectral irradiance standard for the ultraviolet: the deuterium lamp. *Appl. Optics*, 17(4):593–600, Feb 1978.
- [58] F. Schmidt-Kaler, H. Häffner, S. Gulde, M. Riebe, G.P.T. Lancaster, T. Deuschle, C. Becher, W. Hänsel, J. Eschner, C.F. Roos, and R. Blatt. How to realize a universal quantum gate with trapped ions. *Appl. Phys. B*, 77(8):789–796, Dec 2003.
- [59] Jeff A. Sherman, William Trimble, Steven Metz, Warren Nagourney, and Norval Fortson. Progress on indium and barium single ion optical frequency standards. 2005, arXiv:physics/0504013v2.
- [60] Jeffrey A. Sherman. *Single barium ion spectroscopy: light shifts, hyperfine structure, and progress on an optical frequency standard and atomic parity violation*. PhD thesis, University of Washington, Seattle, WA 98195, 2007.
- [61] P. W. Shor. Polynomial-time algorithms for prime factorization and discrete logarithms on a quantum computer. *SIAM J. Computing*, 26:1484–1509, 1997.
- [62] Bruce W. Shore. *The Theory of Coherent Atomic Excitation*, volume 2. Wiley-Interscience, New York, NY, 1990.
- [63] G Shu, M R Dietrich, N Kurz, and B B Blinov. Trapped ion imaging with a high numerical aperture spherical mirror. *J. of Phys. B*, 42(15):154005 (5pp), 2009.
- [64] Christoph Simon and William T. M. Irvine. Robust long-distance entanglement and a loophole-free bell test with ions and photons. *Phys. Rev. Lett.*, 91(11):110405, 2003.
- [65] Anders Sørensen and Klaus Mølmer. Entanglement and quantum computation with ions in thermal motion. *Phys. Rev. A*, 62(2):022311, Jul 2000.

- [66] A. V. Steele, L. R. Churchill, P. F. Griffin, and M. S. Chapman. Photoionization and photoelectric loading of barium ion traps. *Phys. Rev. A*, 75(5):053404, 2007.
- [67] Stig Stenholm. The semiclassical theory of laser cooling. *Rev. Mod. Phys.*, 58(3):699–739, Jul 1986.
- [68] H. Stoehr, F. Mensing, J. Helmcke, and U. Sterr. Diode laser with 1 hz linewidth. *Opt. Lett.*, 31(6):736–738, 2006.
- [69] A. J. Stone. Transformation between cartesian and spherical tensors. *Mole. Phys.*, 29(5):1461–1471, 1975.
- [70] A J Stone. Properties of cartesian-spherical transformation coefficients. *J. of Phys. A*, 9(4):485–497, 1976.
- [71] Hidemi Tsuchida, Motoichi Ohtsu, and Toshiharu Tako. Frequency stabilization of AlGaAs semiconductor laser to the absorption line of water vapor. *Jap. J. of Appl. Phys.*, 21(1):L1–L3, 1982.
- [72] I. Velchev, R. van Dierendonck, W. Hogervorst, and W. Ubachs. A Dense Grid of Reference Iodine Lines for Optical Frequency Calibration in the Range 571-596 nm. *J. of Mole. Spec.*, 187:21–27, January 1998.
- [73] Nikolay V Vitanov, Thomas Halfmann, Bruce W Shore, and Klaas Bergmann. Laser-induced population transfer by adiabatic passage techniques. *Annual Review of Physical Chemistry*, 52(1):763–809, 2001.
- [74] A. Weis and S. Derler. Doppler modulation and zeeman modulation: laser frequency stabilization without direct frequency modulation. *Appl. Opt.*, 27(13):2662–2665, 1988.
- [75] Edward A. Whittaker, Manfred Gehrtz, and Gary C. Bjorklund. Residual amplitude modulation in laser electro-optic phase modulation. *J. Opt. Soc. Am. B*, 2(8):1320–1326, 1985.
- [76] Chr. Wunderlich, Th. Hannemann, T. Körber, H. Häffner, Ch. Roos, W. Hänsel, R. Blatt, and F. Schmidt-Kaler. Robust state preparation of a single trapped ion by adiabatic passage. *J. Mod. Optics*, 54(11):1541–1549, 2007, quant-ph/0508159.
- [77] S. C. Xu, R. van Dierendonck, W. Hogervorst, and W. Ubachs. A dense grid of reference iodine lines for optical frequency calibration in the range 595-655 nm. *J. of Mole. Spec.*, 201:256–266(11), June 2000.
- [78] N. Yu, W. Nagourney, and H. Dehmelt. Radiative lifetime measurement of the Ba⁺ metastable D_{3/2} state. *Phys. Rev. Lett.*, 78(26):4898–4901, 1997.

- [79] X. Zhao, N. Yu, H. Dehmelt, and W. Nagourney. Isotope-shift measurement of the $6D^2S_{1/2}$ – $5D_{5/2}$ transition in Ba^+ . *Phys. Rev. A*, 51(6):4483–4486, 1995.

VITA

Matthew Rainer Dietrich was born on February 23rd 1982 to Rainer and Elizabeth Dietrich in Hoffman Estates, Illinois. He grew up in Crystal Lake, Illinois with his two brothers Michael and Daniel. From 1997 until his graduation in 2000 he attended the Illinois Mathematics and Science Academy in Aurora, Illinois. He then continued his education at Lawrence University in Appleton, Wisconsin whence he graduated in 2004 with a Bachelor of Arts in Math/Computer Science and Physics. Ever spiraling out from his hometown, he then moved to Seattle, Washington to partake in the graduate program at the University of Washington, where he joined Boris Blinov's fledgling group in January 2006. He graduated with his Ph.D. in experimental atomic physics in December 2009, and doesn't know exactly what to do with his new found freedom.